To the Graduate Council:

I am submitting herewith a dissertation written by Andrew Miles Glenn entitled "Single Muon Production and Implications for Charm in $\sqrt{s_{NN}} = 200$ GeV Au+Au Collisions." I have examined the final electronic copy of this thesis for form and content and recommend that it be accepted in partial fulfillment of the requirements for the degree of Doctor of Philosophy, with a major in Physics.

Soren P. Sorensen

Major Professor

We have read this dissertation
and recommend its acceptance:

Kenneth F. Read

Ted Barnes

Lawrence W. Townsend

Vince Cianciolo

Accepted for the Council:

Anne Mayhew

Vice Chancellor and
Dean of Graduate Studies

(Original signatures are on file with the official student records.)

Single Muon Production and Implications for Charm in

$\sqrt{s_{NN}}$ = 200 GeV Au+Au Collisions

A Dissertation

Presented for the

Doctor of Philosophy Degree

The University of Tennessee, Knoxville

Andrew Miles Glenn

December 2004

Acknowledgments

I would like to take this opportunity to thank the many people who have made this work possible. These include my advisors, my friends, my colleagues, and my family. Groups which I am fortunate to say have had no clear boundaries, and all of whom have helped create an encouraging and rewarding environment.

My advisor, Soren Sorensen, has always found the time to advise on physics or any other topic I wish. I am grateful for his infectious patience, enthusiasm, and positive attitude. I am indebted to Ken Read for his perspectives and suggestions, particularly on organization. I hope to follow them better in the future than I have in the past. I thank Vince Cianciolo for his insights into detector electronics and an ever present can-do attitude. I would like to thank Atsushi Taketani, George Gogiberidze, Laurence Villatte, and Vasily Dzordzhadze for expanding my scientific and cultural horizons.

I thank the students who came before me for showing me it could be done and the students who came after me for making me feel things are left in good hands. I am grateful to Jason Newby for bringing me into the group and for being a good friend. He and his wife Shelly opened their hearts and their home to me. I thank Donald Hornback and Irakli Garishvili for reminding me what classes were like, expressing true interest in this work, and providing enthralling political discussions.

I would also like to acknowledge the insights and contributions of my committee, including Larry Townsend and Ted Barnes.

I would like to thank my family for their patient support of my academic work. I thank my parents and siblings for teaching me that knowledge is found in many sources, only one of which is school. I would like to thank my wife's family for becoming my

family and for showing me the true meaning of strength.

Most of all, I thank my wife and closest friend Jennifer, to whom I dedicate this work. She has willingly made many sacrifices or my work. Her patience and support has been most appreciated. I hope she will find it rewarded.

Abstract

The PHENIX experiment, located at the Brookhaven National Laboratory's Relativistic Heavy Ion Collider, is designed to study high energy proton+proton and nucleus+nucleus collisions in order to characterize hot and dense nuclear matter. This dissertation presents the first analysis of single muon production in $\sqrt{s_{NN}} = 200$ GeV Au+Au reactions. Implications of the forward rapidity measurements for charm production are discussed. Motivation for charm production measurements and the role of open charm in characterizing the medium created in relativistic heavy ion collisions are presented, and the importance of measurements at forward rapidity is established. The results of this study are compared to relevant calculations and related measurements at RHIC. The number of muons produced from charm decays is found to scale with the number of binary collisions within large experimental errors over the studied kinematic region.

Contents

List of Tables

List of Figures

xvii

Chapter 1

Introduction

Humanity's yearning to understand its environment, beyond the limits of "practical" applicability, is an important and possibly a defining trait. This work attempts to explore one such area of research. It attempts to discuss and enhance a field of science at the forefront of humanity's understanding of matter under extreme conditions.

1.1 Motivation: The Quark Gluon Plasma

The most comprehensive understanding which the scientific community currently possesses to describe the building blocks of our universe is encapsulated in a framework referred to as the Standard Model. The Standard Model states that all material in the universe is comprised of six quarks, six leptons, their anti-particles and the force carrying particles for the four fundamental forces: gravity, electromagnetism, the weak force, and the strong force. Protons and neutrons are composed of three quarks held together by gluons, which mediate the strong force. There are also many particles, mesons, made essentially from two quark combinations. Quarks have the very interesting property that they cannot exist singly. They have a property called color which must be neutralized by forming particular combinations of two or more quarks. The
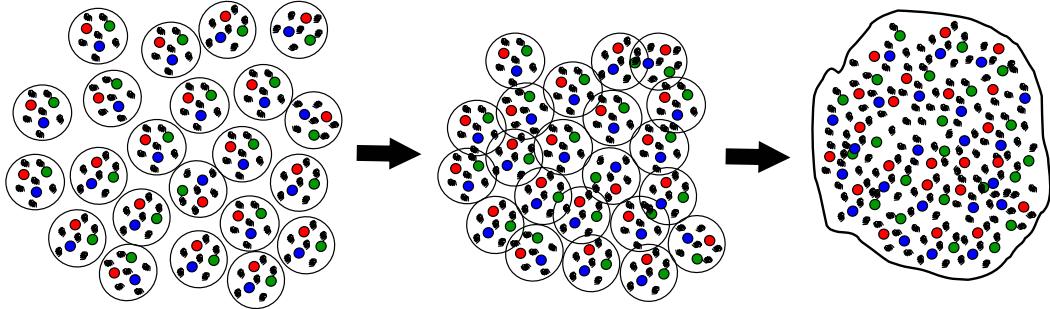
Figure 1.1: Diagram of the speculated transition of hadronic matter to QGP

theory of Quantum Chromodynamics (QCD) attempts to describe how the strong interaction holds quarks together. QCD calculations predict that in a collection of baryons, three quark states, which is localized in a small enough volume and has a sufficient collective temperature, the quarks and gluons which constitute the baryons will cease being confined to their original baryon [1]. The system has a phase transition in which quarks and gluons, not baryons, become the relevant degrees of freedom. This means that an understanding of the initial baryons would not be sufficient to describe many aspects of the system. A schematic representation of this proposed process is shown in Figure 1.1. A somewhat analogous phase change occure when a florescent light bulb is turned on; electrons become free to move over large distances and the material in the glass, now referred to as a plasma, has very different physical properties. Since this proposed breakdown and merging of baryons should result in similar deconfinement of the quarks, this state of matter has been termed a Quark Gluon Plasma (QGP).

Such a state of matter has been speculated to exist in nature. In fact, it is widely held that the entire universe was a QGP in its early existence. Additionally, QGP may be present today at the core of some neutron stars [2]. The Chandra X-ray Observatory has recently observed a star just 11 km across, and with a temperature profile which appears inconsistent with neutron star [3].

It would be advantageous to have a more controllable, and nearby, environment
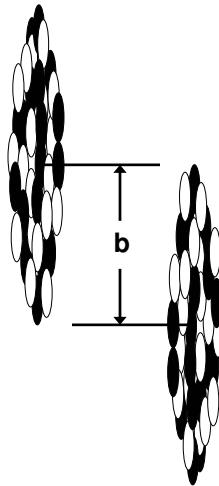
Figure 1.2: Diagram of a $A + A$ collision. Note that the nuclei are Lorentz contracted.

in which to study the possibility and properties of a QGP. To prove the existence of QGP and, if found, systematically study it, scientists have turned to relativistic heavy ion (nucleus-nucleus) collisions. Such collisions appear to be a promising tool due to the amount of energy they can provide within a small volume. The energy density of gold+gold, Au+Au, interactions at the Relativisic Heavy Ion Collider facility have been estimated to reach well over 10 times the energy density of normal nuclear matter [4].

1.2 Centrality

One of the most useful concepts for characterizing a nucleus-nucleus, or $A + A$, collision is centrality. Centrality is basically a measure of the amount of overlap of the colliding nuclei. Qualitatively, centrality ranges from central, corresponding to almost complete overlap, to peripheral, corresponding to nearly no overlap. Figure 1.2 gives a pictorial representation of centrality. Practically speaking, centrality can only be measured and not experimentally controlled, but it provides a natural method to describe the "violence" of the collisions.

1.3 Hints of the QGP?

Many interesting experimental observations have already been made at heavy ion colliders which may be inconsistent with normal nuclear matter and consistent with a QGP. A brief overview of some of these observations will be made here.

1.3.1 Charmonium Suppression

One signal which was proposed early on as an indicator of a QGP was the suppression of charmonium, the bound states of charm and anti-charm, $c\bar{c}$, quark pairs. It was postulated that in the deconfined medium of a QGP, color charges from surrounding quarks would screen the color charges, similarly to Debye screening in classical electrodynamics, of the charmed quarks and prevent them from being attracted and bound. The J/ψ particle is the lightest form of observable charmonium, and it is theorized to be the particle for which this screening phenomena will be most easily observed.

Other than the Relativistic Heavy Ion Collider (RHIC) only the Super Proton Synchrotron (SPS) and possible the Alternating Gradient Synchrotron (AGS) are thought to have created sufficient energy densities to possibly create a QGP. The NA50 experiment at the SPS has reported data on J/ψ yields which have been interpreted by some as just such a suppression. Figure 1.3 shows the NA50 measurement of a J/ψ suppression factor as a function of the estimated energy density. This interpretation has been quite controversial, and several hadronic, normal nuclear matter, scenarios that have been proposed which claim to reproduce the suppression pattern. One of the top goals of RHIC is to extensively study J/ψ production and charm production in general to help clarify the interpretation and look for additional non-hadronic effects in all aspects of charm production. The University of Tennessee/Oak Ridge National Laboratory relativistic heavy ion physics group has been actively involved in the study of the J/ψ at RHIC. The doctoral work of UT graduate Jason Newby described a J/ψ study on the
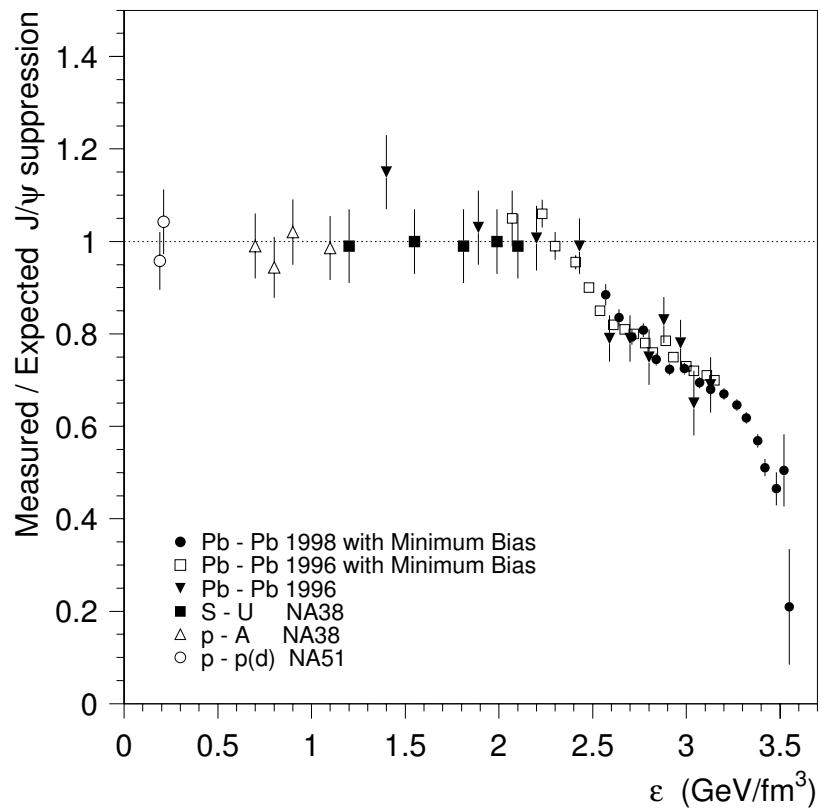
Figure 1.3: NA50 measurement of J/ψ suppression factor as a function of the estimated enegy density [5].

same data set used in this work [6].

1.3.2 Jet Suppression

One of the intriguing observations which has been made at RHIC is another form of suppression, the phenomena of jet suppression. When a hard, high energy, scattering of two quarks occur in a proton+proton collision, they begin to travel in opposite directions with high momentum. When separating, a large amount of energy is present due to the stong force between the quarks. In a process called fragmentation, this energy is converted to a large number of particles. This generally results in a leading particle, an energetic particle with high momentum transverse to the beam axis which has a large number of fragmentation partners in a nearby cone. This process occurs symmetrically,i.e. the quarks travel in opposite directions, in order to conserve momentum. A suppression of such high transverse energy particles has been observed in central Au+Au collisions by multiple experiments. In a high density environment, a quark jet may lose subtantial energy in the form of gluon radiation before fragmenting, resulting in a reduction of the total number of produced high energy particles. The suppression is not seen in proton+proton or deuteron+Au collisions as shown in data from the PHENIX experiment, Figure 1.4. This can be directly related to geometry by identifying such jets then measuring what particles are seen on the opposite side, where the other jet, "away-side" jet, is expected. The away-side jet is clearly present in $p + p$ and d+Au collisions, but practically disappears for central Au+Au collisions as seen in the data from the STAR experiment shown in Figure 1.5. The widely accepted interpretation is that the away side jet loses most of its energy while traveling through an extremely dense medium. The fairly direct observation of a change from a dilute system, which jets have little trouble passing through, to an extremely dense medium is considered some of the strongest evidence for a new state of matter in RHIC collisions.

6
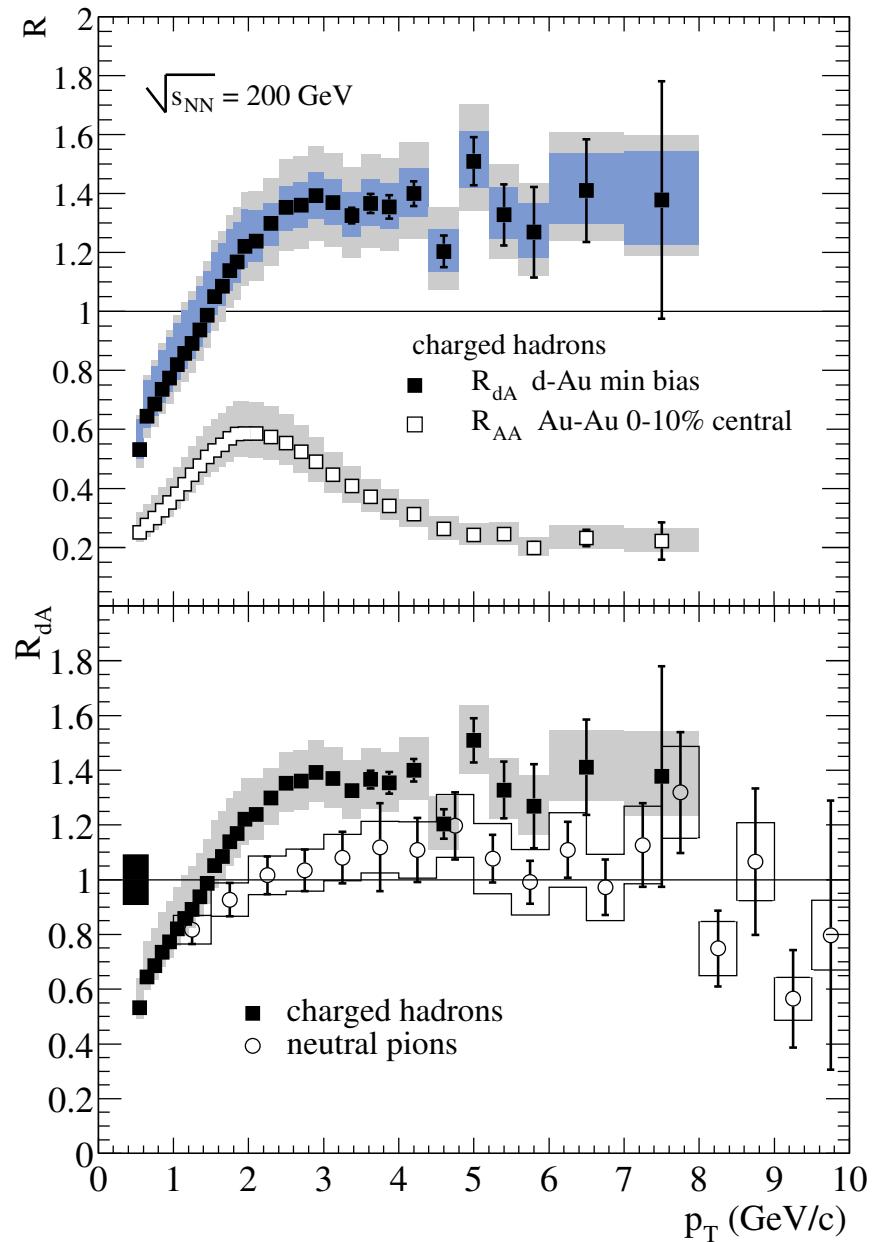
Figure 1.4: High transverse momentum hadron suppression measured at PHENIX [7]. The top graph shows that charged hadrons are extremely suppressed at $p_T > 3$ GeV/c in Au+Au interactions relative to d+Au.
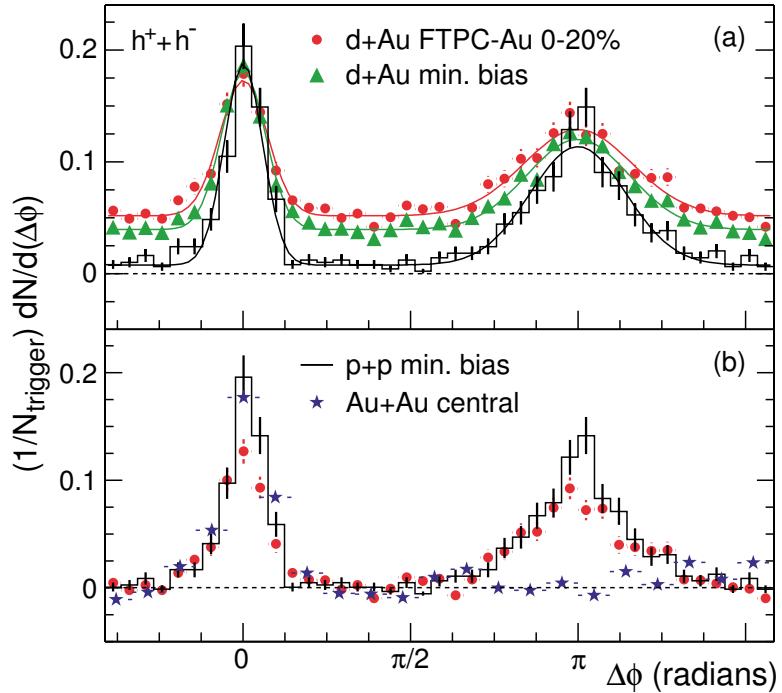
Figure 1.5: Extreme Suppression of the away-side jet in central Au+Au collisions as observed by the STAR experiment [8]. The angular distribution of charged hadrons, where the highest energy particle defines $\phi = 0$, shows two clear peaks 180° apart for $p+p$ and $d+$Au collisions. These indicate a near side jet and a far side jet. The far side jet peak is completely supressed in central Au+Au collisions.

1.4 This Work

Another signal, one closely related to charmonium, which is expected to provide evidence for the type of matter created in heavy ion collisions is open charm production. As further motivated in the following chapter, yields of mesons with only one charm, or anti-charm, quark have the potential to provide strong evidence for the QGP as well as to clarify the understanding of charmonium production. This thesis presents a study of semi-leptonic decays of charmed mesons into $\mu + X$ in Au+Au interactions at RHIC. Chapter 2 presents a theoretical overview of charm production and issues related to production in a nuclear environment. Chapter 3 discusses the experimental apparatus used to record the data used in this analysis, and Chapter 4 presents a discussion on event selection and associated issues. Chapter 5 will present the data reduction and signal extraction, and Chapter 6 discusses the relevance of this measurement to theory and other measurements. Finally Chapter 7 will summarize the conclusions which can be drawn from this study.

Chapter 2

Charm Production

Charm production has been experimentally observed and studied for almost 30 years, yet the understanding of this topic is far from complete. While the initial production of $c\bar{c}$ pairs in $p + p$ collisions seems fairly well understood, underestimated cross sections bring the completeness of the standard picture of how these quarks evolve to form hadrons into question. In $p + A$ collisions, the effects of nuclear geometry and modifications to nucleons when placed in a nucleus have been studied at fixed target energies, and similar studies with $d + A$ collisions are underway at RHIC. For $A + A$ collisions, predictions of both open charm enhancement, due to modifications of the hadronization process and/or significant $c\bar{c}$ production after the initial collision, and suppression, due to energy loss in a dense QGP medium, exist.

Open charm production is also considered quite important in understanding J/ψ production. Color screening due to deconfinement has been predicted to suppress the production of J/ψ if a QGP is formed, but this effect should not suppress open charm production. In order to interpret J/ψ production, open charm cross sections must be measured to more clearly differentiate suppression of J/ψ production relative to $p + p$ collisions due to color screening from suppression due to an overall change in charm production.

Table 2.1: Some properties of charmed mesons.

Meson	quark composition	Mass (MeV)
D^+	$c\bar{d}$	1869.3 ± 0.5
D^-	$\bar{c}d$	1869.3 ± 0.5
D^0	$c\bar{u}$	1864.5 ± 0.5
$\bar{D}^0$	$\bar{c}u$	1864.5 ± 0.5
D_S^+	$c\bar{s}$	1968.6 ± 0.6
D_S^-	$\bar{c}s$	1864.5 ± 0.5
D^{*+}	$c\bar{d}$	2010.0 ± 0.5
D^{*-}	$\bar{c}d$	2010.0 ± 0.5
D^{*0}	$c\bar{u}$	2006.7 ± 0.5
$\bar{D}^{*0}$	$\bar{c}u$	2006.7 ± 0.5
D_S^{*+}	$c\bar{s}$	2112.4 ± 0.7
D_S^{*-}	$\bar{c}s$	2112.4 ± 0.7

2.1 Charmed Mesons

Open charm production is primarily studied through detection of charmed mesons, a bound state of a quark and an anti-quark. Mesons containing one charmed quark, denoted as D mesons, are said to represent open charm, while mesons made up of $c\bar{c}$, termed charmonium, are considered hidden or closed charm. This means that open charm systems have a non-zero charm quantum number ($C = \pm 1$) and closed charm systems have no net charm ($C = 0$). Some properties of D mesons are summarized in Table 2.1, and the energy spectrum of charmed mesons is shown in Figure 2.1. One of the properties of the D meson which will be utilized in this work is their high probability to suffer weak decays in which one product is a lepton. An example of such a semi-leptonic decay is shown in Figure 2.2.
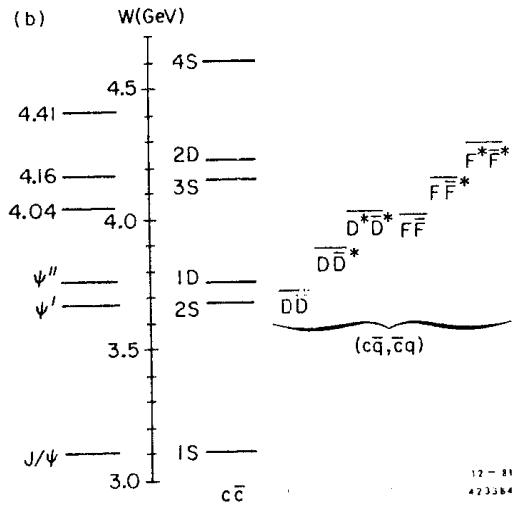
Figure 2.1: Lowest lying charmed mesons and the measured position of vector mesons. F is an earlier notation for D_S. [9]
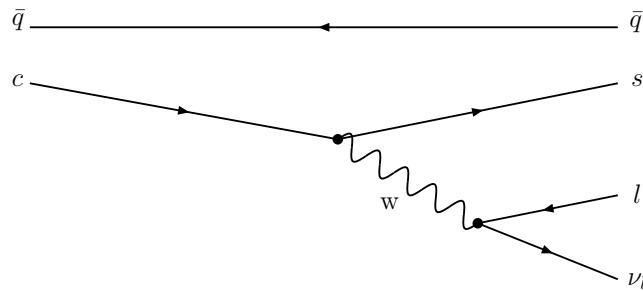
Figure 2.2: Example diagram of a semi-leptonic D decay. The charm quark decays via the weak force into a strange quark, a lepton, and a neutrino.

2.2 Historical Introduction

Charm production has been studied experimentally since the discovery of a bound state of $c\bar{c}$ in November of 1974. Experiments on opposite sides of the US independently observed a resonance around 3.1Gev/c^2. Brookhaven National Laboratory in New York measured e^+e^- pairs from collisions of 28 GeV protons on a beryllium target [10] at the AGS facility, while the Stanford Linear Accelerator Center in California used an energy scan of e^+e^- beams at the SPEAR collider [11]. After the discovery, the particle was named J and ψ by the BNL and SLAC groups respectively, but the particle is now generally referred to as the J/Ψ. Burton Richter, leader of SLAC group, and Samuel C. C. Ting, leader of the BNL group, jointly received the 1976 Nobel Prize in physics for the discovery.

In 1976 a SLAC-LBL team made the first observations of a charmed quark bound with a non-charmed quark, termed D mesons [12] [13]. This work began the experimental study of open charm.

2.3 Methods for Observing D Mesons

There are many methods for detecting particles produced in nuclear collisions. For long lived particles, detection may mean direct observation of the particle's passage through detector elements. This passage is often inferred from energy deposition via processes such as gas ionization and hadronic or electromagnetic showers. These spatial and energy measurements can often be combined with timing measurements and momentum information, measured via the bending of charged particles in a magnetic field, to provide a detailed description of the observed particle's properties.

For short lived particles such as D mesons, $\tau \approx 10^{-12}$s, which travel only a very short distance before decaying, scientists must turn to their decay products, or "daughters", and possibly to the decay products of daughter particles, "grand-daughters".

These decay products are long lived enough to pass through detectors, thus allowing for indirect study of the parent. One simple, yet powerful, tool for observing a particle using information from its decay products is an invariant mass distribution. This is done by assuming that a given combination of particles, $K^+\pi^-\pi^-$ for example, are the decay products of a particle. The mass of this postulated particle can then be calculated from the energies and momenta of the possible decay products. The invariant mass squared for a combination of particles is given by equation 2.1,

$$M^2 = (\sum_{i=particles} E_i)^2 - (\sum_{i=particles} \vec{p_i})^2.$$

(2.1)

Peaks in this distribution reveal the masses of particles which decay into the observed combination. The shape of a peak can be fit to determine the yield, but care must be given in subtracting off the continuum background of the mass spectrum. A recent invariant mass spectrum showing a D meson peak observed by the STAR experiment at RHIC is discussed in Chapter 6.

Experimental evidence for D^0 and $\bar{D}^0$ mesons was first shown in invariant mass spectra of $K^{\pm}\pi^{\mp}$ and $K^{\pm}\pi^{\pm}\pi^{\mp}\pi^{\mp}$ in e^+e^- collisions at SPEAR [14]. Shortly after, D^+ and D^- peaks were seen in $K^{\mp}\pi^{\pm}\pi^{\pm}$ invariant mass spectra, Figure 2.3, of more SPEAR data [15]. A similar technique of looking at recoil mass, the mass of a postulated undetected particle to satisfy energy and momentum conservation, for events in the D peak was used in the same analyses to show that the D mesons appeared to be produced in pairs. The recoil mass spectrum for $D^{\pm}$ in Figure 2.4 shows that there is a threshold, of $\sim 2m_D$ for producing events in the invariant mass peak. The measurements of these particles and their apparent associative production provided important evidence toward confirming the existence of the charm quark.

Detection of all of the decay products of a particle is not always possible given detector acceptance, luminosity and other constraints, but measurements for well studied particles are often still possible. Under these circumstances, detection of only a
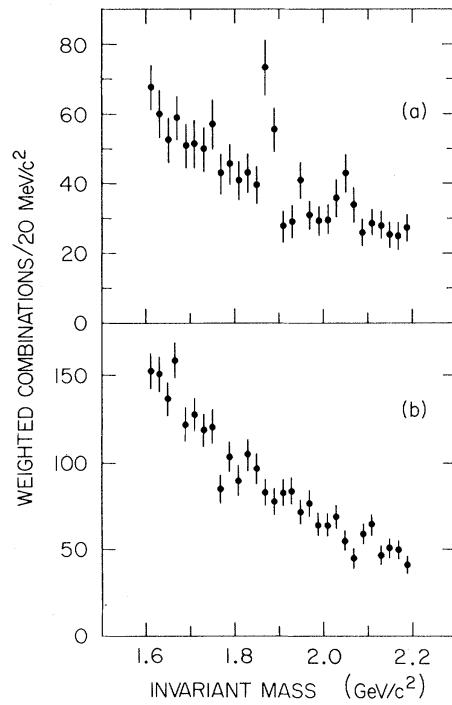
Figure 2.3: Invariant mass spectra for (a)$K^{\mp}\pi^{\pm}\pi^{\pm}$ and (b)$K^{\mp}\pi^{+}\pi^{-}$ combinations. The data are from 19K $E_{\text{c.m.}}$=4.03 GeV multihadronic events.[15]
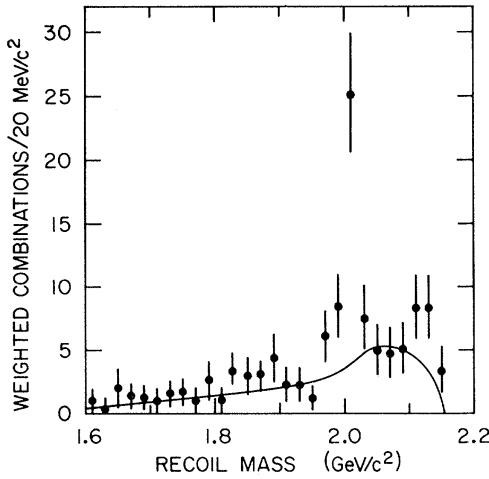
Figure 2.4: Recoil mass spectra for events from the $K^{\mp}\pi^{\pm}\pi^{\pm}$ peak, 1.86 to 1.90 GeV/c^2 in Figure 2.3. The background estimate, smooth curve, is from events in the same mass region of the $K^{\mp}\pi^{+}\pi^{-}$ spectra. [15]

15

subset of daughters, often just one particle, can be used to infer the presence, or probability of presence, of the parent. The inclusive branching ratio for decays involving measured daughters must be known. This method generally requires more care in estimating sources of background and delivers less direct information about the parent than full invariant mass reconstruction, but such indirect statistical measurements provide increased statistics and allow for otherwise impossible measurements. Since full reconstruction of D mesons is not currently feasible with PHENIX, this indirect observation method is used for the analysis presented in this work.

This method was used at Fermilab in 1983 to study D meson production by measuring muons produced from a 350 GeV p beam incident on a Fe target [16]. The experiment examined the X_F dependence and provided a total $D\bar{D}$ cross section. Later experiments by WA78 explored the nuclear dependence of charm production with 320 GeV π^- [17] and 300 GeV p [18] beams by similarly measuring single muon production with Al, Fe and U targets. Both of these experiments used variable target densities, based on the premise that only prompt muons would be produced in a target approaching infinite density, to help quantify the contributions of prompt muons, from semileptonic decays of D mesons, and secondary muons, from π and K decays. Of course, this is not an option in collider experiments.

Both of these statistical methods are susceptible to backgrounds from other decays, especially in high multiplicity environments produced in Au+Au collisions. One of the most promising methods to reduce this background for D mesons comes from precision vertex information. Although short lived, the D travels a measurable distance before decaying. Given a $c\tau \approx 0.3mm$ and significant time dilation, this displacement is measurable by technologies such as a highly segmented Si vertex detector. Requiring that any daughter candidates be consistent with the secondary vertex of a D decay can provide drastic background reduction. NA60 is using this method in ongoing charm analyses, see Figures 2.5 and 2.6, and precision vertex information may become avail-
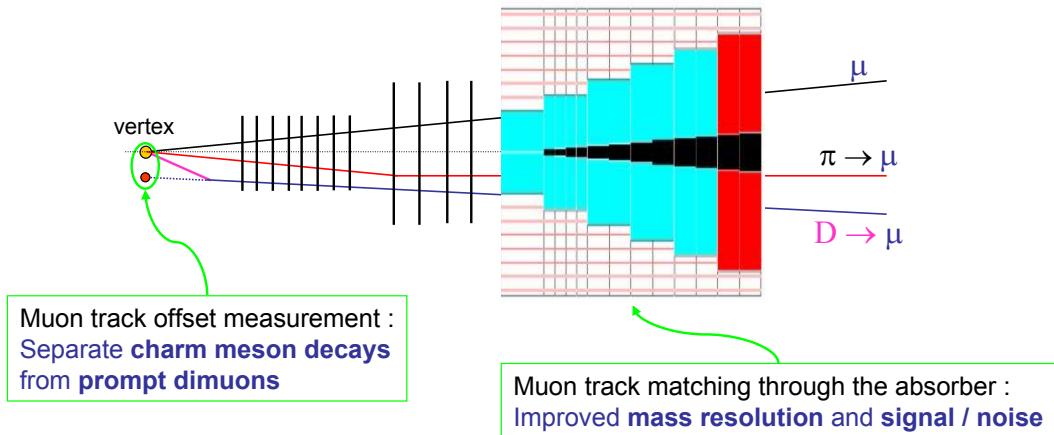
Figure 2.5: A partial sketch of the NA60 experimental apparatus demonstrating the concept of separating muons from charm decays via their displaced vertex. [19]
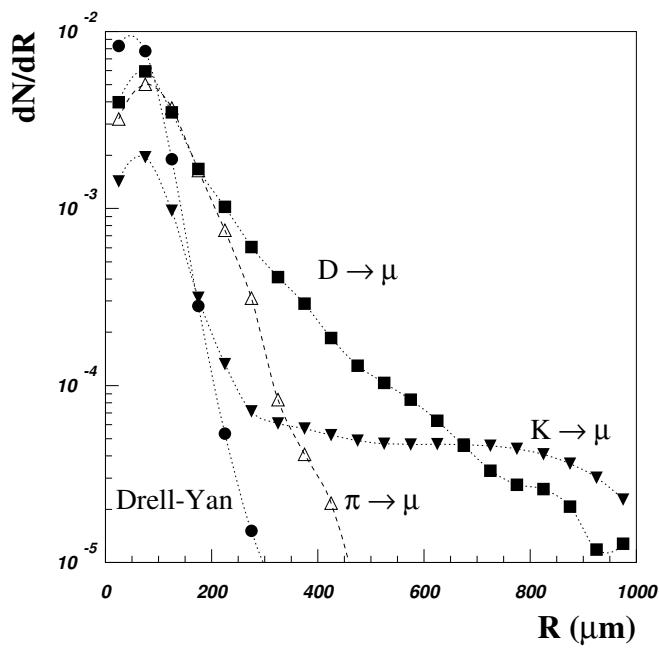
Figure 2.6: NA60 simulation of the offset distribution for muons from different sources. The offset, R, is the minimum distance, measured in the transverse plane, between a track and the interaction point. The distributions are not normalized. [20]
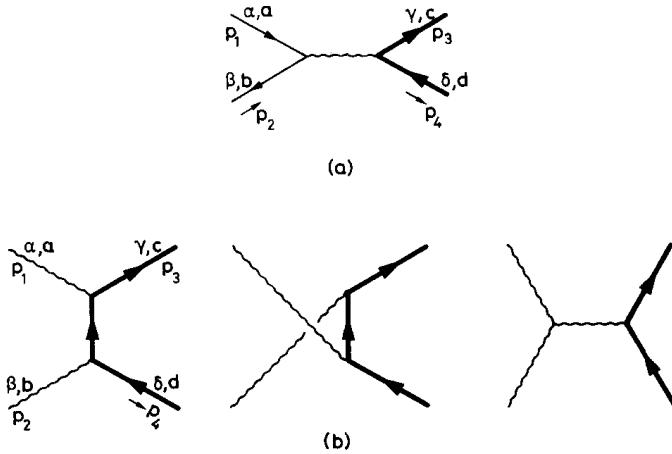
Figure 2.7: Lowest order QCD flavor creation diagrams for (a) $q\bar{q} \rightarrow c\bar{c}$ QCD and (b) $gg \rightarrow c\bar{c}$. [21]

able to PHENIX in a future upgrade.

2.4 Charm Hadroproduction

Although many mechanisms can produce charm, the gluon fusion process is most relevant for this study. Much work has been done to understand charm production in hadronic collisions through Quantum Chromo-Dynamics, in particular perturbative QCD, since the mid 1970's. In 1978 B.L. Combridge published a lowest-order pQCD description of open charm production in pp and $p\bar{p}$ collisions. He categorized the production mechanisms as flavor creation, $q\bar{q} \rightarrow c\bar{c}$ and $gg \rightarrow c\bar{c}$, and flavor excitation, $qc \rightarrow qc$ and $gc \rightarrow gc$, in which a c quark is scattered out of the nucleon sea, as depicted in the diagrams of Figures 2.7 and 2.8 respectively. Combridge admits that this division may lead to "double-counting" since some diagrams can contribute to both creation and excitation. Figure 2.9 shows the energy dependence of the different flavor creation mechanisms. Notice that gluon fusion, $gg \rightarrow c\bar{c}$, becomes the primary contribution well below RHIC energies. Although one of the principle findings of this
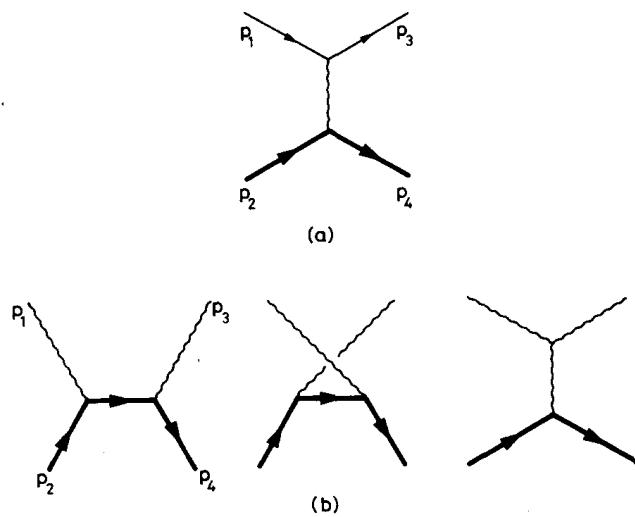
Figure 2.8: Lowest order QCD flavor excitation diagrams for (a) $qc \rightarrow qc$ QCD and (b) $gc \rightarrow gc$. [21]
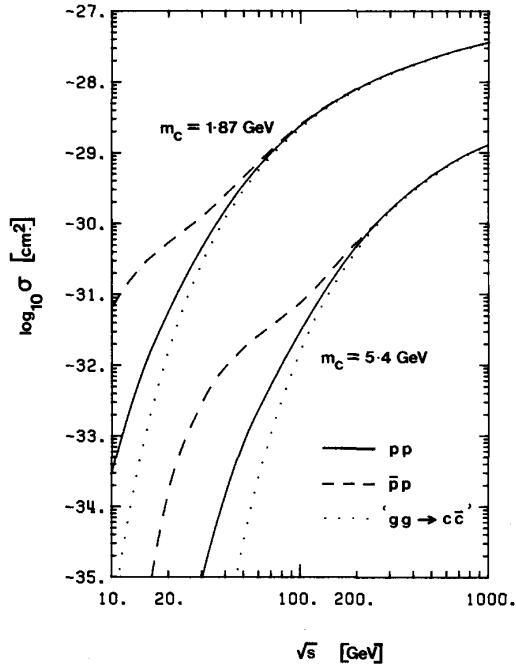
Figure 2.9: Estimates for production of heavy flavored states from $gg \rightarrow c\bar{c}$ and $q\bar{q} \rightarrow c\bar{c}$ [21]. Gluon fusion is calculated to dominate quark annihilation for energies above 200 GeV.
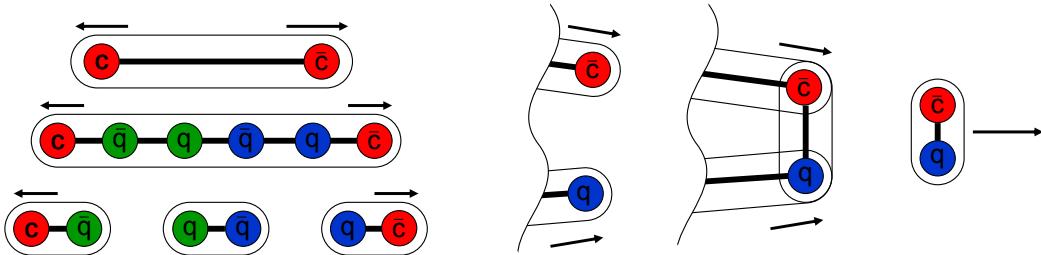
Figure 2.10: A pictorial representation of D meson production via fragmentation (left) and recombination (right).

work was that charm production from excitation was as large as charm production from flavor creation, later work [22] showed that unaccounted for destructive interference makes the flavor excitation terms negligable. The most widely held view is still that gluon fusion dominates charm quark production at RHIC and SPS energies, but this does not address the issue of hadronization.

Combridge, and many other works, assumed that fragmentation was the primary method through which charm quarks (anti-quarks) combine with a light anti-quark (quark) to form a meson. In fragmentation, a pair produced quark and anti-quark, which are coupled with a linear potential of the strong force, begin to separate with some relative velocity. If the velocity is large enough, the energy stored in the field can become sufficient to produce new quark pairs. At this point, the string, representing the gluon field, can "fragment" to produce new quark-antiquark pairs. Combinations of these may then have low enough relative velocities to combine into hadrons.

Combridge also mentions the possibility that heavy quarks may "combine with other quarks present after the initial interaction" to form hadrons. In other words, there is a possibility that a quark produced in one collision will be close enough in phase space to combine with a pre-existing anti-quark which had no prior association to form a hadron. Coalesence hadronization is pictorially compared to fragmentation in Figure 2.10. This recombination component is still an active area of research and has gained

increased prominence with possible applications regarding formation of charmonium in RHIC collisions, which have ~ 10 $c\bar{c}$ pairs in central Au+Au collisions [23][24].

One motivation for the need to quantify any recombination is that leading-order pQCD underestimates open charm production in hadron collisions by about a factor of 5, and next-to-leading-order corrections only get to within roughly a factor 2.5 [25]. It is widely held that these scaling factors, often referred to as K factors, will quickly approach 1 with higher order calculations, but it seems reasonable to examine other possibly relevant effects while this is still an open issue. Rapp and Shuryak have developed a recombination framework which they used to study many aspects of D meson production in pp, $pA(N)$, and $\pi A(N)$ collisions. This method seems to do a good job of describing the x_F and energy dependence of D meson flavor asymmetry which has not been completely understood in a pQCD framework. Since valence quarks from the colliding protons, a *uud* quark combination, can coalesce with produced $\bar{c}$ quarks, D^- ($\bar{c}d$) is favored over D^+ ($c\bar{d}$), $\bar{D}^0$ ($\bar{c}u$) is favored over D^0 ($c\bar{u}$) and D^+ ($c\bar{d}$). A comparison of a recombination calculation to $p + p$ data which shows the good agreement is shown in Figure 2.11. The following predictions are made for $\sqrt{s_{NN}} = 200$ GeV $p + p$ collisions: $R_{(D^+ + D^-)/(D^0 + \bar{D}^0)} = 0.40$, $R_{D^-/D^+} = 1.24$, $R_{\bar{D}^0/D^0} = 1.35$, and $R_{D_s/D} = 0.23$. The applicability of this approach to $p + A$, and similar systems, as well as an extension to $A + A$ are discussed later in this chapter.

2.5 Nuclear Effects

In order to fully understand open charm production in an $A + A$ induced QGP environment, one must understand any initial state effects that arise from the introduction of a nucleus. Alternatively stated, any non-trivial A dependence of open charm production needs to be examined.
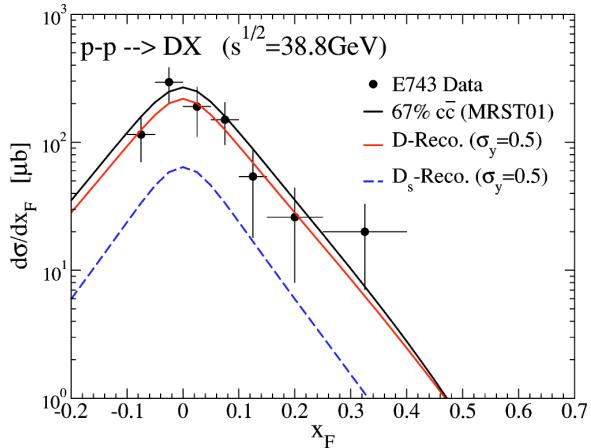
Figure 2.11: Comparison of Rapp et. al. calculation of the recombination contibutions to E743 $p + p$ data for inclusive D mesons. The upper solid line represents 67% of the underlying c and $\bar{c}$ distributions using the MSRT01 parton distribution functions with $K = 5$. [25]

2.5.1 Experimental A Dependence

The nuclear dependence of a hard production cross-section is often parameterized as $\sigma^{pA} = \sigma^{pp} A^\alpha$, where $\alpha = 1$ would correspond to perfect binary collision scaling, i.e. no nuclear effect beyond the expected geometric scaling. This comes from the expectation of binary collision scaling, $\frac{\sigma_{AB \to X}}{\sigma_{AB}} = \nu \frac{\sigma_{pp \to X}}{\sigma_{pp}}$, for hard processes and the Glauber calculation for the average number of binary collisions, ν, integrated over impact parameter, $\nu = \frac{AB\sigma_{pp}}{\sigma_{AB}}$ [26]. Under these assumptions, $\sigma_{pA \to X} = \sigma_{pp \to X} A$ and $\sigma_{AA \to X} = \sigma_{pp \to X} A^2$. A summary of experimental measurements of α is shown in Table 2.2. All but the earliest experiments, which used an indirect measure of open charm and were not sensitive to low x_F, have α consistent with 1. This discrepancy might be easily resolved if α exhibited a strong x_F dependence, but measurements indicate there is not a strong x_F dependence [27][28] [29].

Table 2.2: A dependence of open charm production. The WA78 values are weighted averages of μ^+ and μ^-.[30]

Experiment	Beam	Detected	α	x_F range
E769	$\pi^\pm$ 250 GeV	D^0, D^+	1.00 ± 0.05	> 0.0
E789	p 800 GeV	D^0	$1.02 \pm 0.03 \pm 0.02$	~ 0.0
WA82	π^- 340 GeV	D^0, D^+	0.92 ± 0.06	> 0.0
WA78	π^- 320 GeV	μ^+, μ^-	0.81 ± 0.05	> 0.2
E769	p 300 GeV	μ^+, μ^-	0.78 ± 0.09	> 0.2

2.5.2 Cronin Enhancement

In 1975, J. W. Cronin et. al. made the unexpected observation that high p_T hadron cross sections were enhanced in p+A collisions relative to $p+p$ collisions by a factor larger than the expected A scaling, discussed in Section 2.5.1 [31]. Particle production for various species, $K^\pm$, $\pi^\pm$, and $p^\pm$, produced in collisions of a 300 GeV proton beam incident on Be, Ti, and W targets at Fermi National Accelerator Laboratory was measured at $\sim 90^o$, mid-rapidity, in the pA center of mass frame up to $p_T = 6$ GeV. The A dependence for each particle type, i, was parameterized as $I_i(p_T, A) = I_i(p_T, 1)A^{\alpha_i(p_T)}$, $I = Ed\sigma/d^3p$, and the cross section for $A = 1$ was estimated by extrapolating from the various $p + A$ measurements. For p_T < roughly 2 GeV, α was < 1, but for p_T > 2 Gev, α was greater than 1, indicating an enhancement over the expected scaling. This enhancement is generally interpreted as resulting from collective behavior, including multiple interactions between the incoming proton and the nucleons in the target. An upgraded version of the experiment with thinner targets, 0.03 interaction length, and a liquid deuterium target, for 400 GeV beam, collected data with 200, 300 and 400 GeV protons [32]. As shown in Figure 2.12, α increases until ~5 GeV and then appears to drop or plateau for the various species.

Any such Cronin enhancement in RHIC collisions should be accounted for when looking for final state effects, such as the QGP. Before $p+A$ or $d+A$ measurements were
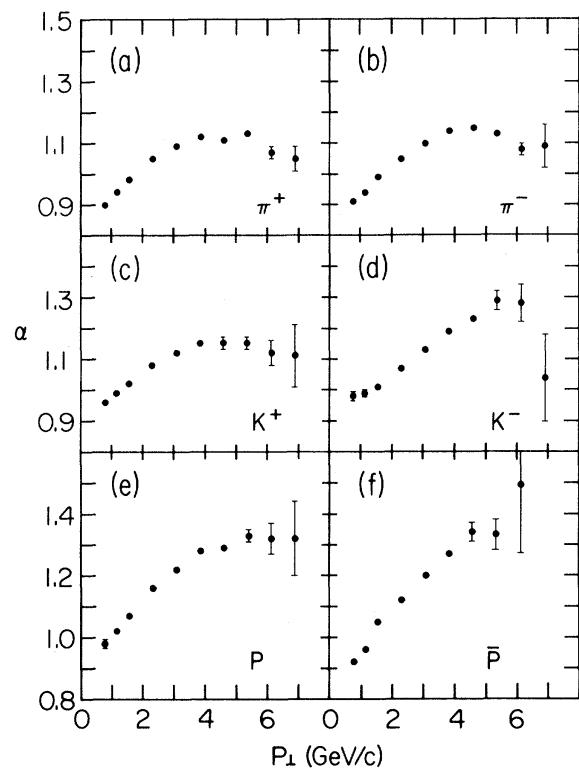
Figure 2.12: Early observation of Cronin enhancement for a 400 GeV p beam. α, the power dependence of A, is described in the text. [32]
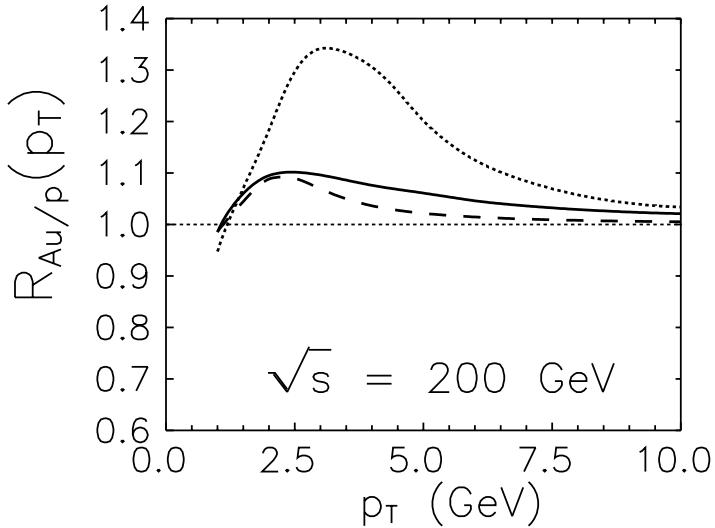
Figure 2.13: Prediction for Cronin enhancement of pions at RHIC. The dotted (dashed) line represents incoherent (coherent) production, while the solid line is the final prediction based on interpolation between the other two. [33]

made at RHIC, Kopeliovich et al. supplied the first "comprehensive description of the dynamics behind the Cronin effect resulting in parameter-free predictions which agree with available data"[33]. The work stresses their assertion that the Cronin mechanism changes from incoherent production on different nucleons at low energies, to a coherent process at very high energies. The coherence length, $l_c = \frac{\sqrt{s}}{m_n k_t}$ sets the scale for this transition from incoherent to coherent; l_c is approximately 5 fm for RHIC energy over the p_T range where the Cronin effect is most prevalent. Their estimate for Cronin enhancement at RHIC, shown in Figure 2.13, peaks at 2.5 GeV and slowly approaches 1, i.e. no enhancement. Although Cronin enhancement was originally quantified by α, a more current standard measure of the effect is given by the Cronin ratio, $R(p_T) = \frac{B}{A} \frac{d\sigma_{pA}/d^2 p_T}{d\sigma_{pB}/d^2 p_T}$, where A and B are the atomic numbers of different targets. This is motivated by the average number of binary collisions, ν, integrated over impact parameter, $\nu = \frac{AB\sigma_{pp}}{\sigma_{AB}}$ as discussed earlier in this chapter. Generally, A is greater than B, and B is often 1 or 2. Recent measurements of hadron production at mid-rapidity in d+Au collisions

at RHIC, Figure 1.4, seem to indicate a larger than expected Cronin enhancement. A brief review of theoretical Cronin models can be found in Reference [34].

2.5.3 Shadowing and the Nuclear Modification Factor

One of the most direct consequences in changing from $p + p$ to $p + A$ collisions is an expected modification of parton distributions in the presence of a nucleus. This effect, called shadowing, is generally described in terms of a modification of the probability of finding a particular type of parton at a given momentum fraction, x, in a nucleon compared to this probability for a bare proton or neutron. If $S_p(x)$ and $S_A(x)$ are the probabilities of finding a gluon in a proton and a nucleus respectively, then $R_A(x) = \frac{S_A(x)}{AS_p(x)}$, often referred to as a nuclear modification factor, gives a measure of any such change. A depletion in $R_A(x)$ is observed at low x which is suggestive of the term shadowing, but it is notable that an enhancement is often expected over some region, an anti-shadowing region. The peak of the anti-shadowing region is expected to be around $x = 0.1$ in Au. One calculation of this effect by R. Vogt for A = 200 is shown in Figure 2.14. The theoretical uncertainty for shadowing is larger for gluons, which have the largest impact on open charm production. Shadowing is generally considered a geometric effect due to the close grouping of protons and neutrons in a nucleus, but any mechanism which changes R_A, such as an A and energy dependent parton saturation effect, can be discussed in terms of shadowing. Most energy dependence though, is simply due to the range of x which is explored. One estimate for the energy dependence of $c\bar{c}$ production from RHIC to LHC with and without gluon shadowing is shown in Figure 2.15. The estimate is a leading order gluon-gluon fusion calculation which assumes "strong" gluon shadowing, and the calculation is mainly meant to demonstrate the effect of gluon shadowing rather than estimate absolute cross-sections [36]. The effect is significantly larger for LHC than RHIC.
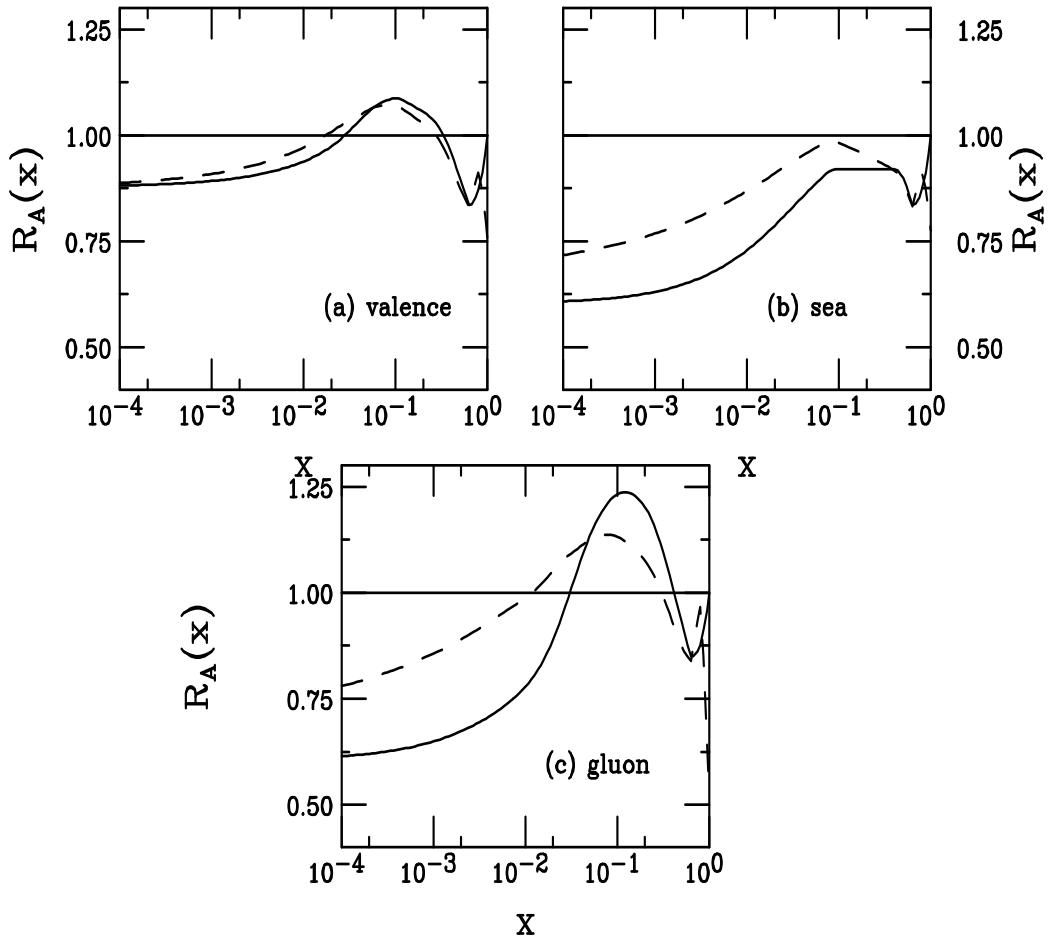
Figure 2.14: Shadowing parameterizations for $A = 200$ for (a) valence quarks, (b) sea quarks, and (c) gluons [35]. Each type of parton exhibits significantly different shadowing. The solid (dahsed) curve is for the interaction scale $\mu = \mu_0$ ($\mu = 10$ GeV).

27
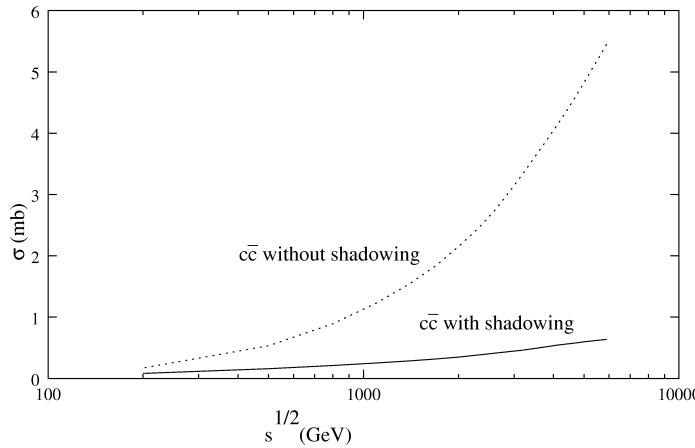
Figure 2.15: Estimate of the cross section from $gg \rightarrow c\bar{c}$. The solid line includes gluon shadowing. [36] Shadowing is expected to be a much larger effect above RHIC energies.

2.5.4 Color Glass Condensate

One of the more exciting of the nuclear effects is the possibility of a new state of matter termed the Color Glass Condensate which may describe the initial condition of nuclear collisions at RHIC. A detailed description of a hadron includes an active sea where partons are constantly created and destroyed over a timescale of < 1 fm/c, which can be thought of in terms of the uncertainty principle $\Delta E \Delta t \approx \hbar$. If the hadron were moving fast enough, Lorentz time dilation would cause these dynamics to appear frozen to a stationary observer. Also, with high enough energy collisions the low x region of the hadron can be probed. At low enough x the probability for $gg \rightarrow g$ should become large, and this leads to a maximum gluon density ($\frac{dN_{gluon}}{dy} \approx 1000$ [37]) or gluon saturation. At high enough energies, the momentum at which this saturation occurs should be greater than the hard scale, $Q^2 \gg \Lambda_{QCD}^2$, thus perturbative QCD is applicable. An effective field theory of the Color Glass Condensate (CGC) has been formulated to describe such a system. The term CGC is used because: 1) the partons carry color charge (Color), 2) the system is in frozen disorder (Glass) and 3) the gluons form a Bose condensate and

are at the maximum density (Condensate). For a more complete introduction to the theory of Color Glass Condensate see Reference [38].

One of the more testable predictions of CGC is that gluon saturation at low x would reduce charm production, which is dominated by gluon fusion, at forward rapidities relative to binary collision scaling. The ratio of forward rapidity charm to mid-rapidity charm would decrease with increasing centrality.

2.5.5 k_T Broadening

In order to account for discrepancies between p_T and azimuthal angle distributions for D meson pairs and those from the expected bare quark distributions in $p + p$ collisions, an intrinsic transverse momentum kick, k_T, was added to account for parton motion in the transverse plane [35]. The k_T is added randomly from a gaussian distribution, $g_p(k_T) = \frac{1}{\pi \langle k_T^2 \rangle_p} \exp(-k^2 / \langle k^2 \rangle_p)$, for which a value of $\langle k^2 \rangle_p = 1$ GeV^2 was found to work well. In nuclear collisions there appears to be a broadening of this intrinsic momentum, likely due to multiple scattering of partons within the nucleus. This broadening is estimated for $p + A$ collisions as a random walk process resulting in $\langle k^2 \rangle_A = \langle k^2 \rangle_p + (\langle v \rangle - 1) \Delta^2(\mu)$, where $\langle v \rangle$ is the average number of binary collisions, Δ^2 is the strength of the nuclear broadening as a function of the scale of the interaction, μ. The value of $(\langle v \rangle - 1) \Delta^2(\mu)$, $\mu = 2m_c$, is estimated to be 0.35 GeV^2 for charm in central $d + A$ collisions with A=200, and scaling $\langle v \rangle - 1$ by 2 corresponds to $A + A$ collisions [35]. The effects of k_T broadening on 158 GeV $p + A$ collisions for various $\langle k^2 \rangle$ values is shown in Figure 2.16.

2.5.6   Timescales and Pre-equilibrium Production

The time evolution of a heavy ion collision, Figure 2.17, likely has an important effect on charm production. In 1992, Muller and Wang proposed that if a dense partonic, ie. deconfined, system was produced in RHIC collisions, significant amounts of charm
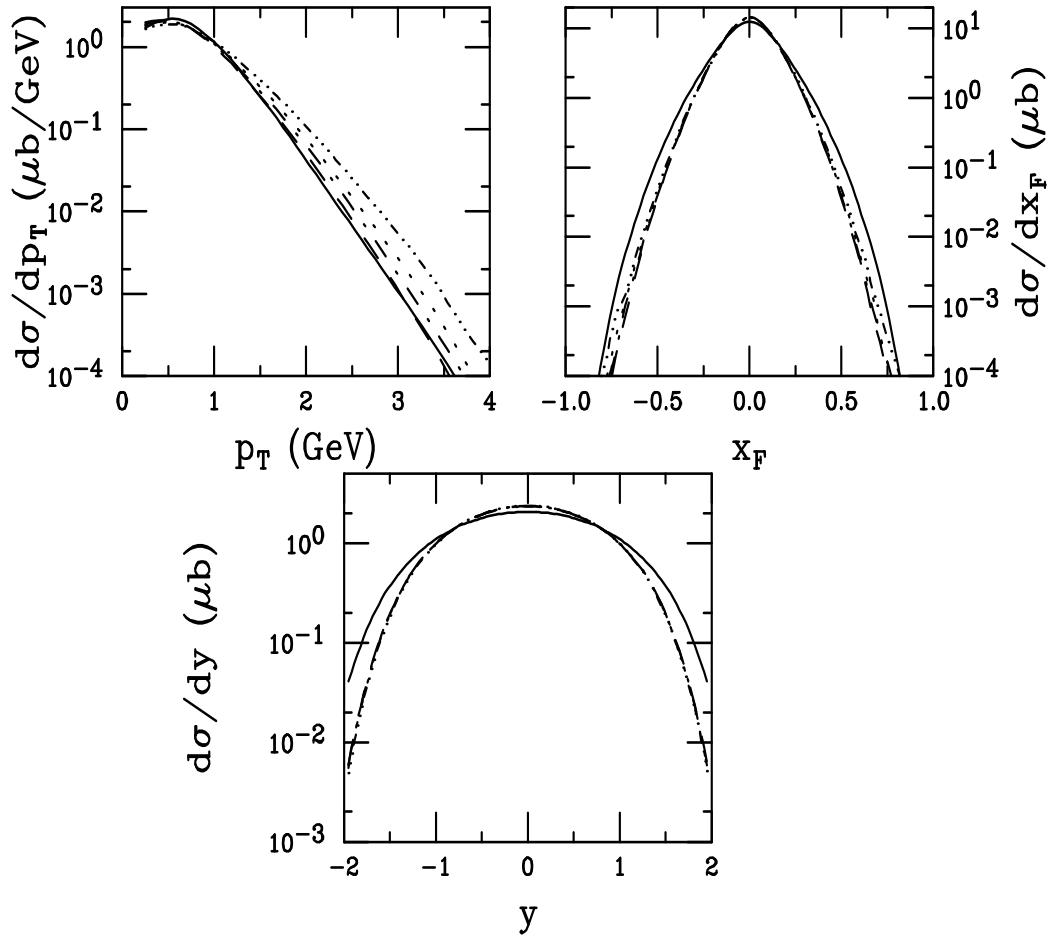
Figure 2.16: The per nucleon cross section for inclusive NLO c quarks in 158 GeV $p + A$ collisions. The solid curves are for bare quarks, $\langle k^2 \rangle = 0$. Other curves include fragmentation and $\langle k^2 \rangle = 1$ (dashed), 1.175 (dot-dashed), and 1.7 (dot-dot-dot-dashed) GeV^2 [35]
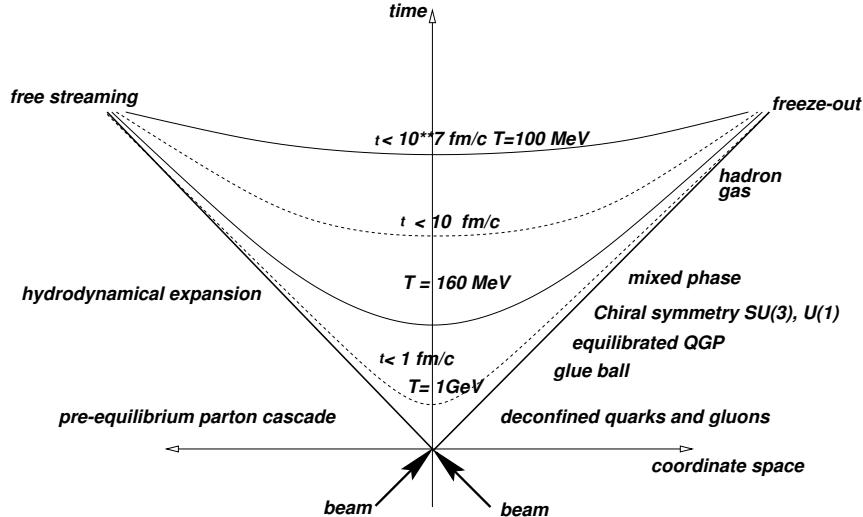
Figure 2.17: Possible time evolution of a heavy ion collision in a QGP scenario. The right side describes the physical state of the system, and the left side describes the framework which is appropriate for simulating the system [39].

could be produced after the initial production. If the amount of charm produced in this "pre-equilibrium" stage is similar to the initial production and if the charmed quarks do not reach chemical equilibrium, the total amount of open charm produced would give a measure of the thermalization time of the dense partonic phase [40]. They then estimated that the pre-equilibrium charm yield would be roughly equal to the initial charm for central $\sqrt{s_{NN}} = 200$ GeV Au+Au collisions as seen in Figure 2.18. Muller and Geiger formed a parton cascade model for simulation of A+A collisions [41] and Geiger published predictions of orders of magnitude enhancement in Au+Au with a QGP. A comparison of the estimates with and without a QGP are shown in Figure 2.19.

Unfortunately, later works by Lin and Gyulassy [42] [43] and Levai, Muller, and Wang [44] concluded that pre-equilibrium charm production would be significantly lower than the initial production, as shown in Figures 2.20 and 2.21. The conclusion is reached by imposing more realistic $\eta - y$ or space-momentum correlations. These

31
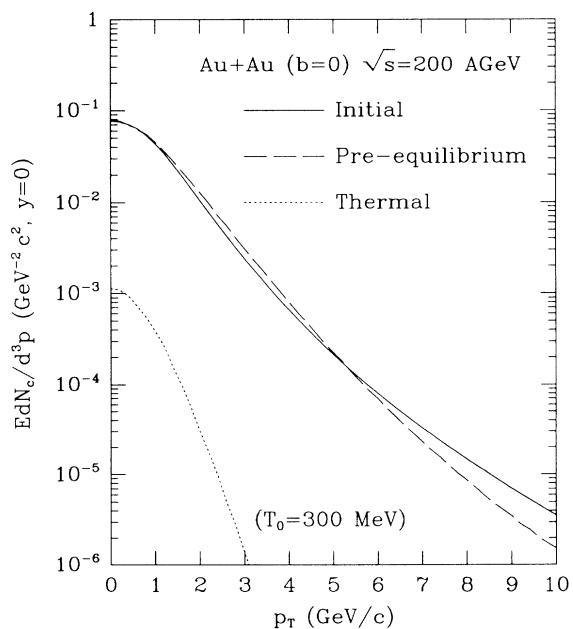
Figure 2.18: Early estimate of pre-equilibrium contribution to open charm production in a heavy ion collision. The estimate does not take into consideration space-momentum correlations.[40]

Au+Au with QGP Au+Au w/o QGP
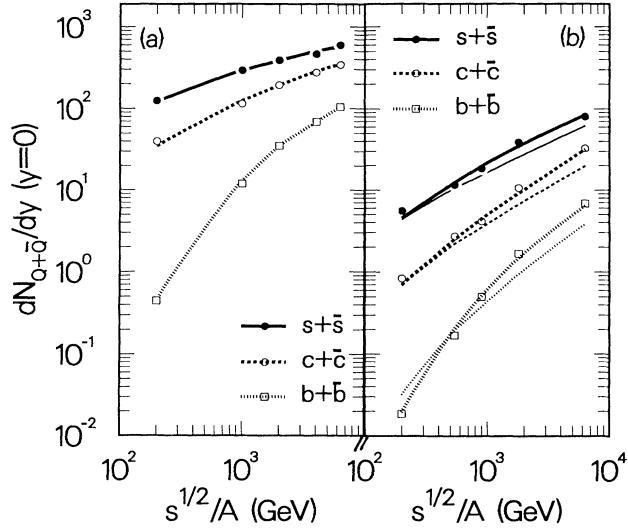
Figure 2.19: Parton cascade model predictions for energy dependence of heavy quark production in heavy ion collisions[41]. The estimate does not take into consideration space-momentum correlations.
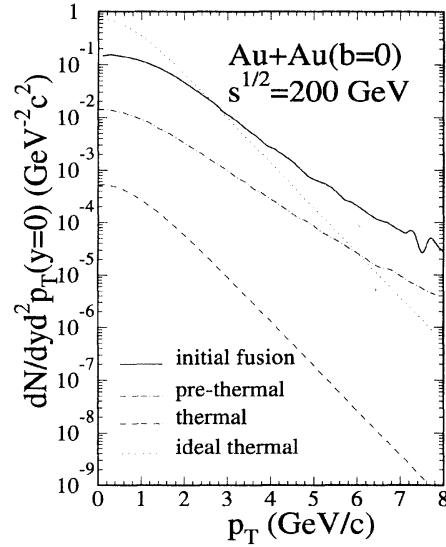
Figure 2.20: Charm production at different stages of a Au+Au collision after considering space-momentum correlations.[44]

33
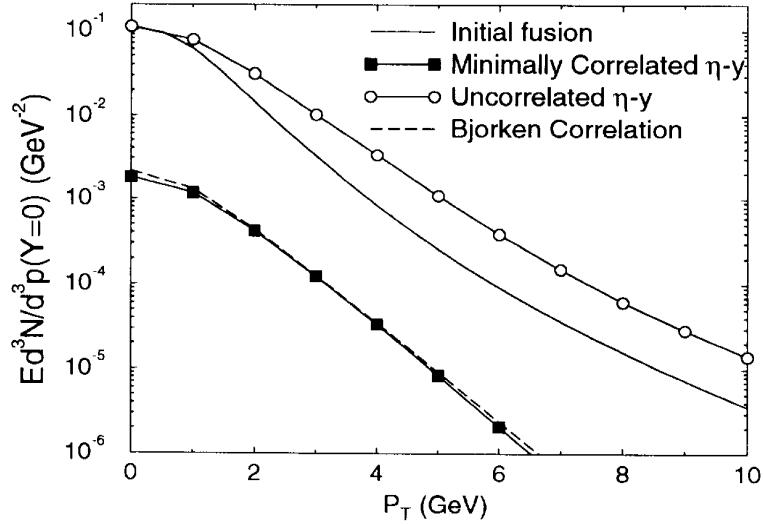
Figure 2.21: Charm production at different stages of a Au+Au collision assuming different space-momentum correlations. [42]

correlations limit which particles can interact with which particles to a more physical picture. The minimal correlations imposed by the uncertainty principle lead to roughly a factor of 40 reduction in the pre-equilibrium charm production. Muller suggests that large pre-equilibrium charm production is still a possibility if initial parton densities are much higher than expected, ie. 4 times HIJING, shown in Figure 2.22. Lin and Gyulassy also give an explanation for the discrepancy between [40] and [41].

2.6   Open Charm as a Charmomium Reference

As discussed earlier, J/ψ production has the potential to act as a probe of color deconfinement. In the past, J/ψ suppression has been measured relative to the Drell-Yan continuum, but this method is beset with serious issues for comparisons of data at different $\sqrt{s}$ and with different atomic number A [45]. These issues are primarily due to the very different production mechanisms for charmonium and Drell-Yan. While charmonium is primarily produced via gluon-gluon fusion, as discussed earlier in this
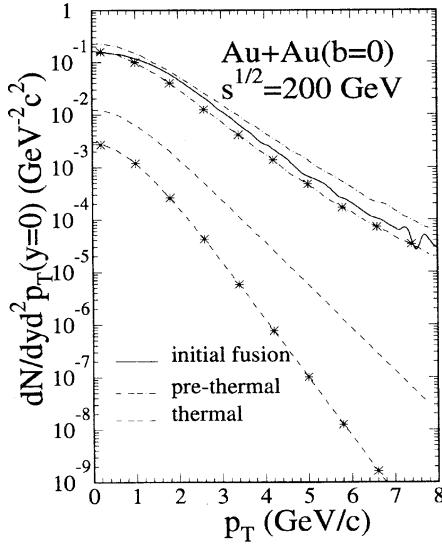
Figure 2.22: Charm production estimate with space-momentum correlations at different stages of a Au+Au collision using 4x HIJING parton densities. [44]

chapter, Drell-Yan is the decay of a virtual photon from $q\bar{q}$ annihilation into a lepton pair. This means that a ratio of J/ψ to Drell-Yan is dependent on the valence quark, sea quark, and gluon structure functions. Since these exhibit different behavior at different x, which would be probed by varying collision energies, comparisons of data for significantly different energies would be difficult. In addition, valence quarks, sea quarks, and gluons have different shadowing properties, making comparisons of data with different atomic numbers difficult. Much of this difficulty would be relieved by measuring J/ψ relative to open or total charm. Since charmonium and D production are both dominated by charm pairs produced from gluon fusion, the importance of the quark structure functions are greatly diminished. Also, if the charmonium and open charm are both produced over a small enough range in x, then any shadowing effects, such as the estimate of Schmitt et. al. [36] described above, will become negligible. An estimation using open charm and J/ψ as charmonium references is shown in Figure 2.23. This estimate shows that the J/ψ to Drell-Yan ratio should continually increase

35
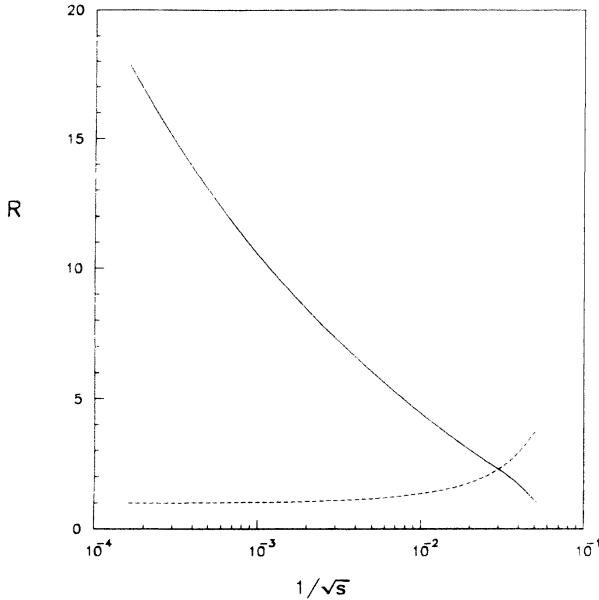
Figure 2.23: Estimation of the energy dependence of the J/ψ to open charm ratio (dashed) and the J/ψ to Drell-Yan (solid). The ratios are normalized to their values at $\sqrt{s} = 20$ GeV (Drell-Yan) and $\sqrt{s} \rightarrow \infty$ (open charm). [45]

with increasing energy, while J/ψ to open charm should approach a constant value at high energies.

2.7 Open Charm Enhancement?

In 1995 the NA45 (CERES) experiment at the CERN SPS observed an enhancement of low mass electron pairs in 200 GeV/nucleon $S + Au$ collisions [46] over scaling from $p + A$ collisions. NA45 had collected data for $p + Be$ and $p + Au$ at 450 GeV, and were able to describe the invariant mass distributions with a combination of expected sources, but extrapolation to $S + U$ failed to describe the data, Figure 2.24. Work was done to determine the amount of open charm enhancement needed to reproduce the data, if it could at all. Using the PYTHIA [48] event generator which reproduced the p-Be and p-Au well, Braun-Munzinger et. al. estimated that open charm produc-

36
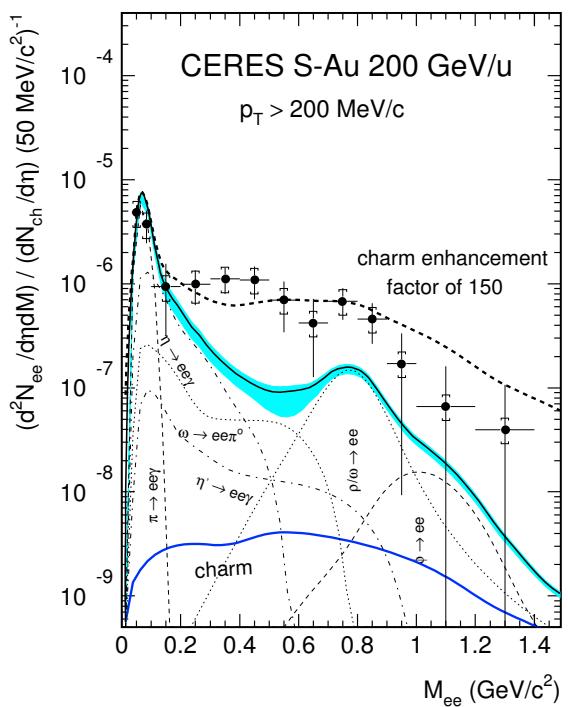
Figure 2.24: Electron pair invariant mass spectrum from the NA45 experiment. The data is significantly under predicted at low mass by scaled sources which describe $p+A$ data well.[47]
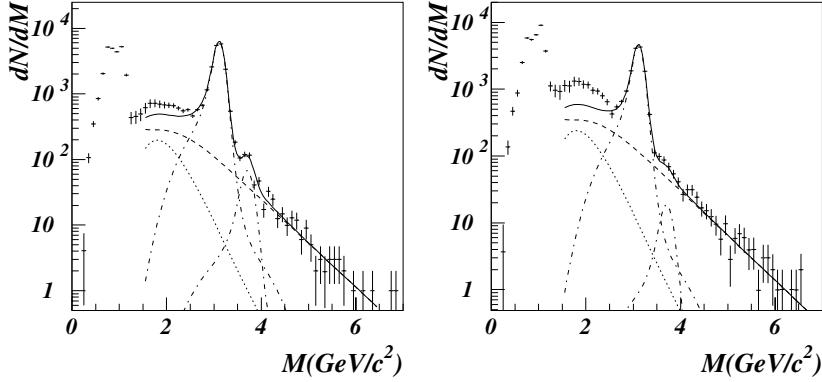
Figure 2.25: Comparison between data and expected sources for peripheral and central Pb-Pb collisions. An excess is seen in the intermediate mass region. [51]

tion would need to be increased by a factor of 150 to best fit the data [47]. The same PYTHIA parameters were then used to simulate NA38 and NA50 dimuon invariant mass spectra from $p + U$, $S + U$ and $Pb + Pb$ collisions, Figure 2.25. The simulations matched the $p + A$ data well, but a significant excess was observed from around 1.5-2 GeV/c^2 for $A+A$ collisions. This excess could be accounted for by a charm enhancement of up to 3. An upper bound of around 3 relative to 150, meant that open charm enhancement was not the primary source of the NA45 enhancement. The enhancement in the dimuon spectra, and the possibility of charm enhancement it implies, are still of great interest to the heavy ion physics community. The low mass enhancement here and in later CERES(NA45) measurements has fueled the interesting subject of in-medium modification of the ρ mass [49][50]. A detailed study of the NA50 excess and its implications for charm enhancement was done by the NA38 and NA50 collaborations [51]. The charm enhancement required to fit the intermediate mass region as a function of the number of participants is shown in Figure 2.26. The $p + A$ data was used to extract a cross-section of $\sigma_{c\bar{c}}^{pp} = 36.2 \pm 9.1$ μb which is quite consistent with both higher and lower energy data [51]. Two leading theories for the sources this enhancement are hadronization of charm pairs with $m_{c\bar{c}} < 2m_{\mathrm{D}}$ [52] and thermal di-leptons [53]. Recent
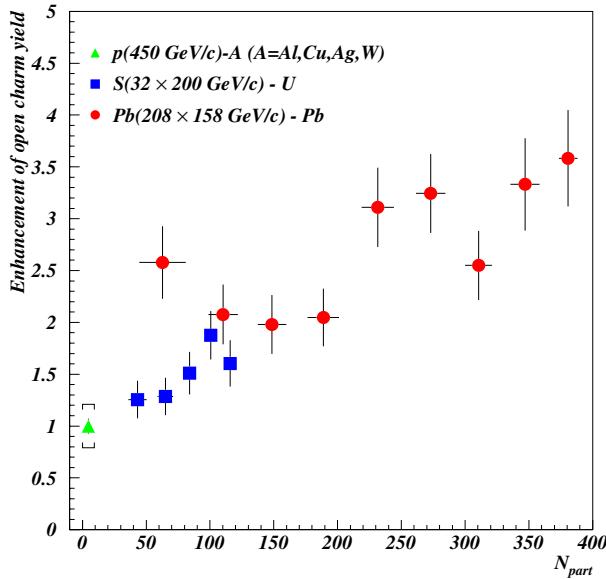
Figure 2.26: Participant dependence of the charm enhancement factor needed to reproduce the intermediate mass region of the NA50 di-muon spectra.[51]

measurements at RHIC of relevance to this topic are discussed in Chapter 6.

One possibility which allows for a greater amount of open charm enhancement at SPS energies than at RHIC energies was presented by Kostyuk et. al. [52]. They argue that in a deconfined medium, such as a QGP, charmed quarks created below the threshold for producing charmed mesons in a vacuum, $2m_D$, can interact with quarks in the medium and coalescence into D mesons. As seen in Figure 2.27, a greater fraction of $c\bar{c}$ pairs is produced above $2m_D$ at RHIC energies, so enhancement from sub-threshold pairs would be significantly reduced from that at SPS energies. As seen in Figure 2.28 this enhancement could be as much as a factor of 6 at the SPS and 2 at RHIC. As the authors make clear, the calculations only represent rough upper limits to such an effect. It is of experimental interest to note that this effect appears even more pronounced for bottom production.

Also, measurements are being undertaken at the SPS by NA60 which will give a direct measure of open charm and should clarify the possibility of open charm en-
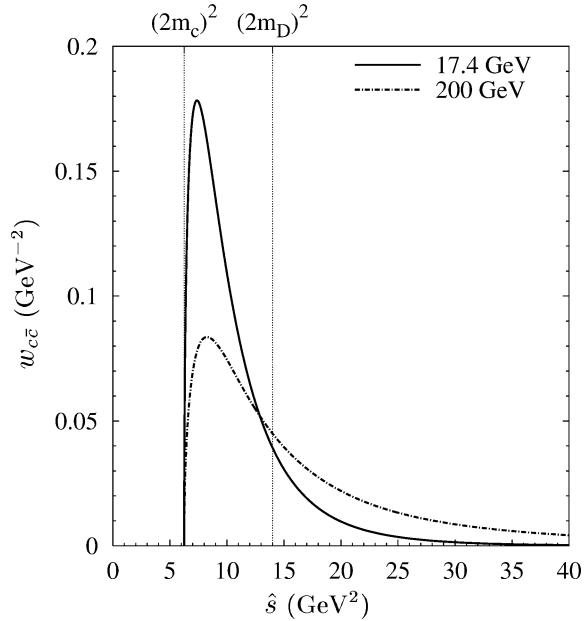
Figure 2.27: The exitation function for $c\bar{c}$ pairs created in a hadronic collision for SPS and RHIC energies [52]. The region below $(2m_D)^2$ cannot contribute to open charm via fragmanetion. Hadronization through coalescence in a deconfined medium could allow this region to result in open charm mesons.
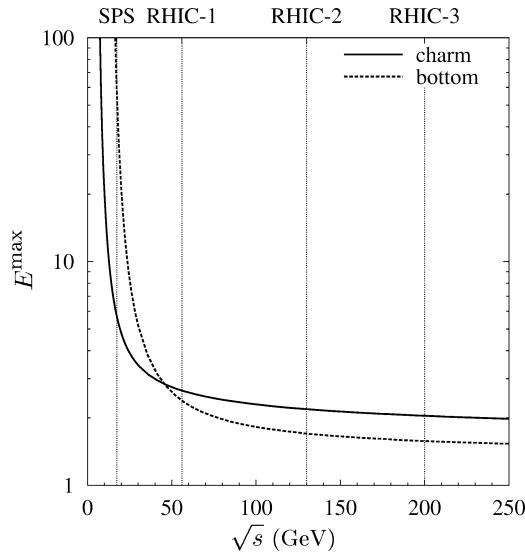
Figure 2.28: The energy dependence of the maximum open charm and bottom enhancement assuming hadronization via coalescence allows all charm to form D mesons [52].

hancement at SPS energies.

2.8 Coalescence

The importance of hadronization of charm quarks into D mesons via coalescence with pre-existing quarks was previously demonstrated for $A + A$, as a possible method for charm enhancement, as well as in $p + p$ collisions, but coalescence production may have other important consequences. In the deconfined media of a QGP, it is reasonable to assume that coalescence, as opposed to fragmentation, is the dominant form of hadronization for D mesons. Under these assumptions, the relative abundances of D mesons should provide a good probe of the chemical content of the QGP [54]. For a QGP with a chemical potential of zero all D mesons should have nearly the same yield. Specifically, for a free relativistic fermion quark gas at T=200 MeV and a baryon chemical potential, $\mu = 0$, $\frac{D_s^-}{D^-} = 0.94$ [55]. In contrast, an equilibrated hadronic bose gas at T=180 MeV is expected to only have $\frac{D_s^-}{D^-} = 0.610$ [55]. One complication is that final state interactions such as $D^\pm + K^\pm \rightarrow D_s^\pm + \pi^\pm$ could modify the ratios, and would need to be corrected for.

The sensitivity of various probes to differentiate between c quarks from 200 GeV $Au + Au$ collisions with momentum distributions from pQCD (PYTHIA) versus complete thermalization with radial and elliptic expansion was evaluated by V. Greco et. al. using a coalescence model [56]. In particular, the ability of D mesons and their decay electrons p_T spectra and elliptic flow to differentiate between the two scenarios was studied. As shown in Figure 2.29, the D meson p_T spectra can differentiate the QGP and non-QGP scenarios but only at high and low p_T, and the decay electrons have less discriminating power. Figure 2.30 demonstrates the more promising capabilities of D flow measurements. Also, the decay electrons show a closer correlation to the parent D distribution in the flow measurement.
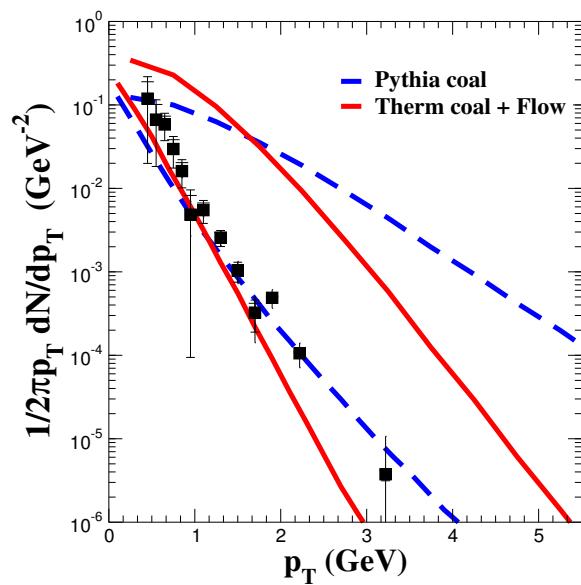
Figure 2.29: Estimates from a coalescence model for mid-rapidity transverse momentum distributions for *D* mesons, upper curves, and their decay electrons (lower curves), produced in $\sqrt{s_{NN}}$ = 200 GeV central Au+Au collisions. The solid lines are for thermal *c* quarks, QGP case, and the dashed represent those from pQCD, non-QGP. [56]
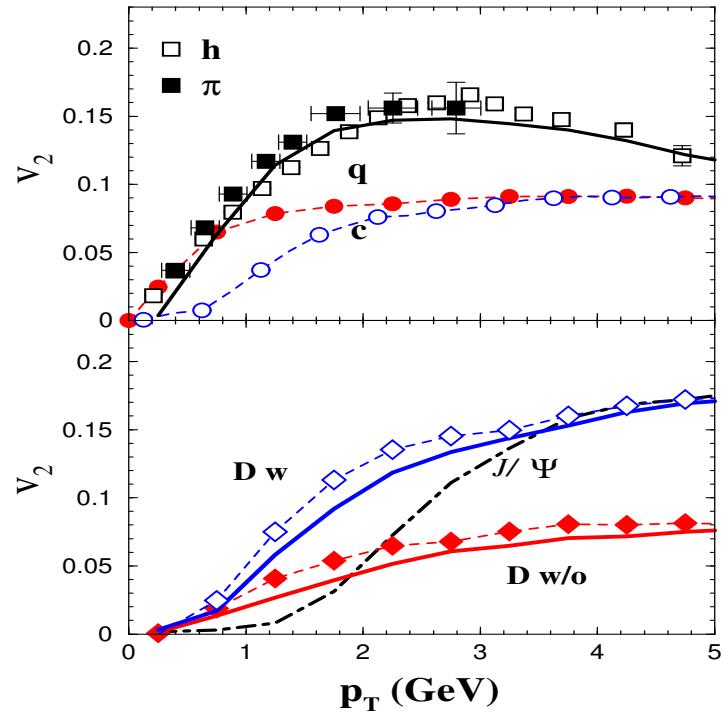
Figure 2.30: Coalescence model estimates for elliptic flow in minimum bias Au+Au collisions at $\sqrt{s_{NN}}$= 200 GeV [56]. The lower panel shows D-mesons (solid lines) and their decay electrons (diamonds) for pQCD charm-quark distributions (D w/o), and for thermal+flow c-quark spectra at T_c (D w). The J/ψ (dash-dotted line) is also shown for thermal+flow. The large difference in the flow parameter v_2 between the two scenarios, even at relatively low p_T, make this a promising signal.

43

Chapter 3

The PHENIX Experiment

3.1 The RHIC Facility

The Relativistic Heavy Ion Collider (RHIC) located at Brookhaven National Laboratory is currently the premier facility for high energy heavy ion research. This was the first facility in the world whose primary purpose was the study of heavy ion collisions. RHIC was first conceptualized in 1983 and construction began on the project in 1991 with a project budget of $616.6M. BNL was an ideal location for RHIC since a tunnel and other infrastructure were already in place from earlier projects. In 1978, construction began on ISABELLE, a machine design consisting of intersecting proton storage rings, but problems with superconducting magnets stopped the project in 1981. Construction of the RHIC facility was completed in 1999 and first collisions were observed in June 2000. Please see [57] for more on the history of RHIC.

RHIC consists of two 3.8km superconducting magnet rings with six points of intersection where collisions can occur. Four of these interaction regions, or IRs, are now instrumented with experiments: PHOBOS, BRAHMS, STAR, and PHENIX. PHOBOS is named after a moon of Mars because it is a scaled back version of the proposed MARS detector. PHOBOS specializes in using silicon technology to measure low-p_T charged

particle multiplicities. BRAHMS, which stands for Broad Range Hadron Magnetic Spectrometers, uses two rotateable spectrometers to measure charged hadrons over a large range of rapidity and momentum. STAR, the Solenoidal Tracker At RHIC, uses a large time projection chamber to track charged particles over a large geometric acceptance at a relatively low rate. PHENIX, the Pioneering High Energy Nuclear Interaction eXperiment, uses various types of complementary detectors to study hadrons, photons, and leptons at high event rate. PHOBOS and BRAHMS are smaller experiments with on the order of 100 collaborators each, while STAR and PHENIX are significantly larger and approach 500 collaborators each. Although much ability for cross checks exists, each of the experiments at RHIC has a unique focus and implementation for studying the collisions.

The collider is capable of accelerating many species of ions from p to Au to an energy of 100 GeV per nucleon, thus achieving $\sqrt{s_{NN}} = 200$ GeV collisions. It is important to note that each ring can accelerate different ion species allowing for asymmetric collisions. The reader may notice in Figure 3.1 that the Alternating Gradient Synchrotron, which has previously made numerous contributions to the fields of high energy and heavy ion physics and continues to be an active research facility, is used in the RHIC facility to accelerate ions before they enter the collider rings. After more than 10 years of development, RHIC began operations in 2000 with $\sqrt{S_{NN}} = 130$ GeV $Au + Au$ collisions, but data from the 2001-2002 RHIC running period will be the focus of the research presented here.

3.2 PHENIX: An Introduction

PHENIX was designed with two main physics goals: investigation of Quark Gluon Plasma and measurement of the spin structure of the nucleon. PHENIX has the ability to search for and, if found, characterize a QGP through many channels. A few of the
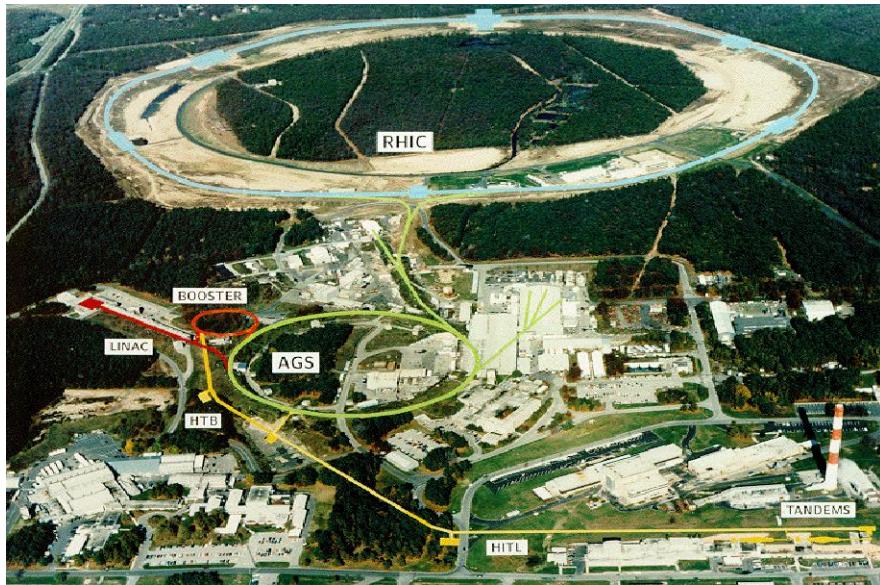
Figure 3.1: An aerial view of the Relativistic Heavy Ion Collider Facility.

more prominent ones are listed here. Direct photons and lepton pairs are sensitive to the initial state. Lepton pairs can be used to study J/ψ, Ψ' and Υ yields, which give insight into Debye screening, and ϕ, ρ, and ω yields, which should be sensitive to chiral restoration. High p_T leading hadrons are used to study jet production, which is sensitive to the density of the medium. Hadrons are also used in HBT correlation studies. These signals are studied in $p + p$ and d+Au as well as Au+Au collisions to understand and account for hadronic effects. W particles identified through high p_T (> 20 GeV/c) electrons and muons, as well as high p_T prompt photon production will be used to study the spin structure of the nucleon.

PHENIX consists of a collaboration of over 450 scientists and an experimental apparatus which weighs approximately 4000 tons. This complex experiment, shown in Figure 3.2, contains over a dozen subsystems which work together to capture vast amounts of information from the collisions RHIC provides. PHENIX can be described as a combination of global detectors which allow event characterization, a set of central, or mid-rapidity, spectrometers which examine hadrons, photons and electrons, and
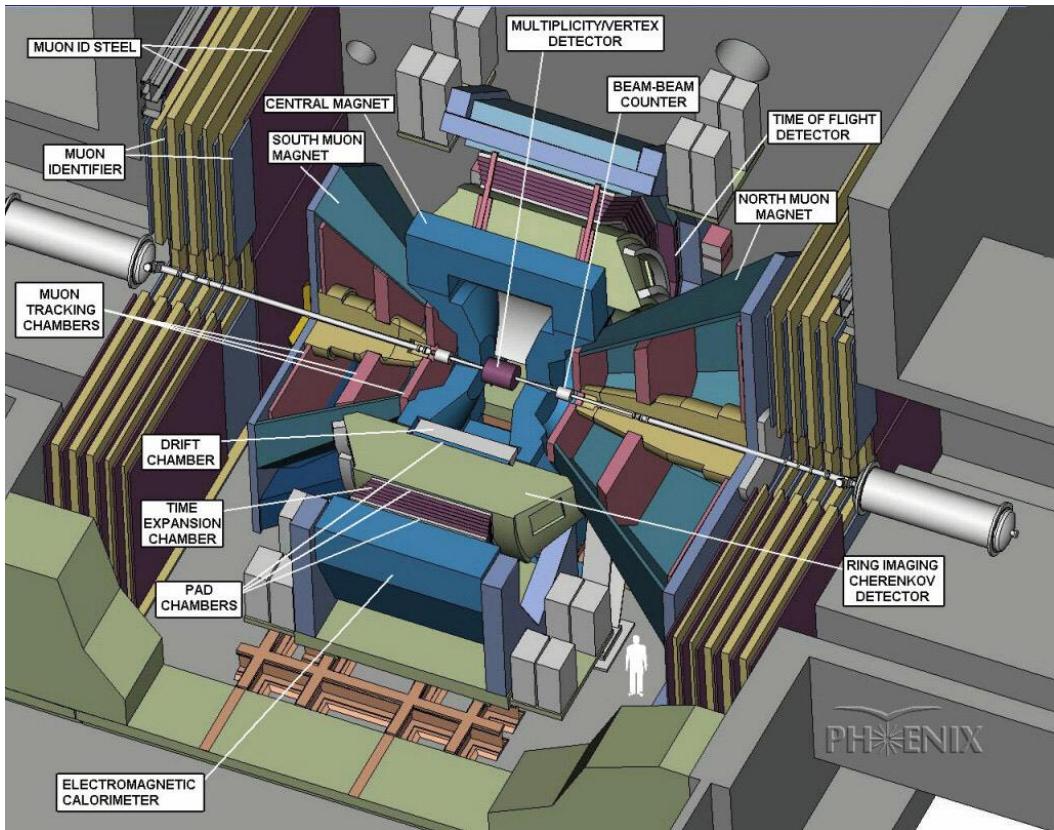
Figure 3.2: The PHENIX Experiment. The major subsystem are labeled. A wedge of the detector has been cut away to show the internal structure. North to south is right to left in the figure.

a pair of forward spectrometers which track and identify muons.

3.3 The Muon Spectrometers

As mentioned above, leptons play a significant role in both the PHENIX heavy ion and spin physics programs. In particular, muons are used in a number of faculties including the study heavy quark and W production. The ability to measure identified muons is unique to PHENIX among the RHIC experiments. Muons are measured at forward and backward rapidities by two muon spectrometers. As shown in Figure 3.2 each of the two muon spectrometers, often referred to as muon "arms", is comprised of a muon tracker, which uses planes of cathode strip chambers in a magnetic field to provide precision momentum information, and a muon identifier, which uses layers of absorber and streamer tubes to aid in the differentiation of muons from hadrons. Although the north and south muon identifiers are geometrically very similar, the south tracker is somewhat smaller, 1.5 m shorter in z and smaller angular acceptance, than the north in order to facilitate removal from the experiment hall. Only the south muon spectrometer was operational for RHIC Run II, 2001-2002, but both were operational for Run III, 2003. As can be seen in Figure 3.3, the muon spectrometers are designed to have complete azimuthal coverage and significant forward acceptance (y $\approx$ -1.2 to -2.2), and the addition of even a single muon arm greatly increased the acceptance of the PHENIX experiment.

3.3.1 The Muon Tracker

The principle design goal of the PHENIX muon trackers was the clear separation of neighboring resonances J/ψ and ψ', Υ(1S) and Υ(2S,3S), and ρ/ω and ϕ with good enough signal-to-background to allow measurements on the scale of a RHIC run. This translates to a spatial resolution of approximately 100 μm. While background reduc-
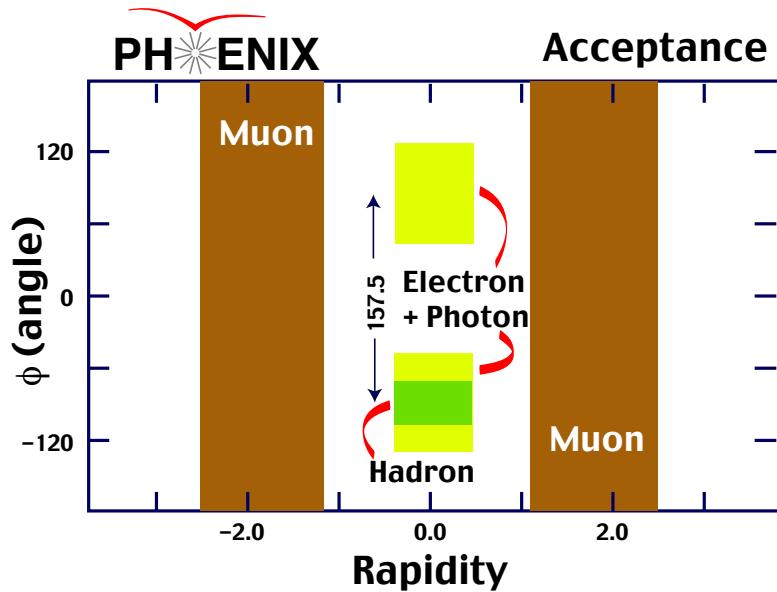
Figure 3.3: Acceptance for various particles of the PHENIX central and forward spectrometers. The south muon arm covers y ≈ -1.2 to -2.2, and the north covers y ≈ 1.1 to 2.4

tion is important to the MuTR, much of this responsibility falls to the Muon Identifier as discussed in the next section. The trackers also needed to be able to handle the occupancy challenges of Au+Au collisions in addition to the event rate challenges of $p + p$. Physical constraints of the experiment hall and funding constraints were also important factors in MuTR design.

Tracking Chamber Design

Each MuTR contains three cathode strip chamber tracking stations which are enclosed in the steel housing of the muon magnet as shown in Figure 3.4. Each of the three stations is composed of three layers, or "gaps" with each gap being a sandwich of cathode strips, anode wires, cathode strips, so each station has a total of 6 cathode layers, two per gap, which can be read out. Only 2 gaps of station 3 were installed due to lack of funding. Every other cathode strip is read out for each gap. Each of the stations
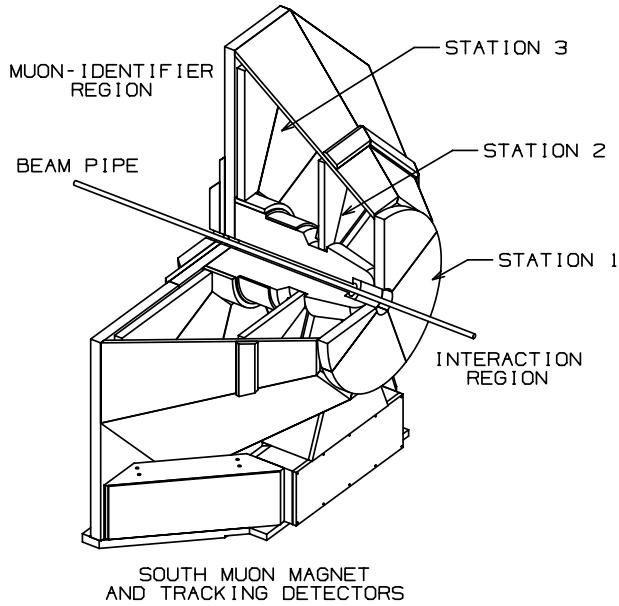
Figure 3.4: Sketch of the South Muon tracker design. A wedge of the detector has been cut away to show internal structure. Notice the octagonal structure of the detector.

is actually separated into eight equal sections or octants. For stations two and three, the octants are completely separable from each other, while station one, the smallest station, is constructed as four physical quadrants; each of which is electrically divided into two octants. Each octant is constructed in the three gap structure described above and sketched in Figure 3.5. For each gap, the wires of the anode plane run roughly azimuthally, the strips of one cathode layer, the "straight" layer, run perpendicular to the anode wires, and the strips of the other cathode layer, the "stereo" layer, are rotated by a small angle ($<$ 12º) with respect to the straight layer. See Table 3.1 for precise stereo angle values. The cathode strips are 5mm wide copper made by creating separations in a continuous copper coating. This was achieved with photolithography, electro-mechanical etching, and mechanical routing for stations 1, 2, and 3 respectively. The cathode planes are separated by 6.35 mm with the anode plane located midway between. The anode planes are alternating 75 μm gold-plated Cu-Be field wires and 20

50
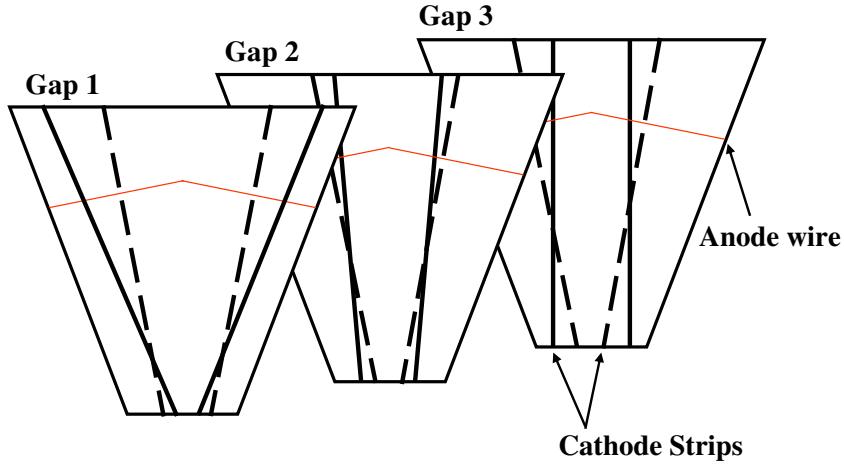
Figure 3.5: Figure of the structure of an example Muon tracker octant. The anode wire plane is between two cathode planes in each gap. Strips in stereo cathode planes are shown as solid lines. Stations 1 and 3 are stacked stereo, straight, stereo ... while station 2 is stacked straight, stereo, straight ...

Table 3.1: The angle of rotation of the stereo plane relative to the straight plane is shown for the first half-octants of each station and gap; the stereo layers of the second half-octants are a reflection across the half-octant boundary. A plus sign represents the positive ϕ direction.

Station	Gap	angle (degrees)
	1	-11.25
1	2	+6
	3	+11.25
	1	+7.5
2	2	+3.75
	3	+11.25
3	1	-11.25
	2	-11.25

51

μm gold-plated W sense wires. The sense wires have a spacing of 1 cm. The anodes are not currently read out due to budget constraints.

The outer stations, 1 and 3, are constructed using honeycomb panels that are laminated with copper clad FR-4 sheets. The inner station, station 2, uses 25 μm mylar foils with a 600 Å copper coating for cathode planes. This gives a total thickness of $8.5\text{x}10^{-4}$ radiation lengths, which allows for the low amount of multiple scattering needed to maintain good momentum resolution down to 1.5 GeV. The station 2 z-position was chosen to roughly coincide with the position of maximum displacement from a linear path for high momentum (10 GeV) muons.

The MuTR chambers are operated with a 50:30:20 mixture of Ar:CO_2:CF_4, and at a bias of 1.85 kV. The gas is non-flammable and has a wide efficiency plateau. This mode of operation provides a gain of $2\text{x}10^4$. For stability, the operating voltage is actually closer to 1.7 kV, but this provides similar performance.

MuTR Read Out

Approximately 21,000 cathode strips from the south MuTR are read out through the system's Front End Electronics (FEE). The signal from each cathode is carried over a 45-60 cm cable to a FEE crate. Spatial constraints prevented placing preamplifiers inside the magnet with the chambers to reduce noise. The signal cable is connected to the Cathode Preamplifier (CPA) chip of a Cathode Readout Card (CROC). The CROC then stores the signal in one channel of a 32 channel Analog Memory Unit/Analog to Digital Converter (AMUADC) chip. Each CROC houses 8 CPA chips, each of which has 8 channels, and 2 AMUADC chips. Two CROCs are connected to a controller card via the crate backplane. This combination is referred to as a Front End Module (FEM), and the south MuTR utilizes 168 FEMs.

Each controller card has an ARCNet interface, used for slow controls, a CLink receiver, for fast timing signals from the Granual Timing Modules, and a CLink trans-

mitter, for sending data to the Data Collection Modules. The copper wire Clink signals are actually converted to GLink fiber signals after a 7 m cable. ARCNet is used for slow control and provides a number of functions including: configuration of CPA and AMUADC chips, configuration and programming of FPGA, communication with voltage and temperature monitors, and providing the reset signal for the Glink communication. The system allows for 4 event buffering capability and will increase to 5 event buffering in the future. An overview of the MuTR FEE system is shown in Figure 3.6.

Each chamber gap has four calibration wires which overlaps all of the cathode strips and is connected to a digital to analog converter (DAC). Sending signals from the DAC simultaneously induces a charge on all of the chamber cathodes. This is used to study each channels gain for a variety of pulse heights. Data with no signal from the DAC are taken periodically to measure the channel pedestals.

Magnet Design

The magnetic field for the muon trackers is provided by a north and south muon magnet (NMM and SMM respectively). Each magnet is composed of an iron piston which surrounds the beam pipe. A current is passed through a coil at the base of the piston to energize the magnet. The remainder of the magnet is comprised of an iron "8 sided lampshade" and a 20 cm (30 cm for north) thick steel back plate, which also serves as the first absorber layer of the muon identifier, as seen in Figure 3.4. This arrangement produces a roughly radial magnetic field which has a field integral which is approximately inversely proportional to θ, polar angle from the beam axis. A view of the field lines can be seen in Figure 3.7. As mentioned above, the SMM is smaller than the NMM. In order to achieve a similar $\int \vec{B} \cdot \vec{dl}$, 0.72 Tm at $\theta = 15^{\mathrm{o}}$, the SMM piston needed to be larger, in polar extent, than that of the north to keep from saturating the piston. The NMM piston extends 10° in θ while the south piston is 12°. The muon magnets were designed to provide the largest reasonably achievable acceptance, have
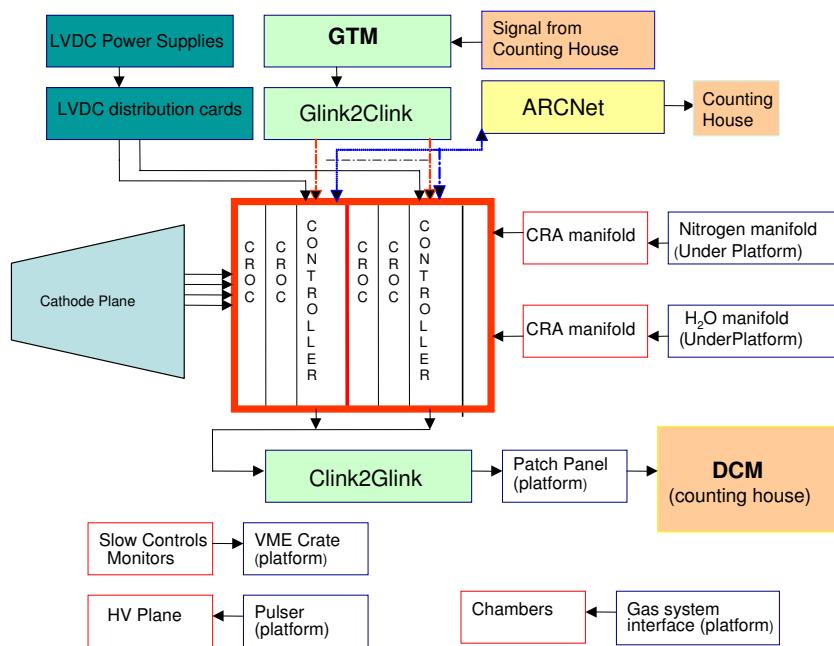
Figure 3.6: Diagram of the Muon tracker Front End Electronics. Signals are read out from the cathode planes by Cathode Readout Cards. When a trigger is received, the controller cards send event data to the DAQ's Data Collection Modules.[58].
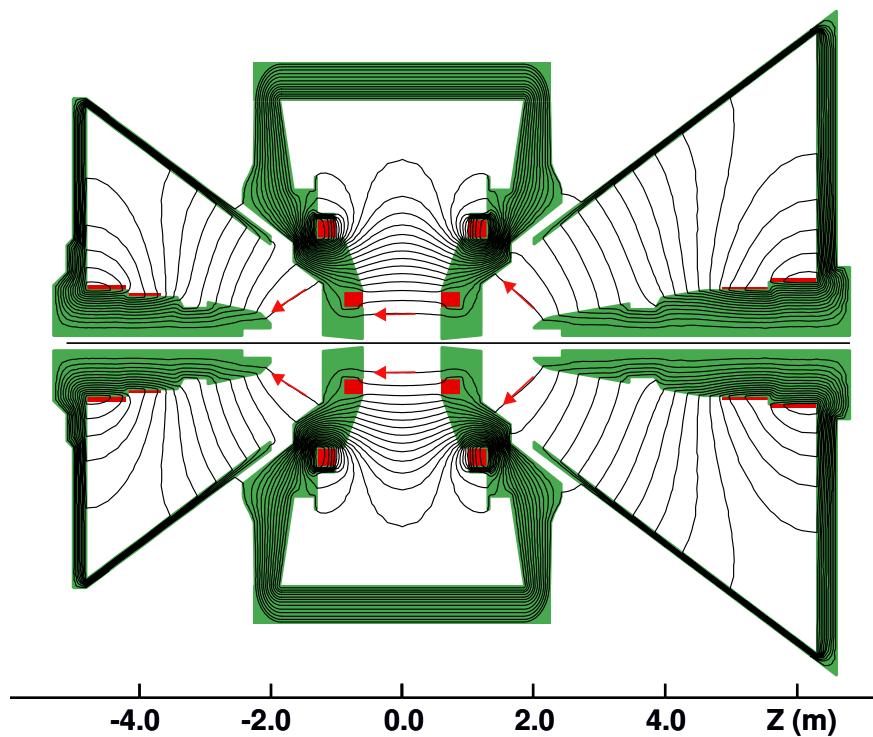
Figure 3.7: Magnetic field of the muon and central magnets from 2D TOSCA simulations. The field in the muon magnets is roughly radial.

Table 3.2: Maximum physics performance of the muon magnets.

	MMN	MMS
Acceptance of $\phi \to \mu^+\mu^-$	0.0058	0.0023
RMS mass resolution for $\Upsilon \to \mu^+\mu^-$	190 MeV/c^2	240 MeV/c^2

a minimal impact on RHIC operations, and produce a fairly uniform field. The maximum physics performance of the magnets for the ϕ and Υ are shown in Table 3.2. For a detailed description of the field mapping procedure and other magnet details please consult reference [59].

Performance

The position of a particle is determined at each cathode plane by fitting the charge distribution induced on neighboring strips when charge from ionized gas is collected on the closest anode wire. The distribution of the induced charge on the strips is a product of detector geometry and can be well described by the Mathiason function. An example of this charge distribution can be seen in Figure 3.8. The charge is most likely to be distributed across three instrumented strips, only every other strip is read out as described above. The shape of this distribution, i.e. the fit to a Mathiason function, determines the position of the particle to a much higher accuracy than the 1 cm separation between read-out strips.

Before the cathode strip chambers were installed at PHENIX, the performance of an instrumented south station 2 octant was assessed using cosmic rays. The octant was sandwiched between two scintallators which provided an event trigger. Hits from 5 of the 6 cathode planes were used to reconstruct cosmic tracks. Those tracks which were roughly perpendicular to the chamber face were projected to the unused plane. The distances between the hit positions predicted by the projection and the recorded
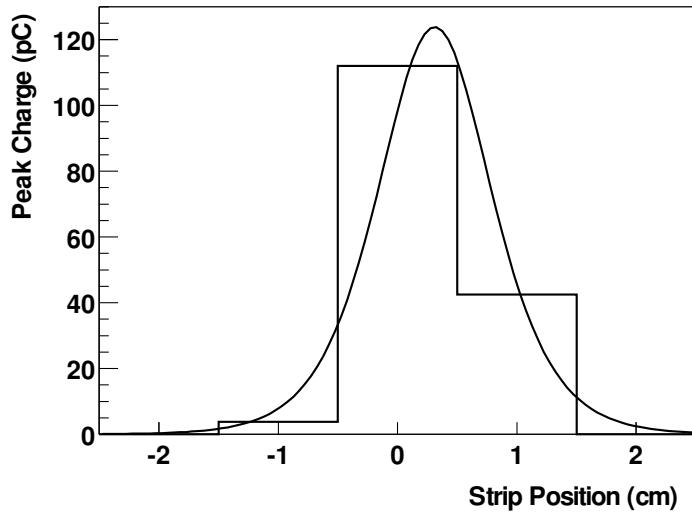
Figure 3.8: Charge distribution on neighboring cathode strips. The distribution is fit to a Mathiason function.

hit positions, referred to as residuals, give a measure of the chamber resolution. The distribution of the residuals, shown in Figure 3.9, indicate a resolution of approximately 130 μm, which is relatively close to the 100 μm design goal.

3.3.2 The Muon Identifiers

The MuTR alone can, in theory, be used for physics measurements such as observing a J/ψ invariant mass peak, especially in low occupancy environments like $p + p$, but the signal to background would likely be crippling, especially in high occupancy Au+Au data. The signal to background of such a measurement would be greatly increased by eliminating a significant number of the tracks due to non-μ particles. Also, the MuTR would be difficult to instrument for the PHENIX level 1 trigger system. A level 1 muon trigger is of critical importance for studying rare processes, particularly in high luminosity $p + p$ running. The PHENIX Muon Identifiers (MuIDs) are designed to cope with these challenges.
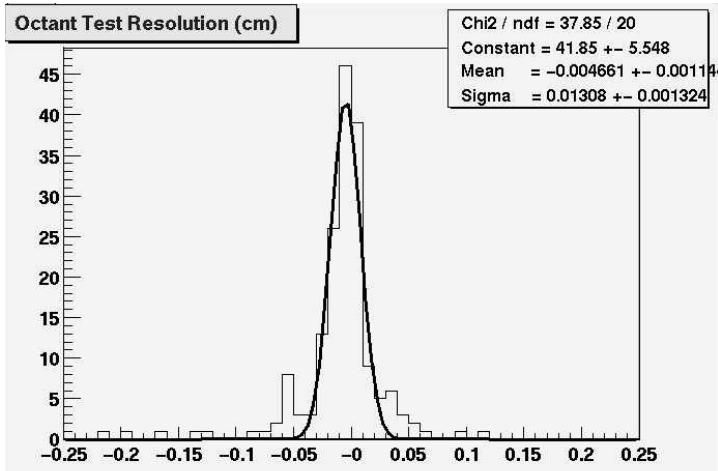
Figure 3.9: Residuals of the South Muon Tracker Station 2 from cosmic ray tests. As seen from the fit, the resolution is roughly consistent with the 100 μm design goal.

Detector Design

Since muons only interact electromagnetically while hadrons can interact strongly and electromagnetically, muons are capable of penetrating much larger amounts of material. This is the primary method employed by the MuID to separate muons from other particles. The first line of defense against the copiously created pions and other non-muons are the pole tips of the PHENIX central magnet. The pole tips begin at ± 40 cm from the nominal interaction point, and they consists of a 20 cm thick brass "nosecone" followed by 60 cm of low-carbon steel. The nosecones were designed to avoid significantly degrading the momentum resolution for low momentum muons and the mass resolution of the J/ψ. The combination of the nosecone and central magnet steel acts as an absorber to stop roughly 99 out of 100 pions, or the particles they may produce, from becoming false "muons".

Before reaching the nose cone, approximately 1 in 1000 pions will decay with one of its products being a muon, but this is of course dependent on the collision vertex position. These decays translate to irreducible μ/π ratio of 10^{-3} for collisions at the
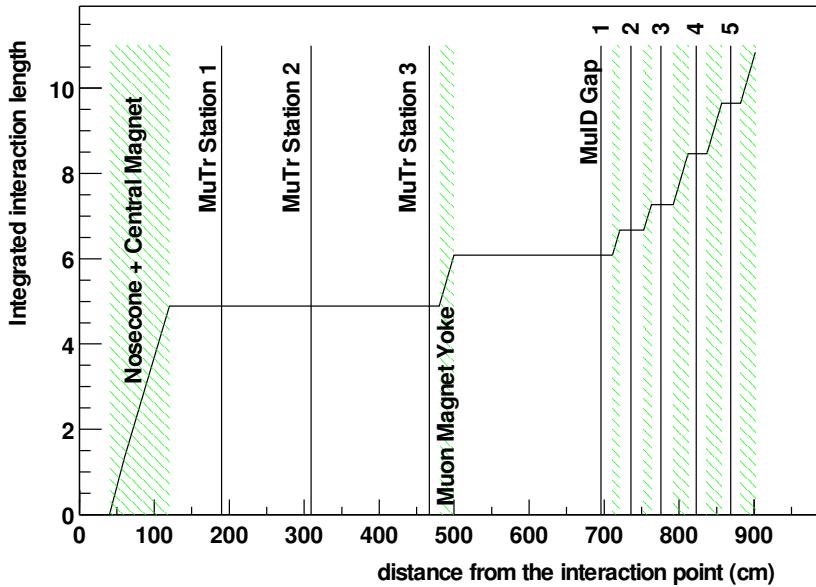
Figure 3.10: South arm distribution of absorber material in integrated interaction lengths. The north arm is the same except for the interaction lengths added by the magnet yoke.

nominal interaction point. The design goal of the MuID is to make this irreducible, on an single event basis, background the dominant physics background.

Each of the PHENIX muon identifiers is comprised of five gaps instrumented with Iarocci streamer tubes placed between steel absorber plates. The first of the steel plates is actually the 20 cm (30cm for north) backplate of the sister MuTR magnet. The total thickness of the other steel absorbers is 60 cm. The distribution of absorber along the beam axis in terms of integrated interaction lengths is shown in 3.10.

Each instrumented gap actually consists of six separate panels as shown in Figures 3.11 and 3.12. Note that each panel overlaps its neighbors so as to minimize dead area due to panel frames. The size and arrangement of the panels is the same for all gaps. This was not an obvious design choice; the active area of the detector layer could have been smallest at the first gap and increased similarly to the MuTR , but a uniform construction was more cost effective. Each panel contains two layers of
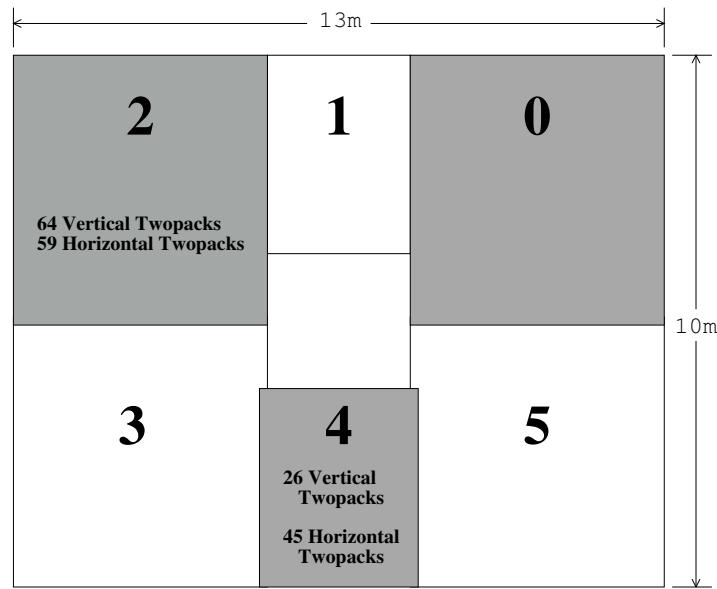
Figure 3.11: South MuID panel configuration as seen from interaction point. Shaded panels and white panels are mounted on separate rails. Panels closer to the interaction region are shaded. Notice the slight overlap of each small panel with its neighbors. Panels 0 and 2 also have slight overlap with the lower panels 3 and 5.
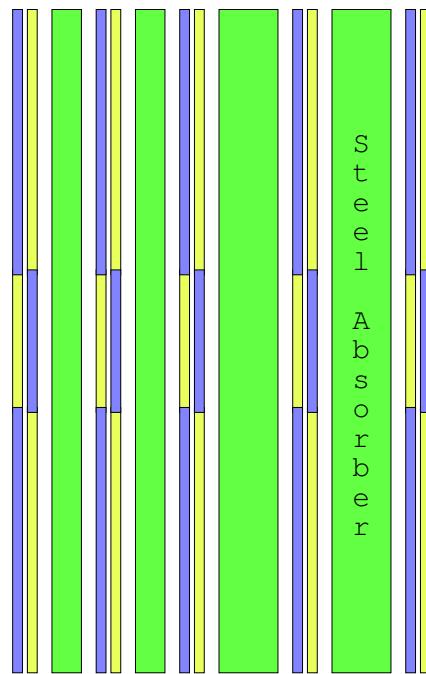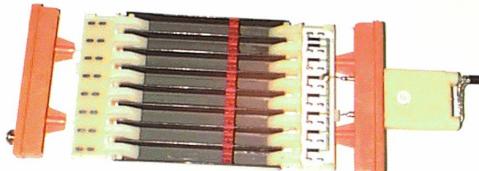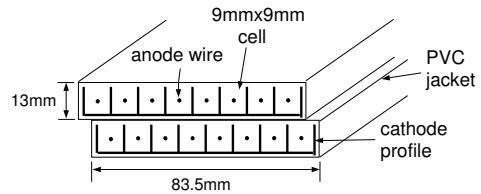
Figure 3.12: MuID Panel Configuration as seen looking down onto top. Closer panels are darker (blue) The leftmost layer corresponds to panels 0,2, and 4 in Figure 3.11. Notice the slight overlap of each panel with its neighbors in the adjacent plane. The interaction point is to the left.

(a) Iarocci tube without jacket.

(b) Twopack crossection

Figure 3.13: Streamer tube design. (a) A photograph of a short (10 cm) Iarocci tube without PVC Jacket. (b) Dimensions of the Iarocci tubes and twopack configuration. The tubes are staggered by half a cell to increase redundancy and efficiency.

vertically oriented tubes and two layers of horizontally oriented tubes encased in an aluminum housing. The plastic casing of the streamer tubes is 8.35 cm wide and divided into eight channels as shown in Figure 3.13. The centers between adjacent streamer tubes inside the panels are 8.4 cm apart. The interior of the tube casing is graphite coated to form a cathode, and a 100 μm CuBe anode wire runs the length of the tube in the center each channel. All of the wires for each tube are coupled together to form a single output. Each tube is attached with a half cell offset to another, and these tubes are OR'ed to form a twopack, the smallest element read out from the detector. This twopack configuration allows a significant increase in efficiency, compared to a single tube, due to the large overlap of active area and the minimal overlap of inactive area. Each tube is on a separate high voltage chain, so one can fail with only a drop in efficiency. There are a total of 3170 twopacks in each muon identifier arm. A non-flammable mixture of 91.5% CO_2 and 8.5% isobutane is passed through the volume of the Iarocci tubes. The gas system runs in a recirculation mode to significantly reduce the cost of operation. The isobutane content may be increased to as much as 25% at a later time which would improve gas gain, but this would require study and additional safety considerations. N_2 is flown through the secondary volume outside the tubes but inside the panel casing to carry off any leakage from the primary volume and to

maintain a dry environment for electronics housed inside the panel casing.

MuID Read Out

The signals from the twopacks are amplified, by in-panel amplifiers, to produce a 250 mV differential signal which is sent over 30 m twisted pair cables to the FEE crate. The key design consideration for the amplifiers was longevity. These components are virtually inaccessible and failures would be near impossible to repair. The amplifier circuit employs polyfuses, double-diode protection against damage from broken wires, and diode clamps to prevent damage from accidentally reversed connections. The analog signal from the twisted pair travels through transition cards at the back of the FEE rack and into a Readout Card (ROC).

The ROC shapes and digitizes the signal as either a 1 or 0, hit or no hit. Signals are delayed to synchronize signals from all incoming twopacks, and accepted events can be stored in the ROC's 5 event buffer. Up to 96 channels of data enter each ROC. The front of each ROC has a GLink transmitter for sending data to the level 1 trigger boards, which were not operational for RHIC Run II. Each ROC also has several lemo cable connections, most of which are used for diagnostics. Some of these, the pseudo trigger outputs, are the logical OR of large sections of neighboring twopacks. These outputs supply signals to the MuID level 1 blue logic trigger used for $p + p$ data. The basic data flow is shown in Figure 3.14.

Twenty ROCs are connected via a backplane in the FEE crate to one FEM. This combination instruments one orientation of the MuID twopacks, so two such crates are needed to read out one arm. Each FEM has an ARCNet interface, used for slow controls, a GLink receiver, for fast timing signals from the Granual Timing Modules, and a GLink transmitter, for sending data to the Data Collection Modules. ARCNet is used for slow controls such as setting various delays and thresholds on each ROC.
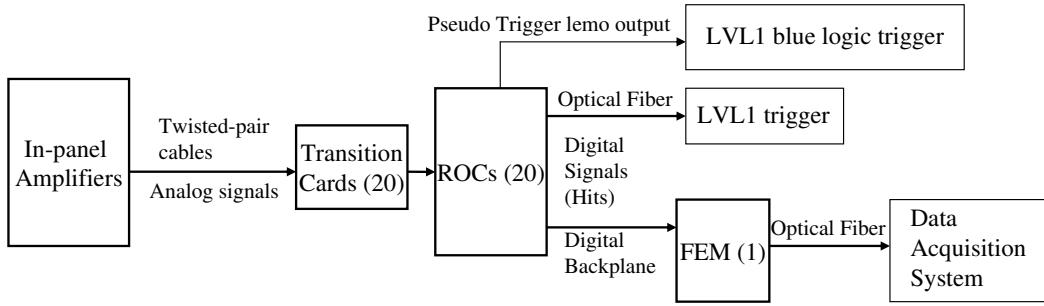
Figure 3.14: Sketch of the MuID Front End Electronics. Readout Cards process signals from as many as 96 twopacks. The digitized hits are sent to the Level 1 trigger and a Front End Module. The LVL1 MuID trigger was not available for Run II.

MuID Performance

Prior to Run II, cosmic ray data was taken with the MuID to commission the detector. This included initial timing in of the detector, checking channel mapping, study and reduction of electronic noise and an initial measure of the MuID twopack efficiencies, Figure 3.15. The details of the MuID performance and efficiency are discussed in Chapter 5.

3.4   The Global Detectors

A set of detectors are employed by PHENIX to characterize the basic nature, or global parameters, of each collision. Such parameters include vertex position, collision centrality, and the orientation of the reaction plane of the collision.

3.4.1   The Zero Degree Calorimeters

The Zero Degree Calorimeters (ZDCs) are designed for two purposes: to act as common luminosity monitors at the RHIC interaction regions and to serve as part of the experimental apparatus for the various experiments. ZDCs were implemented 18 m
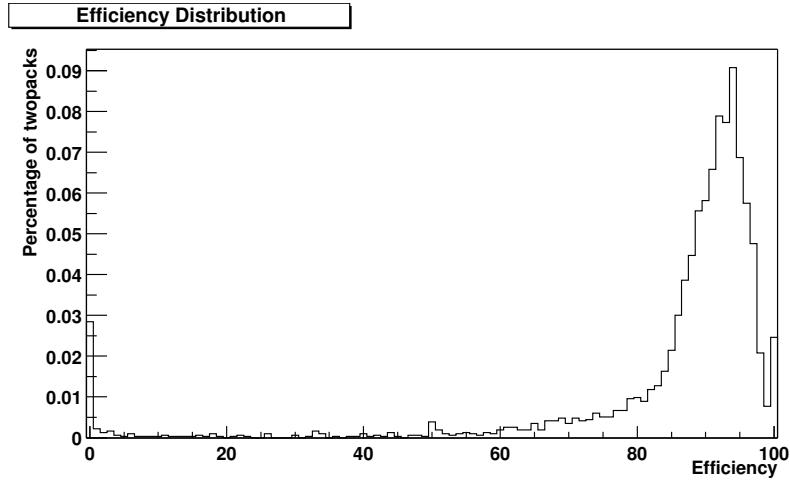
Figure 3.15: Twopack efficiency distributions measured with cosmic rays. Prior to the Run 2, the MuID was commissioned using cosmic rays [60]. The twopack efficiency distribution measured during commissioning for the nominal Run II state is shown above. The peaks at 0 and 100% are due mainly to poor statistics for twopacks located on the outside edges of the detector.

upstream and downstream of STAR, PHENIX, PHOBOS, and BRAHMS. Basically, the ZDCs function by measuring the energy carried by neutrons which did not directly participate in collisions, so called "spectator" neutrons. A RHIC DX magnet, which is located between the ZDC and the interaction point, sweeps away charged particles before they can enter the ZDC as seen in Figure 3.16. The information from the ZDC is used by PHENIX for triggering and centrality determination as discussed later in this chapter.

A ZDC is constructed of alternating layers of 5 mm thick tungsten absorbers and Cherenkov fibers. These combine to give a length along the beam axis of roughly 70 cm. The ZDC is positioned between the two beam pipes, which are separated by about 11 cm. The layers of the detector have a 45$^\text{o}$ tilt with respect to the beam axis to increase light output. The light is carried in fiber ribbons to a photomultiplier tube at the top of the ZDC. The ZDC is segmented along the beam axis into three modules, each of which
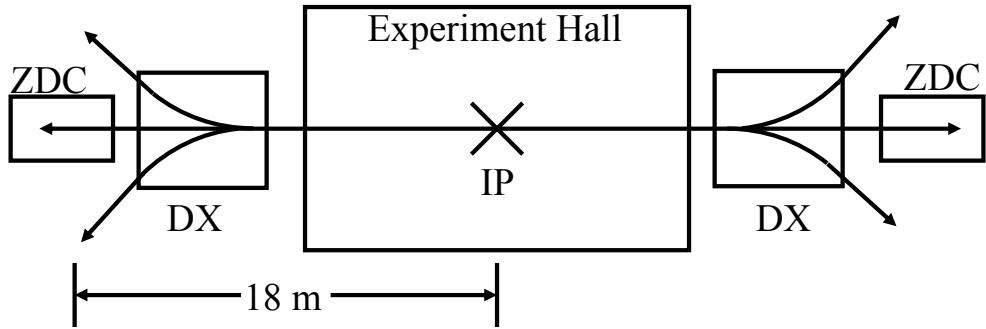
Figure 3.16: Placement of the ZDCs before and after the PHENIX experiment hall. Charged particles are swept away by the DX magnet before they can reach the ZDCs. The figure is not to scale.

contains a photomultiplier tube. A sketch of the ZDC is shown in Figure 3.17.

To insure uniformity for RHIC monitoring while providing flexibility for individual experiments, the signals have two independent readout paths. For detailed information on the performance and implementation of the ZDCs, which is beyond the scope of this work see [61] and [62].

3.4.2 The Beam Beam Counters

Another important tool in characterizing collisions at PHENIX are the Beam Beam Counters (BBCs), which measure forward charged particles. The BBCs were designed to have a dynamic range which can support Au+Au as well as $p + p$ collisions, be radiation hard, and work in high magnetic fields. The BBCs are positioned to surround the beam pipe at ±144 cm from the nominal collision vertex. Each has full azimuthal acceptance and covers 3.0 to 3.9 in η. The BBCs aid in triggering, vertex measurement, and centrality determination.

Each BBC is an assembly of 64 hexagonally shaped quartz Cherenkov radiators, each of which is attached to a photomultiplier tube as shown in Figure 3.18. For a central Au+Au collision at full RHIC energy, roughly 15 charged particles per quartz
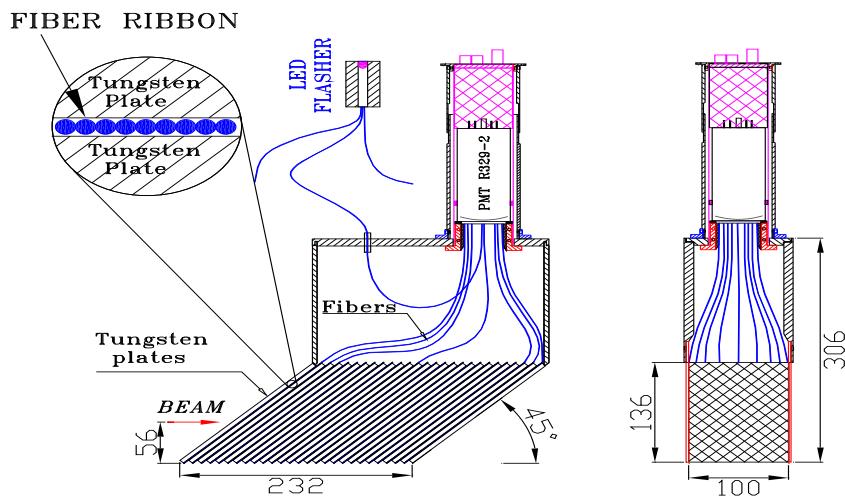
Figure 3.17: The design of a ZDC module. A ZDC is made of three combined modules.
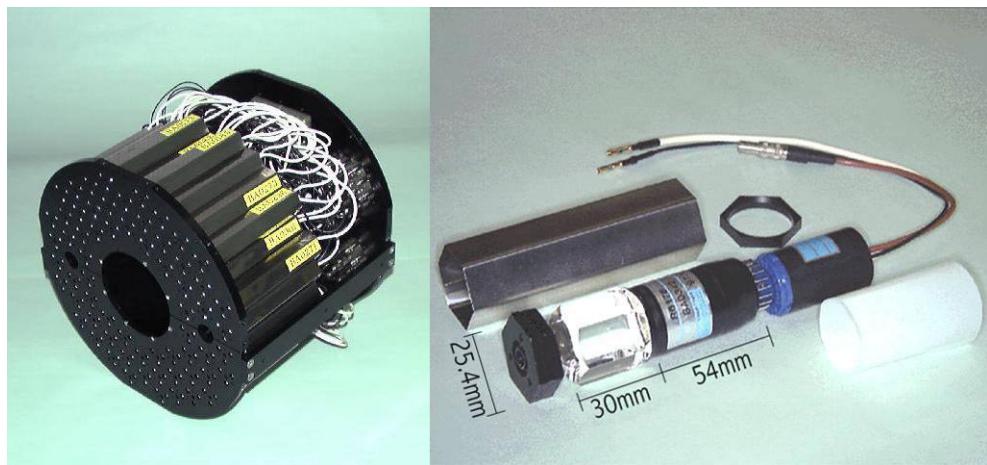
Figure 3.18: Photograph of the PHENIX Beam Beam counter. A single BBC element, quartz radiator and photomultiplier tube combination, is show right. A complete BBC, made of 64 elements is shown left.

radiator enter the BBC.

The difference in hit timing of the BBCs is used to measure the position of a collision occurring between them. Under PHENIX experimental conditions the time resolution of a single BBC element was found to be 52 ± 4 ps [63]. This translates to a spatial resolution of about 1.6 cm. The use of the BBCs in triggering is discussed later in this chapter.

3.4.3   Centrality Determination

A good measure of centrality is essential to a successful heavy ion program. Many important phenomena, such as J/ψ suppression, have critical predictions which vary with collision centrality. For PHENIX, the centrality of Au+Au collisions is determined using information combined from the BBCs and the ZDCs. While the charge in the BBC does increase monotonically with increasing centrality, information from the ZDC can be included in the centrality measurement to resolve ambiguities in less sensitive regions of the BBCs response. The correlation of the BBC and ZDC, which is used for centrality determination, is shown in Figure 3.19. Sections of the correlation are grouped to form centrality classes. Multiplicities in all detectors should be correlated with event centrality to some level. Figure 3.20 shows the good correlation for the MuID.

3.5   Triggering

The BBC was used to provide the minimum bias trigger for RHIC Run II Au+Au. The trigger required that two photomultiplier tubes in each BBC fire, and that the z-vertex, calculated from the time difference of the BBCs using a look up table, be between ±40 cm. This configuration, referred to as the Beam-Beam Local Level 1, had a trigger efficiency of 93.1 ± 0.4 ± 1.6% for events in this vertex range [64].
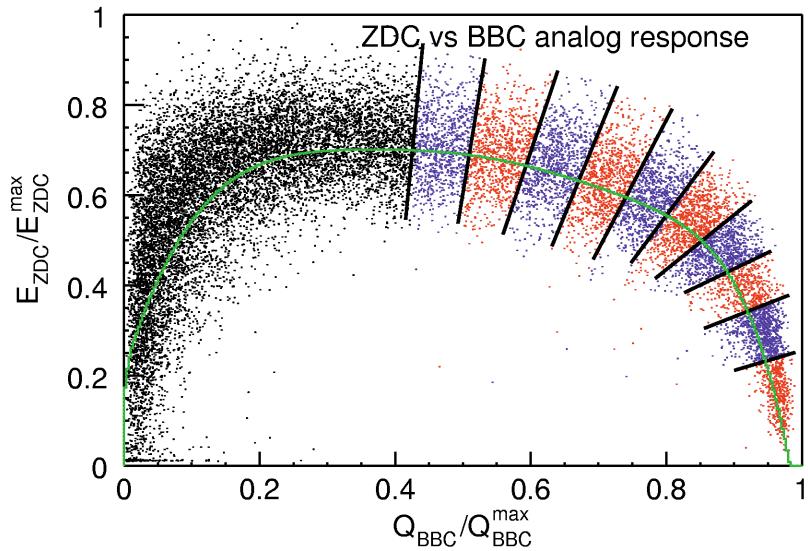
Figure 3.19: Correlation of the ZDC energy and the BBC charge sum. Lines are drawn perpendicular to the centroid of the distribution to define centrality classes. Here, bins covering 5% in centrality are shown. The most central bin is to the right.
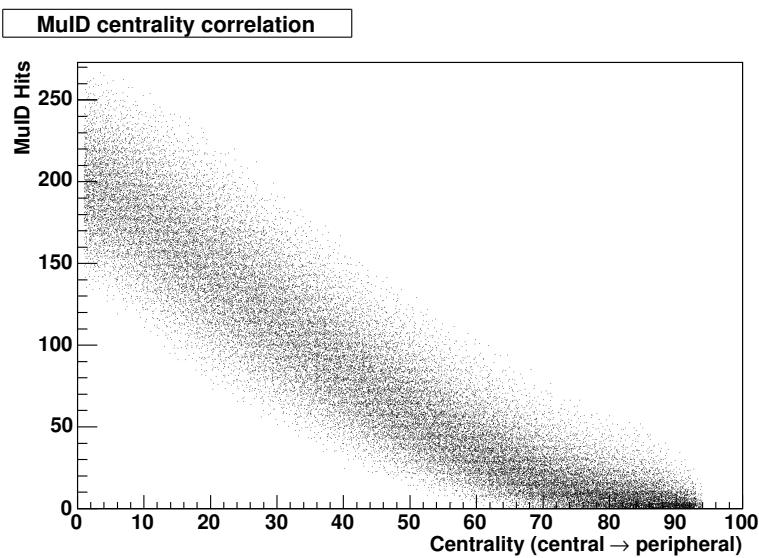
Figure 3.20: Correlation of the MuID hit multiplicity with event centrality. The MuID occupancy is well correlated with the event centrality measured by the BBC and ZDC.

The level 1 triggering system consists of two parts: the Local Level 1 which consists of hardware which communicates directly with the detector subsystems to produce reduced-bit data. The Global Level 1 uses these bits to provide a trigger decision for each beam crossing. The MuID was designed to serve as a level 1 triggering system, and MuID Local Level 1 trigger boards should be in place for Run V.

Although extensive work was done to develop and implement Level 2 triggering capabilities, these were not extensively used until after the background issues, discussed in the following chapter, prevented efficient operation of the MuID. Detailed information about the muon Level 2 triggering can be found in Reference [6].

3.6 The Data Acquisition System

As described above for the MuTR and MuID, the FEM is the link between a detector, or detector section, and the PHENIX Data Acquisition system (DAQ). This is generally true for each subsystem. A sketch of the DAQ, as described below, can be seen in Figure 3.21. Each beam crossing, every 106 ns, the detectors are sampled, but data cannot be digitized at such a high rate. Data from a few fast detectors is sent out to subsystem specific Local Level 1 (LLVL1) trigger hardware, which send a small number of bits which characterize the data to the Global Level 1 (GL1). GL1 then makes a trigger decision based on the assembled bits from the various LLVL1 subsystems. On the occasion that a beam crossing satisfies the trigger criteria, GL1 sends a request for the event, which has been buffered by subsystem FEEs, to each subsystem. The request is actually sent via the various Granual Timing Modules (GTMs), which send clock and trigger data over optical fiber to subsystem FEMs. In response to this request, the FEMs digitize and transmit the event data, also over optical fiber, to the PHENIX Data Collection Modules (DCMs). The data from the FEMs is sent in a packet format, which has a header containing essential identification information and a trailer containing di-
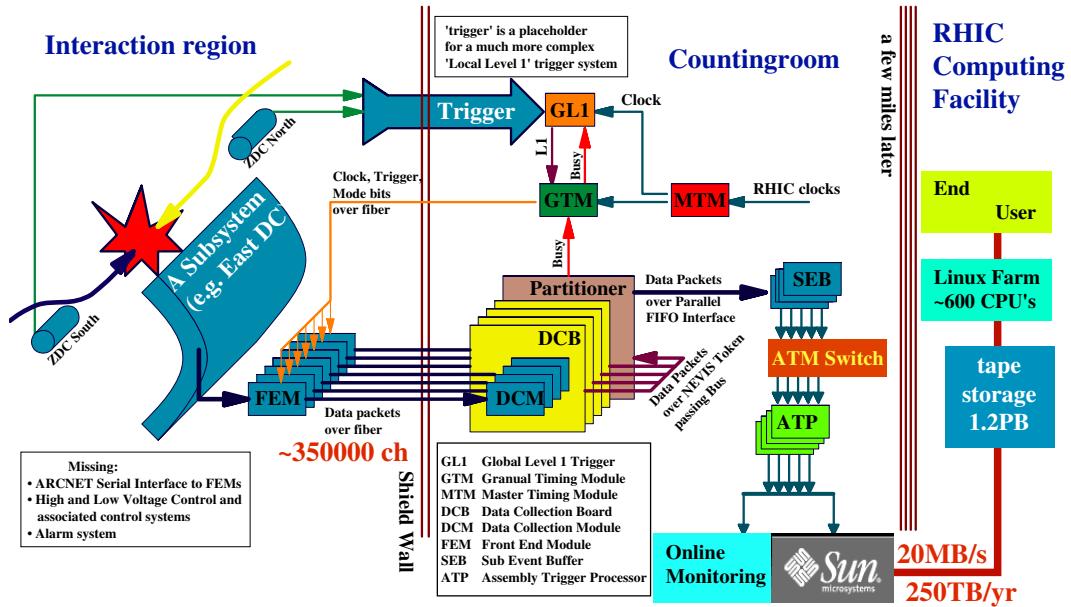
Figure 3.21: A diagram of the PHENIX Data Acquisition System. See text for description.

agnostic information. The DCMs zero-suppress the data using subsystem dependent algorithms. Basic error checking is performed, and calibrations can also be carried out. Data is sent to the Event Builder, which is made of Sub Event Buffers (SEBs) and Assembly Trigger Processors (ATPs). The ATPs and SEBs are specially equipped PCs running Windows NT. Data is buffered on the SEBs until requested by the ATPs. The ATPs assemble data from the SEBs into complete events. At this stage, level two trigger algorithms can operate on the data. Accepted events are then sent to "buffer boxes", computers with a large amount of disk storage. When a buffer box is not being written to, the data files can be sent over high speed fiber to the High Performance Storage System (HPSS) tape archive at the RHIC Computing Facility (RCF).

71

Chapter 4

Event Quality and Selection

RHIC and PHENIX have exhibited an impressive track record through their first four running periods. Significant amounts of data have been taken for polarized $p + p$ ($\sqrt{s_{NN}} = 200$ GeV), d+Au ($\sqrt{s_{NN}} = 200$ GeV), and Au+Au ($\sqrt{s_{NN}} = 200, 130, 62.4$, and 19 GeV) collisions, and by the end of Run IV, RHIC was regularly providing Au+Au collisions at twice design luminosity. The data from the Runs I-III have resulted in 27 PHENIX physics publications to date, 5 of which are preprints, with many more in preparation. PHENIX recorded 96 million $\sqrt{s_{NN}} = 200$ GeV Au+Au minimum bias collisions in Run II and an impressive 1.5 billion more in Run IV resulting in over 200 TB of raw data. Unfortunately many of these events for Run II were not suitable for muon analyses. Only the south muon spectrometer was available for Run II. The north spectrometer was operational for Run III, and both spectrometers took useful data during their respective commissioning runs.

4.1   RHIC Background Issues

As the RHIC Run II running period, which began in August 2001, was the commissioning run for the south muon spectrometer, some unanticipated challenges were ex-
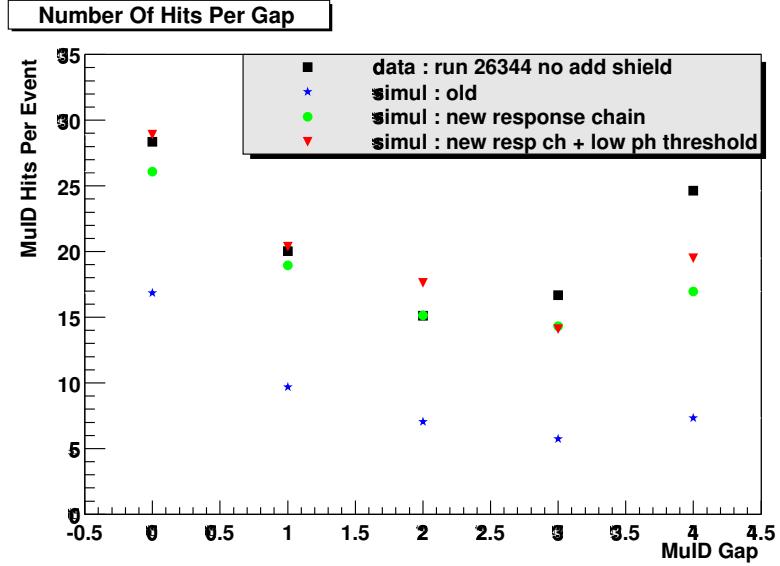
Figure 4.1: Simulated hits per gap per event for the MuID before shielding. Statistical errors are smaller than symbol size.

pected. Some of the more significant challenges came in the form of accelerator related backgrounds. Soon after collecting the first commissioning data, it was realized that the MuID occupancy was roughly twice the expected value from HIJING simulations. Also, the occupancy as a function of depth from the nominal vertex position had a significantly different shape than that from simulation. The simulation predicted a general drop in occupancy with increasing depth, while the data indicated a drop in occupancy near the middle and a rise at the back as seen in Figure 4.1.

The first step in resolving this challenge was to understand the large discrepancy between data and simulation. After investigation, it was discovered that most of the discrepancy was due to missing material in the simulation and an insensitivity to particles entering the detector from angles significantly different from those of particles produced near the nominal vertex. Improving the simulation's sensitivity to particles entering the MuID from any direction indicated that the background was mainly coming from particles emanating almost perpendicular to the beam pipe, as sketched in

73
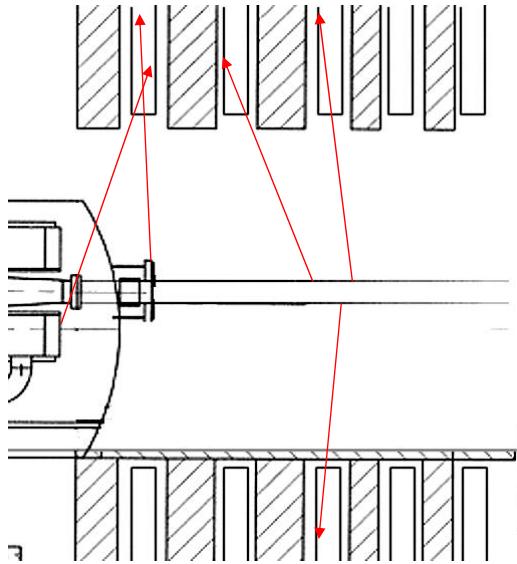
Figure 4.2: Sketch of sources of MuID square hole background.

Figure 4.2. These particles were produced by very forward collision products which entered the beam pipe material at a very small angle, thus traversing a long section of the beam pipe material. Decreasing the photon threshold for the inner part of the MuID absorber layers from 50 MeV to 5 MeV produced roughly a 10% effect in increasing the occupancy.

Once a good understanding of the background had been established, the project shifted toward finding a quick and effective solution. After simulation and *in situ* tests of various shielding options, six inches of steel covering the floor and side walls of the MuID square hole, which surrounds the beam pipe, was selected as the shielding solution. Time constraints made it impossible to adequately shield the area directly above the beam pipe, which left the upper small panels and sections of the upper large panels of the MuID unshielded. Also, the shielding could not be extended out of the square hole in order to shield the gap 0 panels, which are those closest to the interaction point. Seven tons of small steel plates were hand stacked during a two day shutdown. The positive effect of the shielding and good agreement of post-shielding with simu-
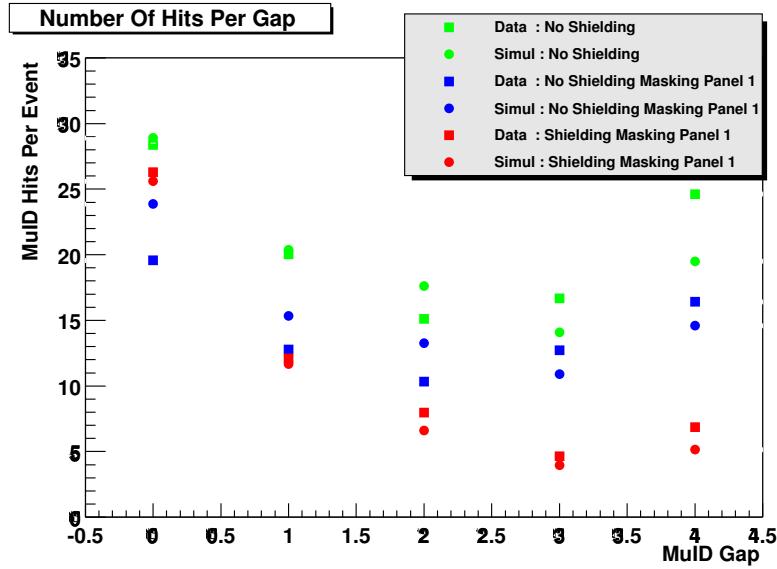
Figure 4.3: Measured and simulated hits per gap per event for the MuID after before and after shielding. Measurements and simulations show the reduced occupancy and improved detector response. Statistical errors are smaller than symbol size.

lation can be seen in Figure 4.3. A more permanent solution, which included ceiling shielding, was implemented for both muon identifier arms for RHIC Run III (Figure 4.4). The shielding for each square hole consists of a 6 inch thick steel floor plate and a three-sided 6 inch thick steel box, comprising the walls and ceiling, which is inserted into the hole from the tunnel side.

In the later part of the run, RHIC was able to significantly increase the luminosity. This had the unfortunate impact of producing a new background problem for the MuID. The backgrounds raised the currents in the Iarocci tubes to levels which caused voltages, hence efficiencies, to drop significantly. Operating with these current levels would also significantly shorten the lifespan of the streamer tubes. The backgrounds were particularly harsh for gap 4, which is tunnel side, and particularly the upper panels. Most of the lower panels are below the level of the concrete tunnel floor. The high currents persisted in the MuID when RHIC separated the beams so that no beam-beam
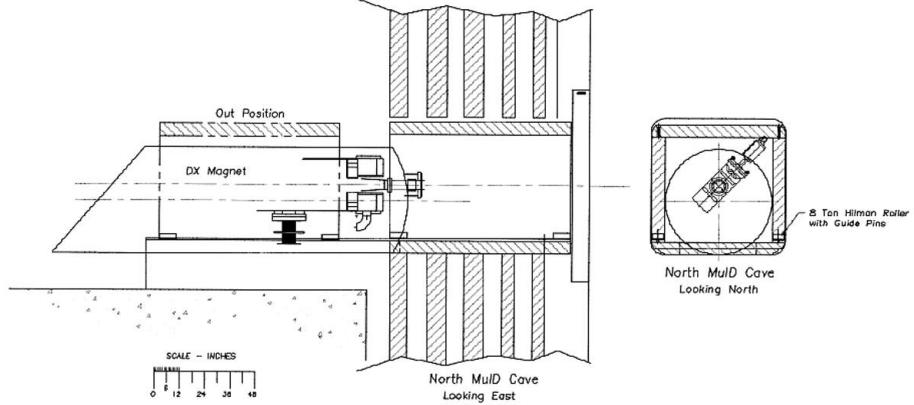
Figure 4.4: RHIC Run III MuID square hole shielding design. The shielding consists of a steel floor plate and a three-sided box which is insterted into the hole from the tunnel side.

collisions occurred; thus proving that the background was not collisions related. This isolated the problem to beam scrape, beam ions inadvertently interacting with RHIC infrastructure, or beam gas, beam ions interacting with free particles in the beam pipe.

Studies continued through Run III on diagnosing and addressing this background. Scintillator paddles were placed on the tunnel side of the north MuID, since the *Au* beam entered from the North at PHENIX. The paddles were used in coincidence with the MuID blue logic 1 deep trigger as a background trigger, and the data was reconstructed in an attempt to image any background source. As shown in Figure 4.5, the reconstructed roads exhibited a wide distribution, consistent with a diffuse source, projecting to the beam axis for many tens of meters into the tunnel. The RHIC accelerator facility was able to reduce the problem with additional beam steering and aggressive beam collimation, but installation of significant amounts of shielding on the tunnel side of each MuID was also required to reduce the background to an acceptable level. A steel wall over 4 feet thick was constructed behind each MuID. Other 40 inch thick blocks were placed downstream at strategic locations. Figure 4.6 shows this arrange-

76
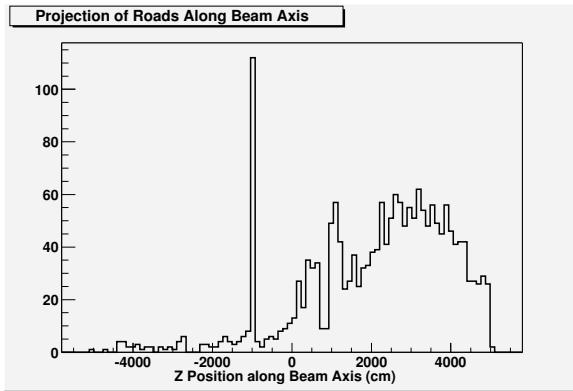
Figure 4.5: The projection of north MuID background roads, triggered by tunnel scintillators and MuID BLT coincidence, onto the beam axis. The peak at -999 cm corresponds to roads parallel to the beam axis.
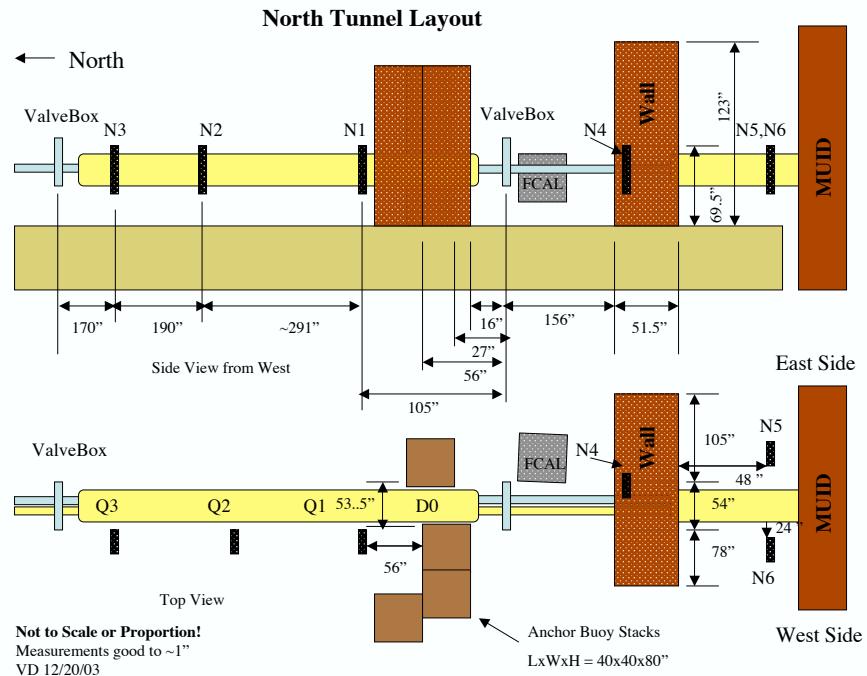
Figure 4.6: Diagram of the north MuID tunnel shielding added prior to Run IV. The tunnel scintillators are also shown (N1-N6).

ment for the North side. Also, scintillator paddles, labeled N1-N6 in Figure 4.6, were placed at various locations in the tunnel to monitor background rates. These provided important feedback information for RHIC when steering the beams. MuID high voltage snapshots for Run III and Run IV shown in Figures 4.7 and 4.8 demonstrate the very significant effectiveness of the background treatment.

To summarize, Run II Au+Au data taking can be divided into three parts as seen in Figure 4.9. These sections are the early section of the run, during which the MuID suffered from collision related background, the late section of the run, during which the MuID suffered beam scrape, or tunnel, related background, and the central section of the run. All Run II data used in this analysis is taken from the central section of the run. Background rates did vary from store to store during Run IV, but no long sections of the run suffered significantly worse backgrounds.

4.2   Hardware Status

During Run II much of the MuTR high voltage system had stability issues due to humidity levels in the experiment hall. Logs from the high voltage system were used to remove runs in which a MuTR high voltage channel tripped or more than 18.5 % of the channels were disabled, see Figure 4.10. Only 87 of the 203 physics runs during the low background section of Run II meet this criteria. Minor modifications to the HV system and circulation of dry air through the MuTR eliminated this issue, greatly increasing the efficiency and stability for following runs. Hit distributions demonstrating the overall improvement of the MuTR, which included some FEE repairs, are shown in Figure 4.11.

The MuID high voltage system also faced some stability hurdles during Run II. To ensure detector safety, the MuID high voltage must be lowered or turned off during beam injection and tuning. Also, the MuID automatically recovered from channel
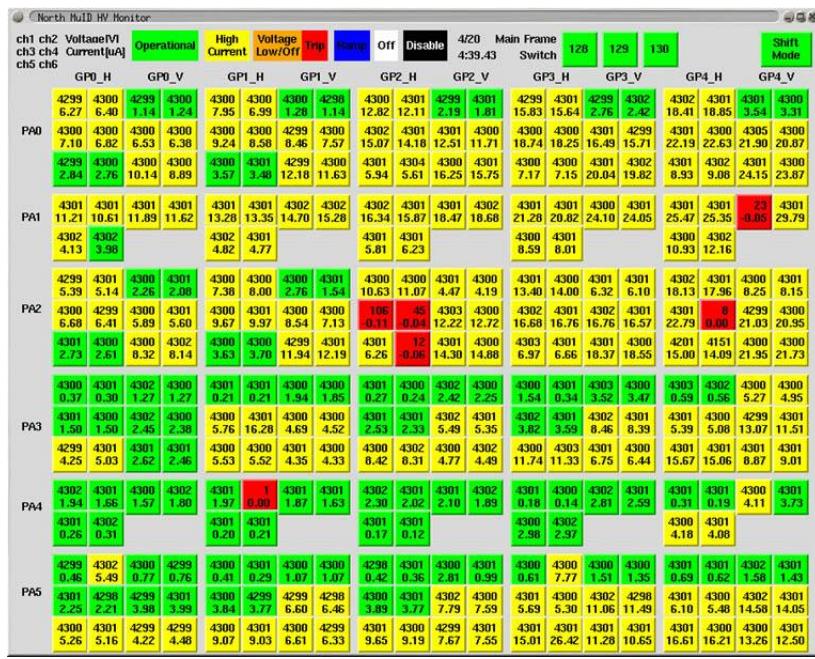
Figure 4.7: North MuID high voltage display during bad beam conditions for Run III. Light gray (yellow) indicates high current. Channels on the left are near the PHENIX experiment hall, while channels on the right are near the RHIC tunnel. The top half of the channels are in upper panels.

Figure 4.8: Typical post-shielding MuID high voltage display during Run IV. Light gray (yellow) indicates high current. Channels on the left are near the PHENIX experiment hall, while channels on the right are near the RHIC tunnel. The top half of the channels are in upper panels.
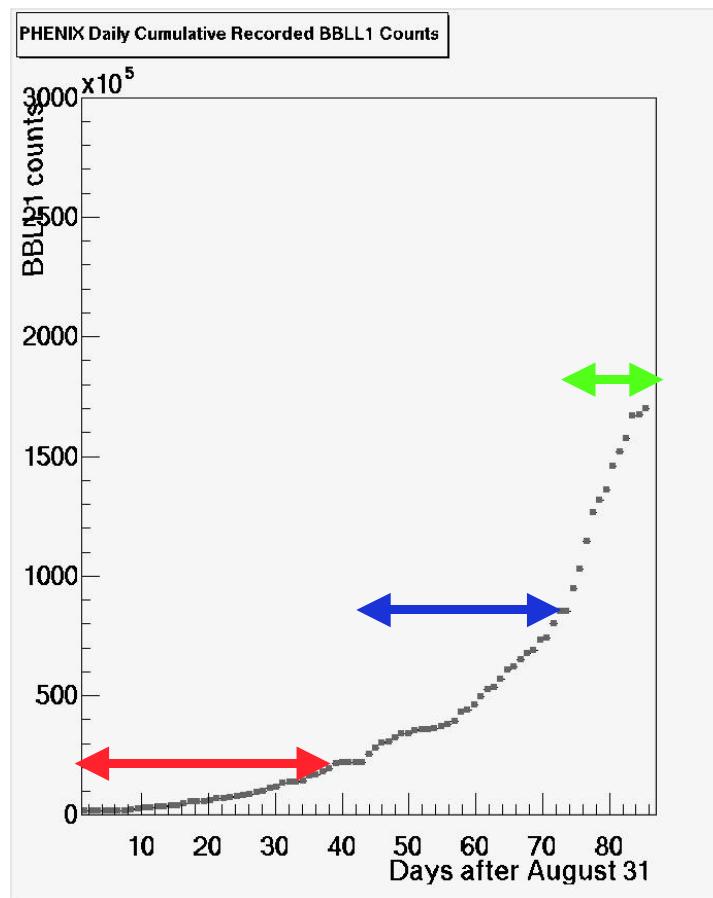
Figure 4.9: PHENIX Run II Au+Au integrated luminosity as a function of time. The middle (blue) arrows indicate the low background section of the run. The left (red) and right (green) arrows indicate the sections of the run dominated by square hole and tunnel side backgrounds respectively.
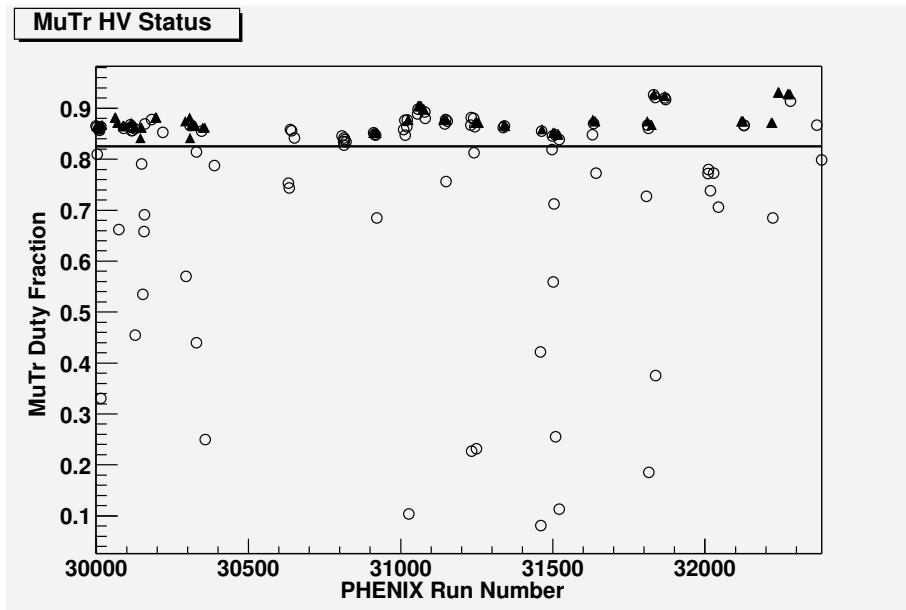
Figure 4.10: Fraction of functional high voltage for the Muon Tracker as a function of run. The line indicates the acceptable threshold of 81.5% enabled. The open circles represent runs which are below this threshold or had a HV channel trip.
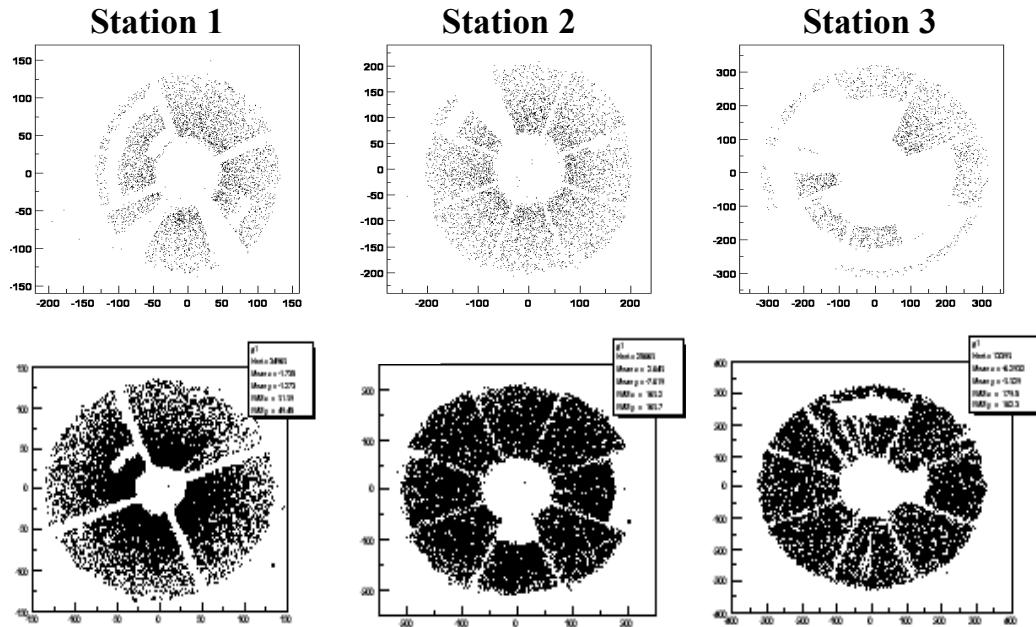
Figure 4.11: Typical MuTR hit distributions for Run II (top) and Run III (bottom). Reduced humidity susceptibility and FEE repairs greatly improved the MuTR performance after Run II [65]. Azimuthal holes represent HV problems, and radial holes correspond to FEE problems.

trips during Run II, which occurred fairly frequently. Since the MuID high voltage system consists of 300 channels per arm, this control entails a large amount of communications, compared to other subsystems. This amount of communications revealed stability issues with the Input Output Controllers (IOCs) used to communicate with the LeCroy HV mainframes. The IOCs crashed frequently leaving the shift crew without control of the system for several minutes while the IOC was rebooted. Efforts were made to minimize the communication during Run II, and the IOCs were removed from the system for Run III. The mainframes are now controlled by server software on a PC which is directly connected to the HV mainframes via a serial cable.

During commissioning of the north MuID HV system, it became obvious that the individual north chains were operating much more stably than those in the south. Far less tripping and sparking was observed. This led to a reinvestigation of the south arm HV system. It was found that previously observed sparking in the south arm was in fact due to insulation breakdown caused by the potting compound used in the connector ends which attach to the detector panels. A different potting compound had been used for the north arm due to earlier indications that the potting compound used in the south arm may cause insulation breakdown, and, thus, it had not suffered any breakdown. This led to replacement and repotting of the connector ends for much of the south MuID.

Another notable Run II issue was the discovery of HV modules which supplied voltages lower than their requested/reported values. The problem was traced back to faulty read back resistors in the sensing circuitry of some HV modules. This resulted in repairs, replacements and extensive re-testing of the modules before Run III.

4.3 Trigger Selection

For Au+Au collisions, the beam-beam counters provide the minimum bias trigger. The beam-beam local level 1 trigger uses the timing measurements from the BBC's the estimate the z vertex position. The BBCLL1 z vertex was required to be within ±30cm for Run II and ±20cm for Run IV. For Run II minimum-bias triggers are estimated to sample 92% of the 6.9 barn Au+Au inelastic cross section [64]. All minimum-bias events which passed the selections for background, HV, triggering were reconstructed, and 7.6 million events, corresponding to an integrated luminosity of 1.1 μb^{-1} , were found to have a collision z-vertex with ±40cm.

Although a large sample of MuID level II triggers were recorded, these are not used for this analysis due to the beam related backgrounds. An unfortunate mismapping in the level II algorithm rendered the trigger highly inefficient, so its usefulness would have been limited even in a clean environment. Only minimum bias events are used in this analysis.

Chapter 5

Data Reduction

5.1 The PHENIX Data Flow

Data is collected by the PHENIX detectors and passed thought the Data Acquisition System as Described in chapter 3. Once this stage is completed, the data, in the form of PHENIX Raw Data Format files (PRDFs), reside on magnetic tape in the RHIC Computing Facility (RCF) High Performance Storage System. The data can then be retrieved for offline reconstruction. Official reconstruction is generally performed on a cluster of personal computers at the RCF running a Linux operating system, but data can be transferred to other computing facilities. These other facilities are particularly useful for making multiple passes over a significant subset of data in order to improve software performance.

Once retrieved from HPSS, the PRDFs are then processed by the PHENIX offline reconstruction software. The software is written primarily in C++, with some legacy code in C and FORTRAN, and makes significant use of the ROOT analysis package. The software source code is currently available to the public at http://www.phenix.bnl.gov/viewcvs/. The reconstruction software takes raw detector information and reconstructs particle paths and relevant physics quantities. These are

then saved to disk in the form of a Data Summary Tape (DST), although this might be viewed as a slight mis-naming since a DST is roughly the same size as a PRDF and still contains some raw detector information. Also, the muon reconstruction can begin with a DST as initial input starting at the MuTR cluster finding. An overview of the data flow is shown in Figure 5.1.

Generally a final physics analysis is done on a more refined version of the DST which has additional cuts and corrections applied. Also, while DSTs contain information about all detectors, the nDSTs (nano-DSTs) and pDSTs(pico-DSTS) are broken into sub-types which are tailored for specific physics analyses, although it is possible to process different sub-types of nDSTs simultaneously. The nDSTs do not store any low level detector information, such as MuID hits, but still have a event-by-event structure similar to the DST. The pDSTs are very tailored to a specific analysis such as a single muon or di-muon analysis. These are basically ntuples of reconstructed particle properties.

5.2   Muon Reconstruction

The reconstruction of muons begins in the MuID. Many of the same characteristics which make the MuID a good level 1 trigger system make it good for starting the reconstruction. One dimensional roads are formed through iterative projections from a seed gap, a gap where reconstruction begins. The one dimensional roads are then merged to form two dimensional roads. These are then filtered down to a smaller set of roads which are projected to the closest MuTr tracking station, Station III. Clusters of strips within a projection window are grouped to form a track stub though the station layers. The process of projection and stub formation is then repeated for Station II and Station I. The algorithm is summarized in Figure 5.2 and the control parameters are shown in Table 5.1. The MuID is examined again to further refine the roads using

87

Event PRDF:
Raw Detector Signals

Data Divided by
Physics Topic

PRECO
Data Reconstruction

Muon nDST

MWG
analysis code

Event DST:
All Detectors. Roads, Tracks
Hits, Calibrated Cathodes

Muon pDST:
Divided on particle
instead of event bases
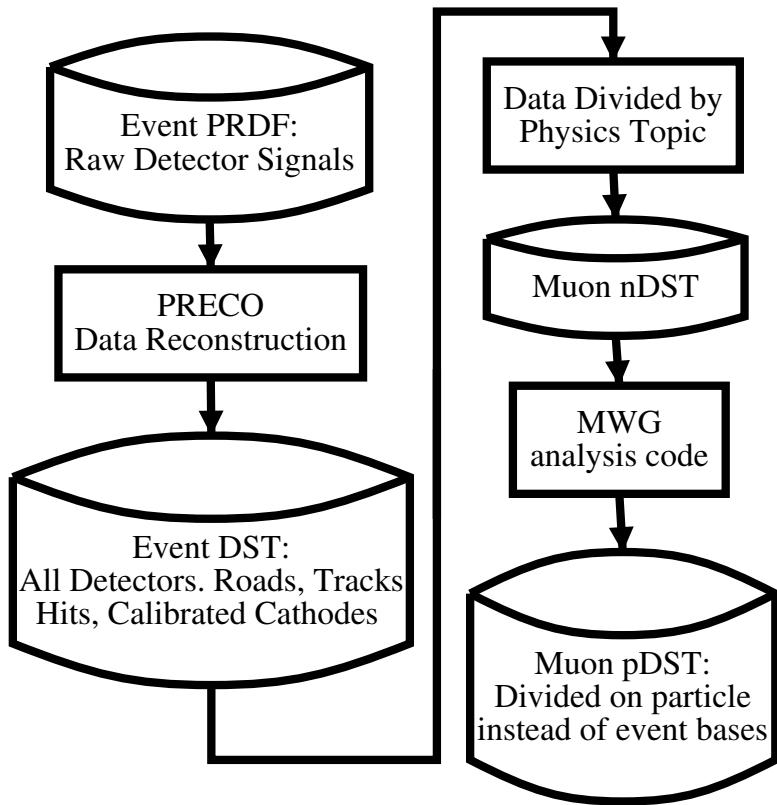
Figure 5.1: Overview of offline data flow. After full reconstruction, DSTS can be further refined and filtered into more compact analysis-specific formats.
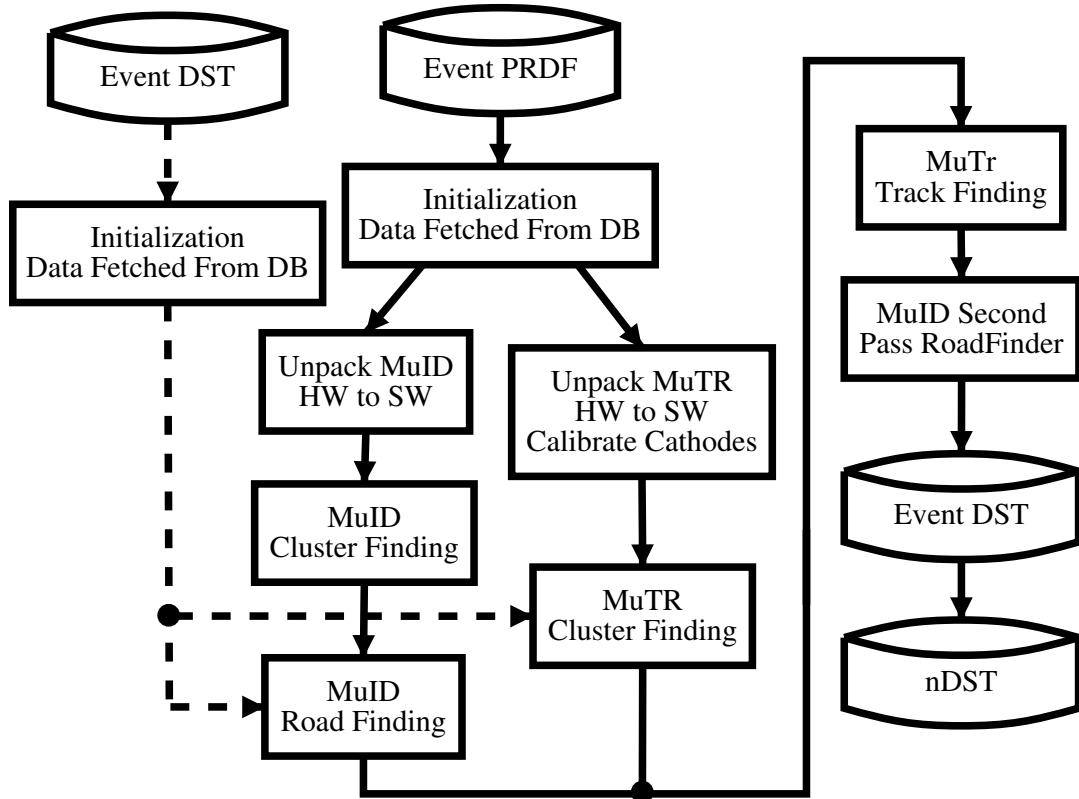
Figure 5.2: Overview of muon data reconstruction. The dashed line indicates the optional start of re-reconstruction on a DST.

Table 5.1: First Pass Road Finder Control Parameters.

Parameter	Value	Description
SeedLoop[0]	{-1,1,0,2,3,4}	Order that gaps of MuID are searched, -1 indicates the vertex position
SeedLoop[1]	{-1,2,1,0,3,4}	Order that gaps of MuID are searched, -1 indicates the vertex position
ClusterCollectMode	0	1: RoadFinder use multi-hit clusters. 2: each hit is treated as a cluster
minLastGap1D	2	Minimum Depth of a 1D road
minFiredGaps	2	Minimum number of gaps with hits for a 1D road
maxSkippedGaps	2	Maximum number of gaps missing in the planes preceeding the last gap
minSharedHits1D	5	Number of hits required for roads to be considered ghosts for the same orientation.
maxXRef1D	180	Maximum distance of a 1D roads projection to the nominal reference plane z=0 in cm.
maxYRef1D	180	Maximum distance of a 1D roads projection to the nominal reference plane z=0 in cm.
minLastGap2D	2	Minimum Depth of a 2D road
maxDelLastGap2D	1	Maximim difference of the last gap of paired 1D roads
maxDelHitsPerGap	1	Maximum difference of hits per plane for paired 1D roads
maxDelTotalHits	2	Maximum difference of hits for all planes for paired 1D roads
maxXRef2D	180	Maximum distance of a 1D roads projection to the nominal reference plane z=0 in cm.
maxYRef2D	180	Maximum distance of a 1D roads projection to the nominal reference plane z=0 in cm.
maxXChisq	1000	Maximum reduced χ^2 of vertical road fit
maxYChisq	1000	Maximum reduced χ^2 of horizontal road fit
minSharedHits2D	8	Number of hits required for roads to be considered ghosts.

the track information. The different steps of the reconstruction are discussed in detail below.

5.2.1 First Pass Roadfinder

As discussed in Chapter 3, the MuID is made of layers of perpendicular Iarocci tubes situated in five gaps between steel absorber layers. One dimensional roads are first formed from using only tubes from one orientation. Roads begin to be formed by one of two methods. In the first method, the nominal vertex position is combined with hits in the seed gap to project to the next plane in the search order. Then each hit in a search window of 15 cm, roughly two tube widths, is combined to form separate road stubs. In the second method all hits in the seed gap are combined with all hits in the next plane in the search order. The first method is generally used for reconstructing data from collisions, while the second is useful for reconstructing cosmic ray or non-collision background. This seeding is repeated using another search order with a different seed gap once roads are formed from the first search order as described below. This helps recover roads which were not found in the first search order due to hardware inefficiencies.

Once a road stub is formed, it is projected to the next search gap and each hit within the search window is combined with the stub hits to form a separate road. Even though it is possible with a 6% probability for a single particle to fire adjacent twopacks due to their slight overlap, these hits are not merged into a single cluster. Hits are first looked for in the same panel as the previous hits. If none are found, adjacent panel are searched. Each of the hits in the search window found in the adjacent panels are combined with the road to form extended roads. The road with no hit in this gap is also kept. The projecting, searching and hit attaching are then repeated for each gap in the search order. A specific example of the processes is shown in Figure 5.3.

Once the 1D roads are found for each orientation, duplicate and unlikely roads are
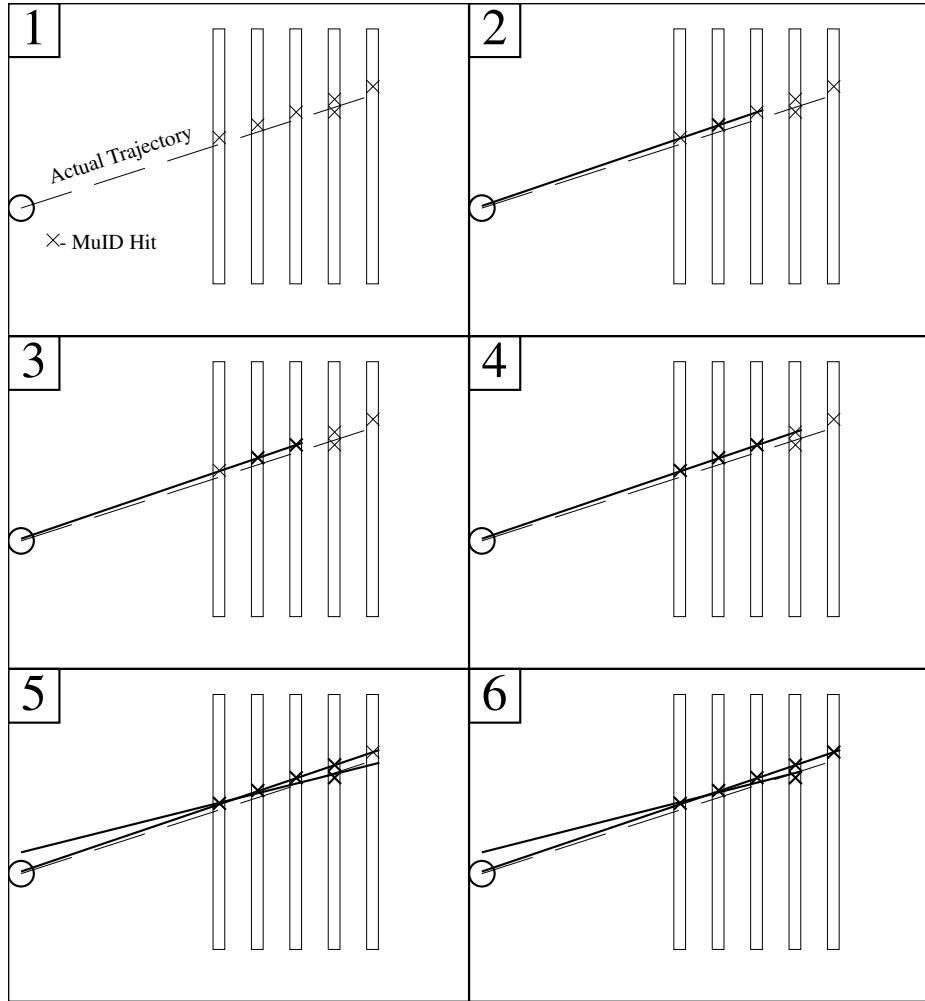
Figure 5.3: One dimensional roadfinding example. Panel 1 shows the recorded hits and the true muon trajectory. In Panel 2 a hit in the seed gap, the second gap, is found and the road stub is projected to the third gap. Panel 3, a hit from the third gap is added to the road, indicated by the darkened x, and the road is projected to the first gap. Panel 4, a hit from the first gap is added to the road and the road is projected to the fourth gap. Panel 5, two hits are found within the search window, and each is used with the previous hits to form a unique road. Each of the to roads is projected to the last gap. Panel 6, a hit is found in the window for one road's projection, so one road is assigned a last gap of 3, counting from 0, while the other penetrated the entire detector and has a last gap of 4.

removed. A road must meet the following criteria in order to be kept. The road must have at least one hit beyond the second gap. The road must have hits in at least two gaps. The road can have at most 1 skipped gap. Since each of the two search orders could have resulted in reconstructed roads containing all identical hits, these duplicate roads are removed.

The roads from separate orientations are then combined into two dimensional roads. Various attributes of the roads from opposite orientations are compared to significantly reduce the number of falsely combined roads: 1) The depth of the roads can differ by no more than one gap. 2) The roads must contain nearly the same number of hits. 3) Roads which transition from one panel to another should only be paired with roads of the opposite orientation which make the same panel transition.

Even with perfect pairing of the 1 dimensional roads, it is sometimes impossible to avoid unphysical ghost roads. If two particles which fire different twopacks are tracked though the same panel of the MuID, the detector design produces two ghost roads due to stereoscopic ambiguity as shown in Figure 5.4. More generally, N real crossings in a panel produce $N^2 - N$ false crossings. Although information form the MuTR can eventually reduce the number of ghost though techniques such as a matching angle cut between MuID roads and MuTR tracks, It is generally impossible to tell which are the real roads from the MuID alone.

It is important to pass as few roads as necessary to the MuTR in order to reduce the significant computing resources needed by the reconstruction. Similar roads are likely to produce similar tracks, so only one representative road for a grouping of similar roads is used for seeding the MuTR reconstruction. The first road becomes the first group. Subsequent roads are compared with all groups. A road is added to a group if 1) it has hits within a fixed window of the hits of any road in the group in both orientations and 2) The road's projection to MuTR Station lies within a window of the projection of any road in the group. It the road satisfies these conditions for two groups, the groups are
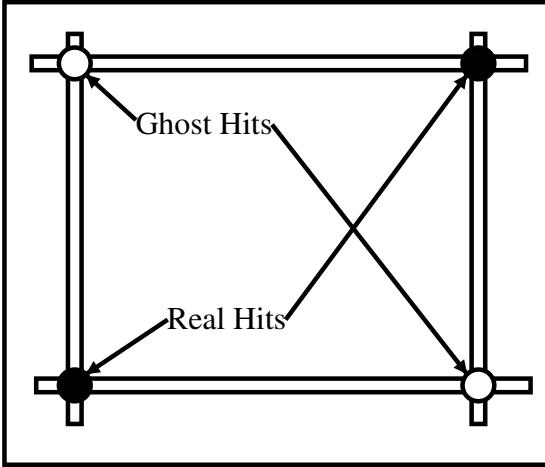
Figure 5.4: The design of the MuID makes it susceptible to stereoscopic ambiguities. This demonstrates the simple case of two roads passing though the same MuID panel. The fired twopacks are outlined, and one can see that discriminating between the true hits and the ghost hits is impossible, if no other information is available.

merged. If the road does not meet these conditions for any group, the road starts a new group. Only one road from each group is passed on to the MuTR reconstruction. The road which has the Station III projection closest to the median of all Station III road projections is used to represent the group.

5.2.2 Track Reconstruction for the Muon Tracker

The fist step of the MuTR reconstruction is to collect adjacent cathode strips which had an induced charge into clusters. As discussed in Chapter 3, a charged particle passing though a MuTR chamber induces a charge on several cathode strips. The distribution of charge can be fit with a single Mathiason function as shown in Figure 3.8. It is possible for different particles to induce charge on some of the same strips, and this is fairly common in high multiplicity Au+Au events. These, usually wider, cluster distributions can be fit with a sum of two Mathiason functions if the overlap is not too large. Fitting a charge distribution with a Mathiason function can provide a position resolution as good

Table 5.2: MuTR search window values at each station.

Mutr Station	Polar (cm)	Azimuth (cm)
I	20	10
II	30	25
III	50	40

as 100 μm, but boise and gain fluctuations can degrade this.

As mentioned in the previous section, roads from the MuID are used to seed the reconstruction in the MuTR. Clusters which fall within a search window of the projected road-station intersection are grouped into a track stub. Station III has 2 layers of anode wires and 4 corresponding cathode planes, so an ideal Station III stub will be made of from 4 clusters, one from each cathode plane. This stub provides a momentum measurement which then allows projection through the magnetic field back to Station II. If one layer of Station III is disabled, a 2 cluster stub can be used with the MuID road depth providing a rough momentum estimate. Clusters are again grouped within a window of the projection. Due to the higher resolution of the MuTR the search window is shrunk as projections are made thought the MuTR. The window dimensions are listed in Table 5.2. A stub is formed at Station II which would ideally have 6 clusters; one for each cathode plane. The projection and cluster collecting is repeated for Station I.

The last fitting point is the BBC measured vertex. Since a large amount of absorber is present between the MuTR and the vertex, estimates for energy loss and multiple scattering must be used to recover the particle's initial momentum and trajectory.

5.2.3 Second Pass Roadfinder

Once MuTR tracks are reconstructed, the second pass road finder utilizes the MuTR information to produce the final set of refined MuID roads. Since MuID roads seed the MuTR track finding, different MuID road can be associated with identical MuTR

tracks. Although this is highly unlikely due to the road grouping at the last stage of the first pass roadfinder, only the best road is kept for these cases. Since the first pass roadfinder is optimized for accurate pointing to the MuTR, the algorithm favors adding only true hits to a road at the cost of missing some true hits over associating all true hits at the cost of adding false hits. The second pass road finder attempts to attach any missed hits. Each road is projected through the entire MuID and hits which fall within the search window for each gap are added to the road. These roads are refit, and they become the final version of the MuID roads.

5.3   Software Performance

The performance of the reconstruction software can be examined using detailed simulations. PHENIX has developed a GEANT [66] based package referred to as the PHENIX Integrated Simulation Application (PISA). PISA can use input from various external event generators such as PYTHIA and HIJING as well as many internal single particle generators. PISA uses this input to generate a hits file, which records interactions with active detector material. This hits file is then passed though response software which mimics detector digitization including hardware efficiencies to produce a simulated PRDF. This can then be analyzed by the same reconstruction software used for real data to produce a simulated DST. These steps can also be combined to avoid writing a simulated PRDF. Figure 5.5 shows the simulated reconstruction efficiency for 5 GeV/c single muons. A muon is considered found if the reconstructed road contains at least half of the hits created by the simulated particle.

The correlation between hit occupancy and number of found roads from the first pass roadfinder is shown in Figure 5.6. There is a slow turn on in the road occupancy until about an average of 70 hits. The number of roads then quickly increases until the grouping algorithm begins to make a significant impact. Figure 5.7 shows the per

MulD Efficiency 5GeV Muons

Efficiency

HW Efficiency

Realistic Panel Efficiencies
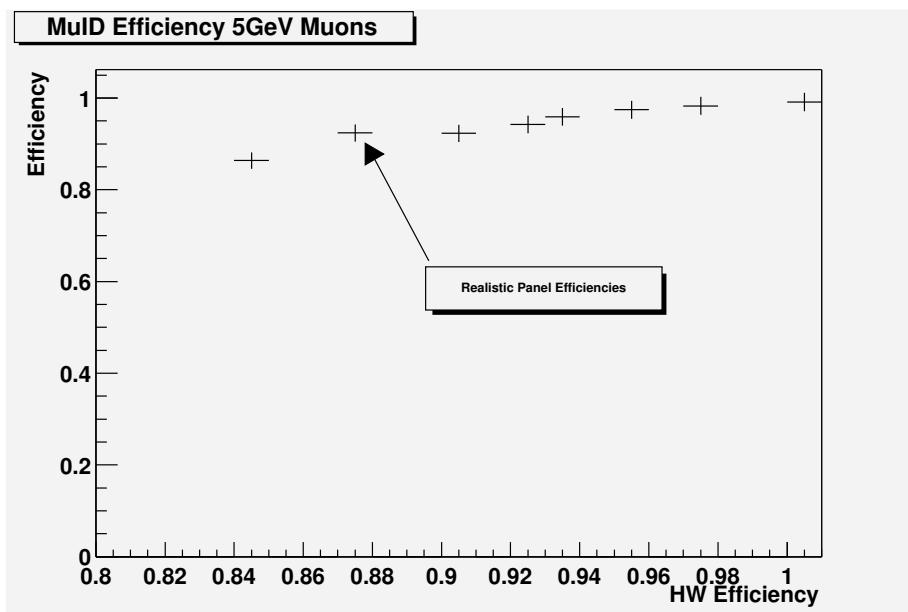
Figure 5.5: Simulated efficiencies for 5 GeV/c muons. The ordinate value indicates the hardware efficiency used for the detector. The ordinate value for the point labeled "Realistic Panel Efficiencies" is an average from the efficiencies derived using $p + p$ data as discussed later in this chapter. The other points represent each twopack being given the same efficiency.
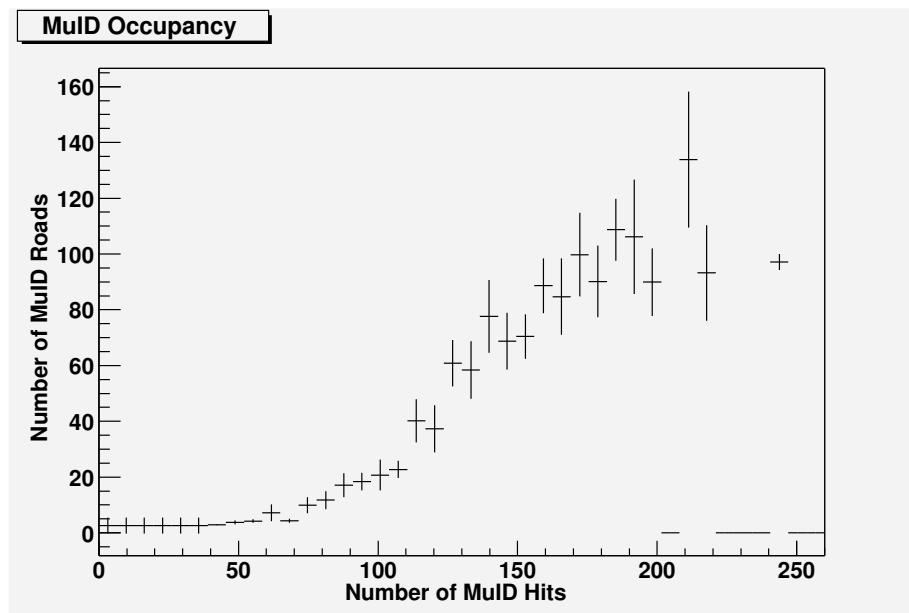
Figure 5.6: MuID road count as a function of hit multiplicity after the first pass road-finder. A minimum bias event has an average of approximately 80 hits or a 2.5% occupancy.
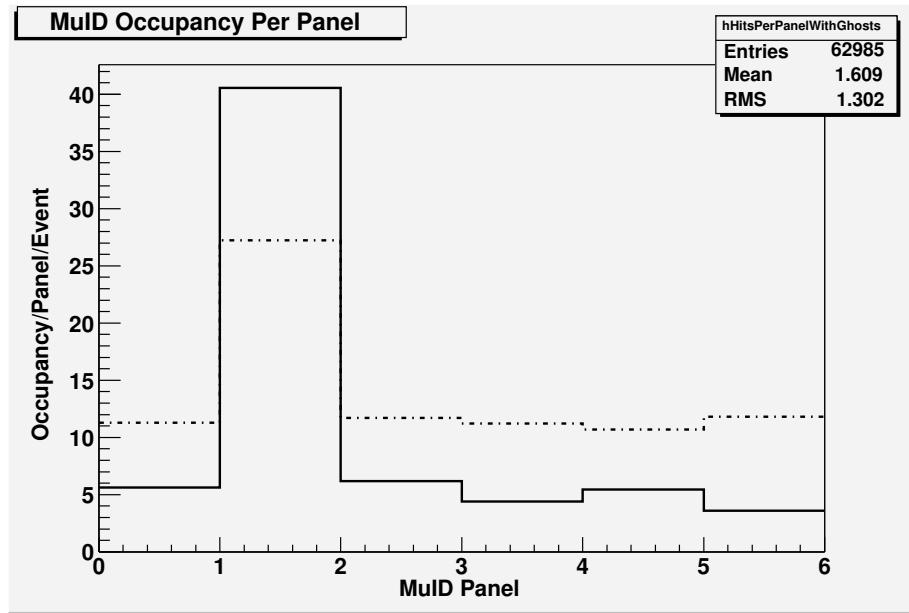
Figure 5.7: MuID hit and road occupancies per panel. The dashed line is hit occupancy and the solid line is road occupancy before road grouping in the first pass road finder.

panel occupancies for minimum bias events. The shielding issues discussed in chapter 4 are clearly visible in panel 1.

5.4   Detector Occupancy

It is important to study the detector occupancies due to the impact on reconstruction efficiency. Figure 5.8 shows the expected trend that occupancies vary significantly with centrality in both the MuID and MuTR, but more interestingly, these show that there is no large vertex dependence. Any large vertex dependence would significantly complicate the study of yields as a function of event vertex.

Figure 5.9 shows the occupancy distribution for the first and last tracker station for several centrality classes. The occupancy varies much more dramatically for Station I and is over 20% for the most central events. An event display of a Au+Au event, Figure 5.10, shows the challenge presented to the reconstruction software. The distribution of reconstructed roads at Gap 0 is shown in Figure 5.11. Due to the increased occupancy above the MuID square hole, a cut, described later in this chapter, is used to remove roads from this section of the detector.

Even though the average occupancy in the MuID is only 6% for the 15% most central events, the local occupancies can be much higher. Figure 3.20 shows the large spread in hit multiplicity for a given centrality, and Figure 4.3 demonstrates that the multiplicity in Gap 0 is much higher than the average. There is additional localization of multiplicity in the detector plane as indicated by the highly non-uniform distribution of roads as shown in Figure 5.11. While an evenly distributed 10% occupancy would probably cause few reconstruction issues, the locally dense regions present in the data pose a significant challenge.
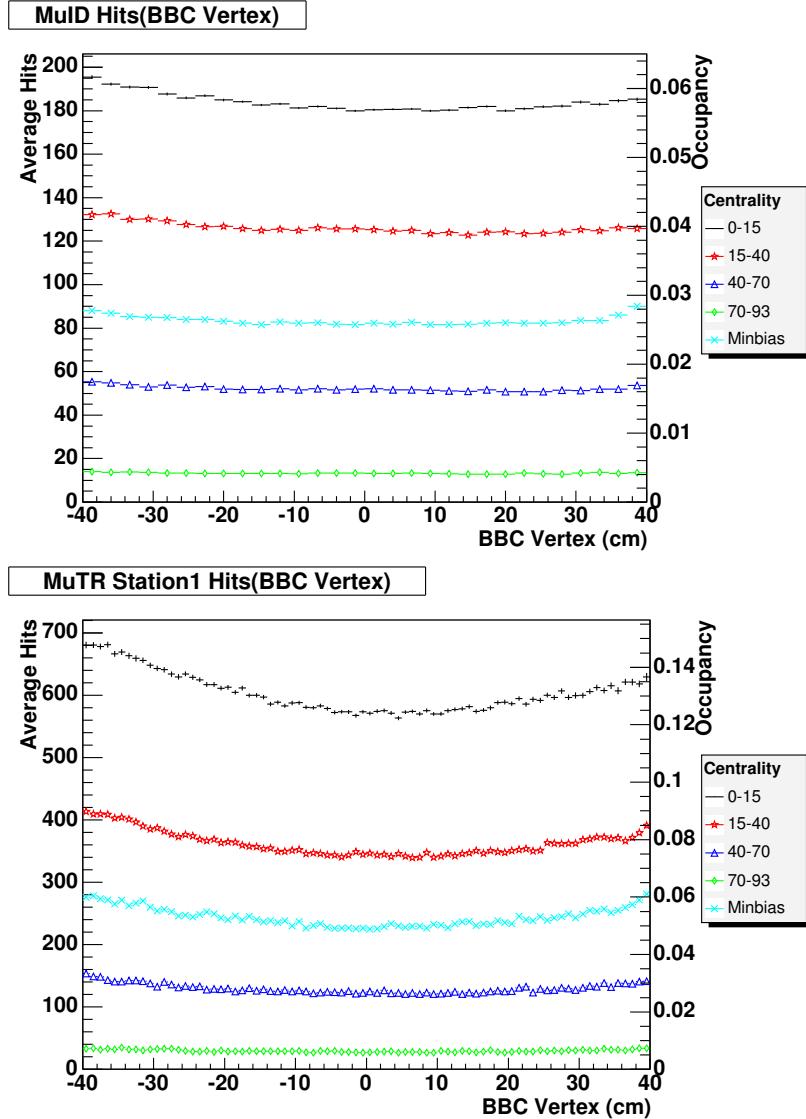
Figure 5.8: Average number of hits in the MuID (Top) and charged cathodes in the MuTR (Bottom) as a function the event vertex for several centrality classes of Run II Au+Au data. There is only a few percent change in detector occupancy over the vertex range of $-20 < Z_{vertex} < 38$ used for this analysis, but there is a larger change in MuTR occupancy than in the MuID. The rise on the right is due primarily to increased hadron decays, while the increase on the left is likely due to decreased absorber lengths for particles which enter the nose cone from the beam pipe hole. All centrality classes exhibit a very similar shape.
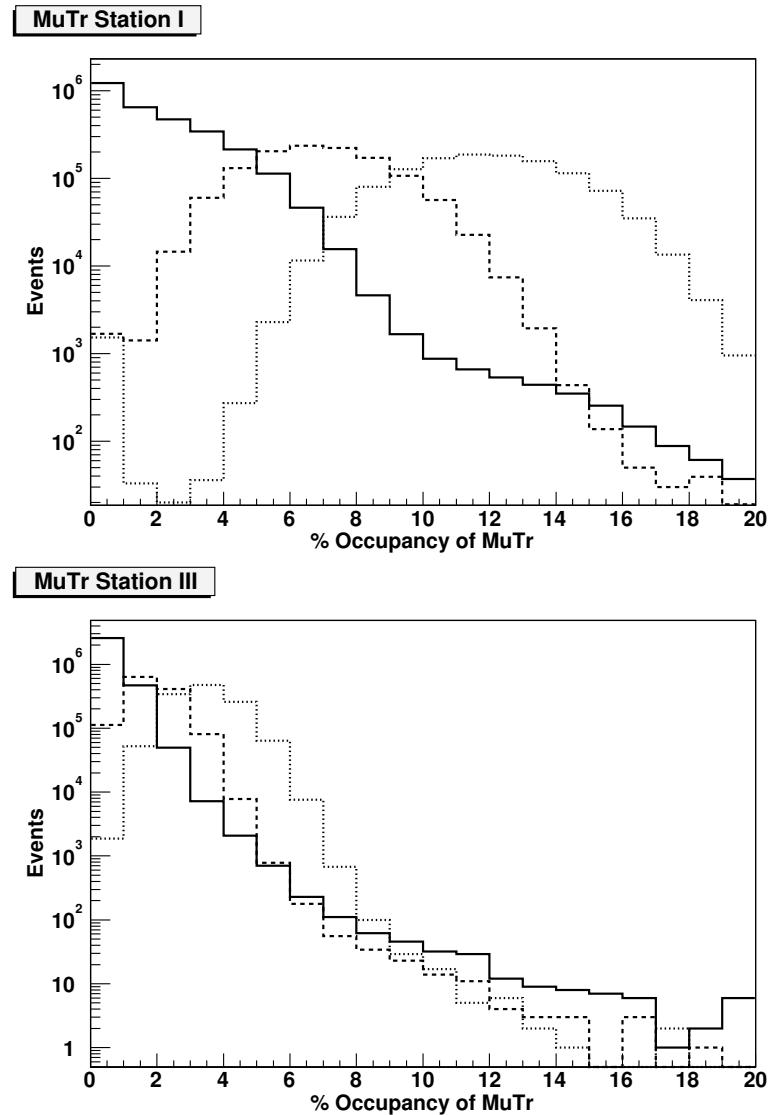
Figure 5.9: MuTR occupancy distributions for Run II Au+Au data. The 0-20% most central is dotted, 20-40% is dashed, and 40-90% is solid. The occupancy in Station I increases much quicker with centrality than the other stations.
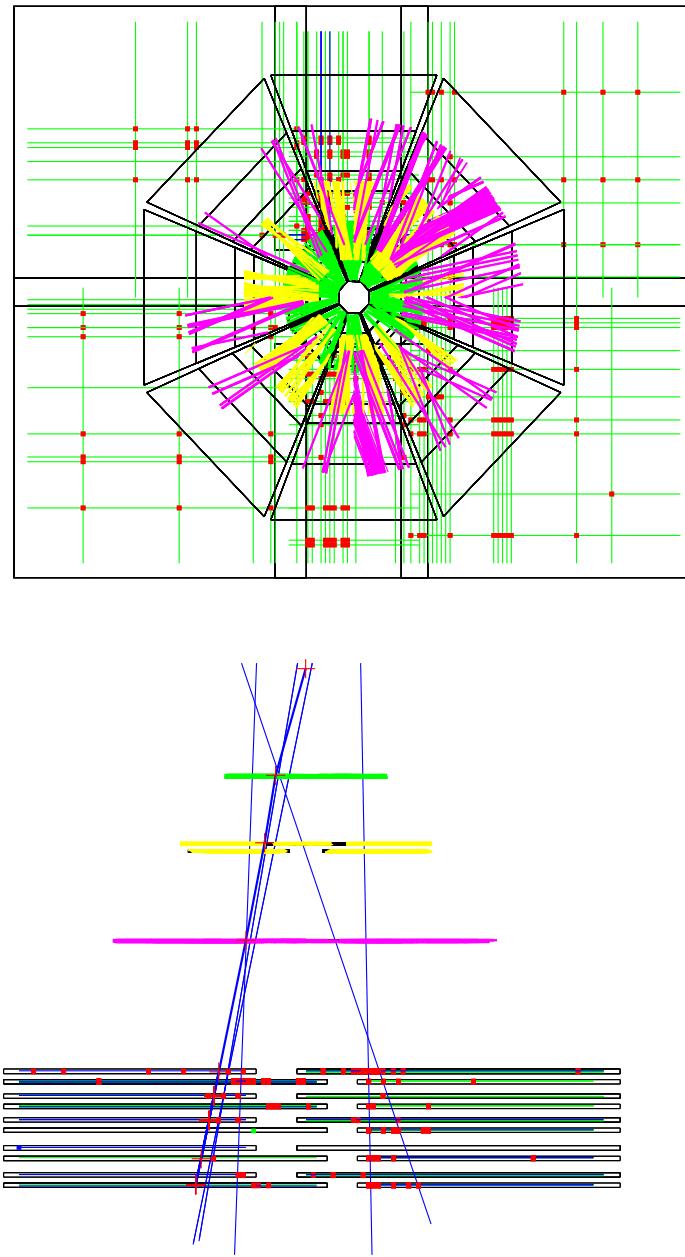
Figure 5.10: Event display of a Run II Au+Au event. The top view shows the detector as seen from the beam line. The horizontal and vertical lines represent struck MuID twopacks, and the roughly radial lines show charged cathodes. The separate detector planes can be seen from the side view (bottom). Reconstructed roads are shown projecting through the MuTR and MuID.

Gap 0 road intersection
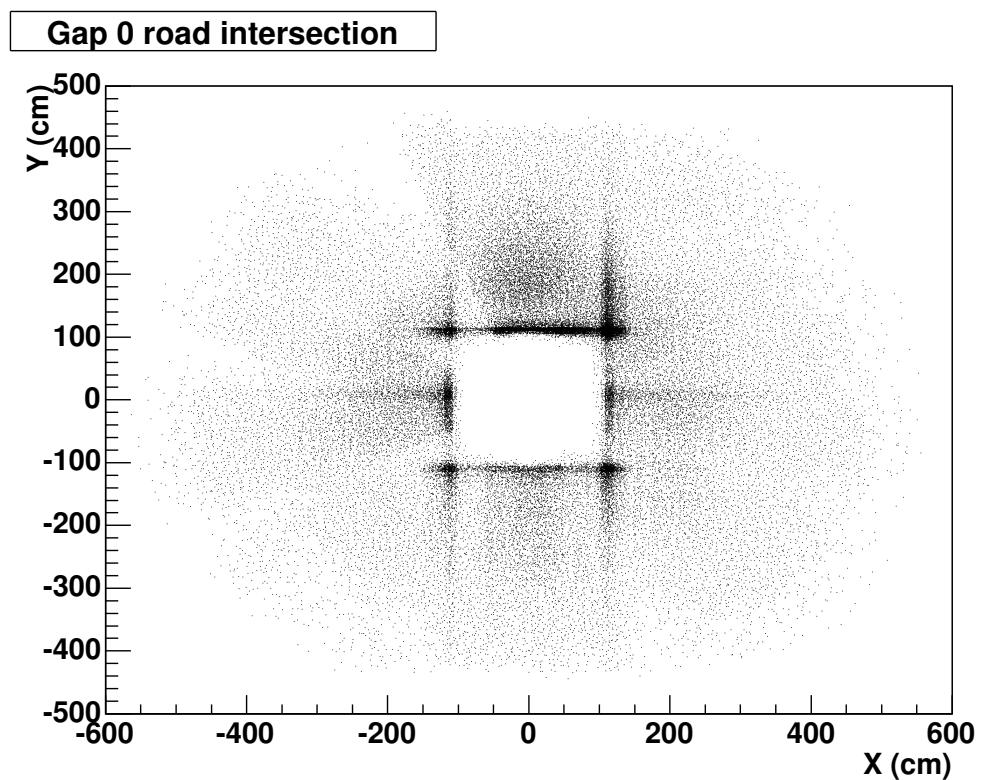
Figure 5.11: MuID Gap 0 road intersection distribution. Some notable features are: 1) regions of increased hit density due to panel overlaps 2) increased background around the square, and 3) increased occupancy above the square hole concentrated in the small panel due to the lack of ceiling shielding during Run II.

5.5 Sources of "Muons"

The cross section for prompt single muon production directly reflects the open charm production cross section. It is very important to measure both the open charm and the charmonium cross sections in order to unravel the relative contributions from charmonium suppression, a possible result of color screening, and charmonium enhancement, as predicted by coalesesence/recombination theories. Since charm production is sensitive to gluon distributions, single muon production may be subject to interesting initial state effects such as gluon saturation and the postulated color glass condensate.

The main sources of muon candidates, or reconstructed particles, from RHIC Au+Au (and $p+p$) collisions are shown in Figure 5.12. Muons from D, and to a lesser extent B, mesons are generated when a D (or B) decays into $\mu + X$ very close to, < 1cm, the event vertex. These "prompt" muons comprise the signal for open charm production which is to be extracted. Another source of true muons comes from π and K decays, which occur much farther from the event vertex. The relative contribution of these decays has a vertex dependence which can be exploited, as discussed later. The other source of muon candidates is non-muons, usually hadrons, which penetrate the MuID. These include particles which are generated at the vertex and the products of their strong interactions. By studying, characterizing, and simulating these sources of background, one can subtract them from the total signal and obtain a measure of prompt muon production.

5.5.1 Prompt Muons

Prompt muons from semi-leptonic D decays, such as the example in Figure 2.2, are the signal of interest for this analysis. Prompt muons are also produced from B decays as well as J/Ψ and similar decays. These other sources are expected to be small over the kinematic range available from the current data. Various contributions to the muon p_T specta are estimated using PYTHIA are shown in Figure 5.13. The simulation shows
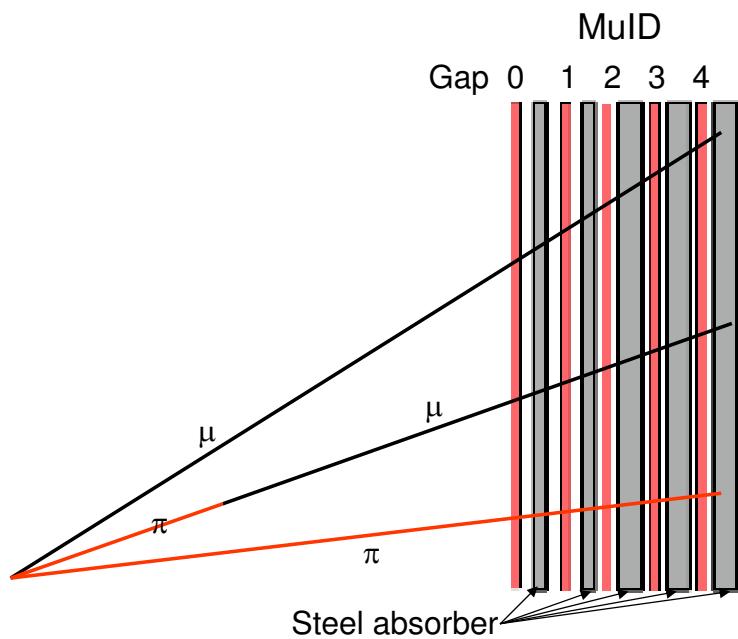
Figure 5.12: Sources of muon candidates. *D*, and to a lesser extent *B*, mesons decay semi-leptonicly to produce muons very close to the vertex. Hadrons decay, $\pi^{\pm} \rightarrow \mu^{\pm}\nu_{\mu}$ and $K^{\pm} \rightarrow \mu^{\pm}\nu_{\mu}$, much farther from the vertex. Hadrons which do not decay have a chance to pass through the absorber material.

Muon Pt; bb,cc, qcd events

hccm
Nent = 281266
Mean = 0.8156
RMS = 0.2859

MC

$\pi^{\pm} / K^{\pm} \to \mu^{\pm}$

$c \to \mu$

$b \to \mu$
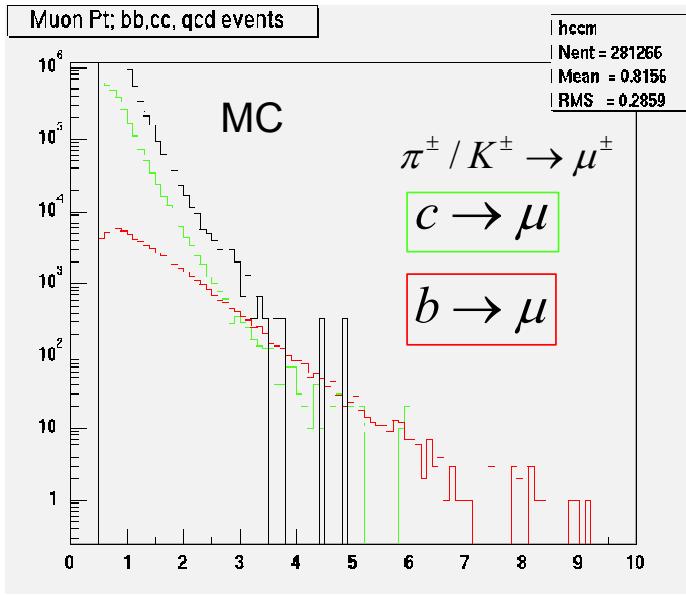
Figure 5.13: Simulated p_T specta for muons from hadron decays, charm decays, and bottom decays [67]. At low p_T, the top curve is for muons from hadron decays, the middle curve is for muons from charm decays, and the lower curve is for muons from bottom decays. Charm decays are expected to dominate the prompt muon yield for $p_T < 2.5$ GeV/c.

that muons from charm decays are expected to dominate over muons from bottom decays for $p_T < 2.5 \text{GeV}/c$

5.5.2 Decay Muons

The dominant source of muons, particularly at low p_T, in the MuID are from hadron decays. Charged pions and kaons decay via the weak force into muons and neutrinos. Although typical $\gamma c \tau$ can approach 100m, 78m for a 1.4 GeV π, the large hadron multiplicities allow a significant number of decays before reaching the nose cone. The decay probability for a hadron created at vertex, z_{vtx} is given by $p_\mu(z) = \frac{1}{\lambda_d} \exp(-\frac{z - z_{vtx}}{\lambda_d})$, where $\lambda_d = \gamma c \tau$. Assuming the probability per unit length to create a hadron at z_{vtx} is uniform, $P_H(z_{vtx}) = \frac{1}{L}$ where L is the distance over which hadrons are created, the distribution of muons from hadron decays, as show in Appendix A, becomes

$$N(z_{vtx}) = \frac{1}{\lambda_d} z_{vtx} - \frac{z_0}{\lambda_d} \tag{5.1}$$

for hadrons traveling south, negative z. Any number of hadronic sources add to produce the same functional form.

For Au+Au data, a select region of η, as described later in Section 5.9, which has a reconstruction efficiency independent of the event vertex needs to be analyzed to avoid a change in the vertex distribution due to geometric acceptance. Also, the minimum bias event vertex distribution, shown in Figure 5.14 is not uniform, so the raw muon vertex distribution, Figure 5.15, is divided by the event vertex distribution. A particle vertex distribution after event vertex division from Run II Au+Au data is shown in Figure 5.16 to demonstrate the very linear rise due to decay muons. The specific quality cuts are described in Section 5.9. The slope of the graph cannot be readily used to extract a λ_d since it depends on the reconstruction efficiency, acceptance, and multiplicity for the hadrons.

The linear vertex dependence of decay muons can be exploited to help study and
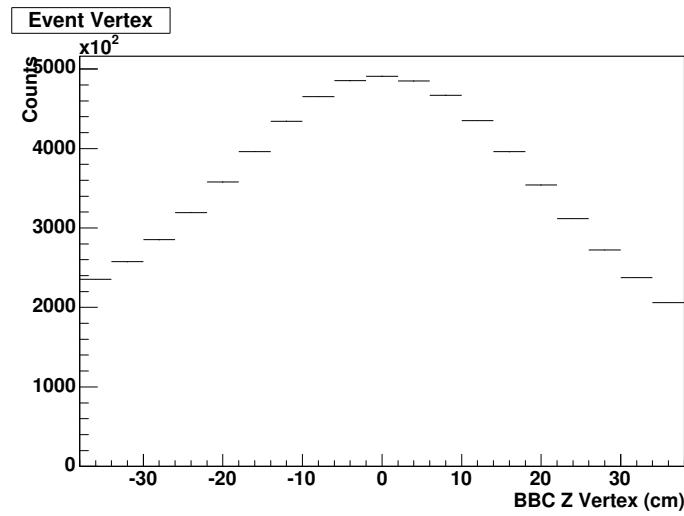
Figure 5.14: Minimum bias event vertex distribution for runs used in this analysis.
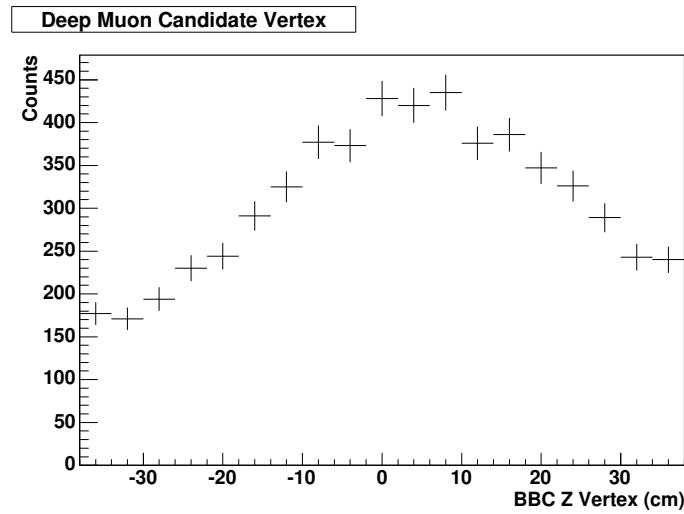
Figure 5.15: The vertex distribution of muon candidates which appear to penetrate the entire MuID. The graph is for centrality > 20 and $1 > p_T > 3$ GeV/c. Specific quality cuts are discussed in Section 5.9.

108
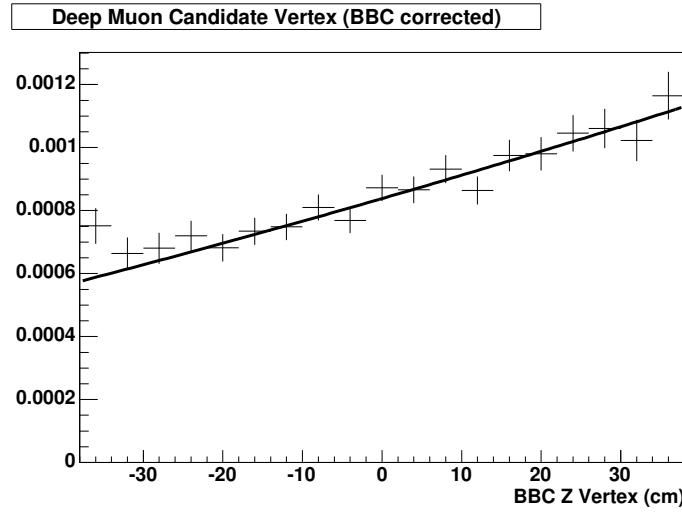
Figure 5.16: Example muon candidate vertex distribution. The graph is for centrality >
20 and $1 > p_T > 3$ GeV/c. The rise near -30 cm is primarily due to the geometric effect
that particles close to the nose cone may enter the absorber from the inside the beam
pipe hole rather than the face. This reduction in absorber length causes an increased
hadron contribution. To avoid this nonlinear region, only events with $-20 < Z_{vertex} < 38$
are used in this analysis.

subtract the decay component. Subtracting distributions of muon candidates from collisions near the detector from those of candidates from collisions far from the detector allows study of decay muon properties. Simulations to measure z_0, as discussed later in this chapter, allow measure of the total decay contribution. Also, an analytical estimate of z_0 is presented in Appendix A. Since $f(x) = mx + b$ has the same y-intercept as $g(x) = K(mx + b)$, matching the detector efficiency in simulation is less important than for an absolute subtraction.

5.5.3   Punch-through and Interacting Hadrons

Hadrons which do not decay can also produce roads and tracks in the Muon spectrometer. There is a small chance that pions and kaons can penetrate into the MuID without experiencing a strong interaction in the proceeding absorbers. These hadrons become a more significant source of background with increasing transverse momentum. Even if a hadron does suffer a strong interaction, it can result in a reconstructed particle. The interaction can take place deep in the MuID, or a secondary particle produced from the strong interaction may extend the apparent trajectory. Some of these aspects of hadron punch-through are demonstrated in the simulated event shown in Figure 5.17 Many of these can be removed on a single event basis as discussed below, but estimating the remaining contribution is left largely to simulations.

5.6   Muon-Hadron Separation

The PHENIX MuID is designed to take advantage of a fundamental difference between muons and hadrons. Hadrons can interact with matter via the strong force, while leptons, specifically muons, do not. This means that, statistically, a muon is able to penetrate more of MuID absorber steel than a hadron with the same energy. Of course charged hadrons and muons both interact electromagnetically. This means that in in-

110
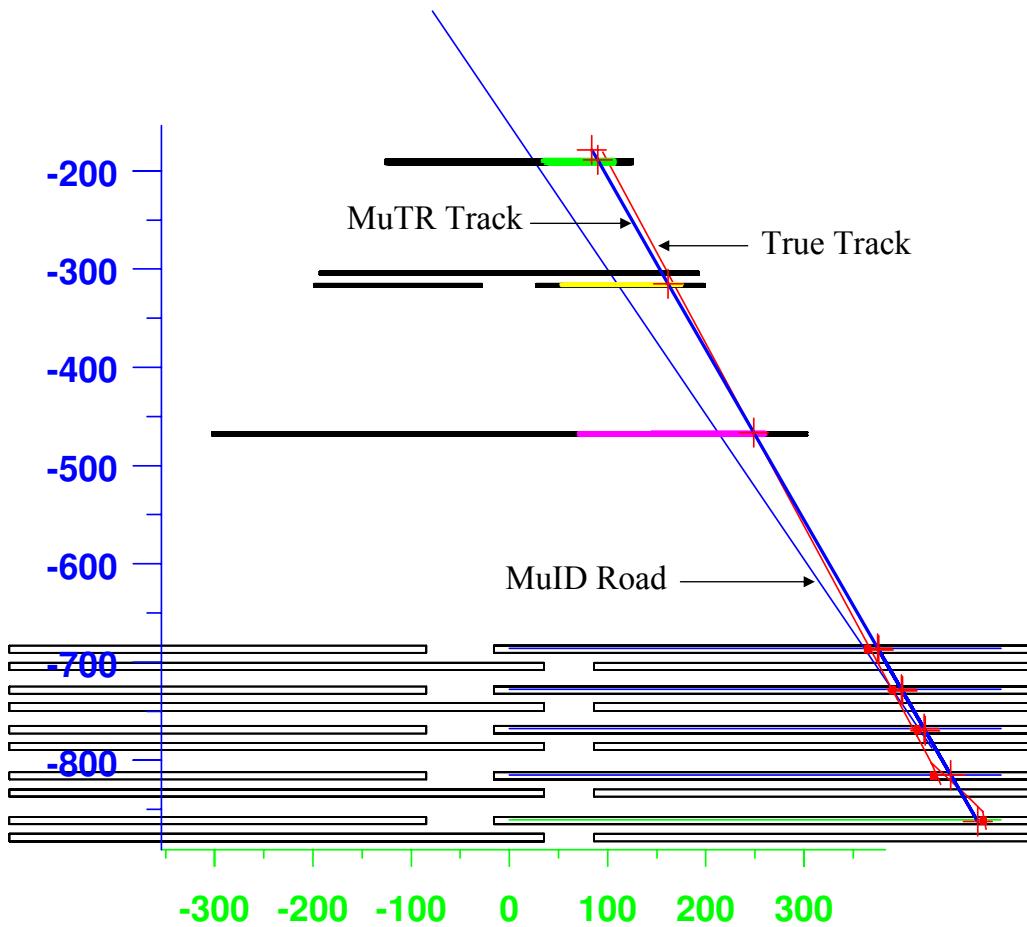
Figure 5.17: Event display representation of a penetrating hadron which results in a reconstructed particle. The hadron has an interaction in the absorber preceding Gap 3, and the resulting partices cause hits in gaps 3 and 4. This particular event would be very hard to distinguish from a muon. Since the road was reconstructed to Gap 4, there is no chance of a depth/momentum mis-match.
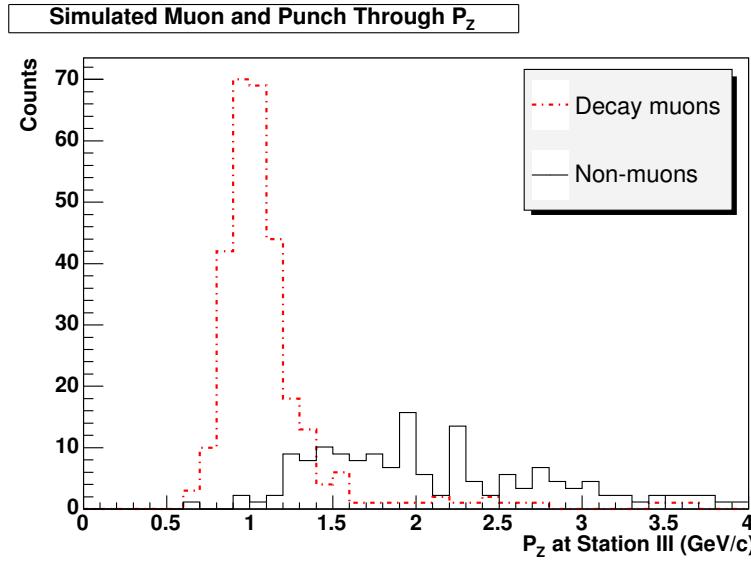
Figure 5.18: Simulated longitudinal momentum distributions for decay muons and interacting hadrons which stop in Gap 3. Only muons within a small momentum range are stopped at Gap 3 while hadrons have no peak and a large spread.

stances where a hadron losses all or most of its kinetic energy via Coulomb interactions before suffering a strong interaction, the hadron is basically indistinguishable from a muon. Fortunately, the probability that a hadron will have a strong collision is high enough to allow for significant distinguishing power as is demonstrated in Figure 5.18. The figure shows that for simulated hadrons which are passed through the full reconstruction chain, the decay muons which only penetrate to Gap 3 are grouped in a tight momentum range while the non-muons are likely to be stopped even at much higher momenta. The specifics of the simulation is discussed later in Section 5.8. The quicker stopping of hadrons also means that the ratio of muons to hadrons quickly increases with penetration depth. This effect is demonstrated in Figure 5.19.

For gaps other than the last gap, looking at particles with p_Z above the stopping peak should allow for a clean sample of non-muons. The vertex distribution of high p_Z particles from Run II Au+Au data with last gaps of 2 and 3 gives support for this interpretation. The flat shape of this distribution is very distinct from that of deep muon

112

Simulated MuID Penetration
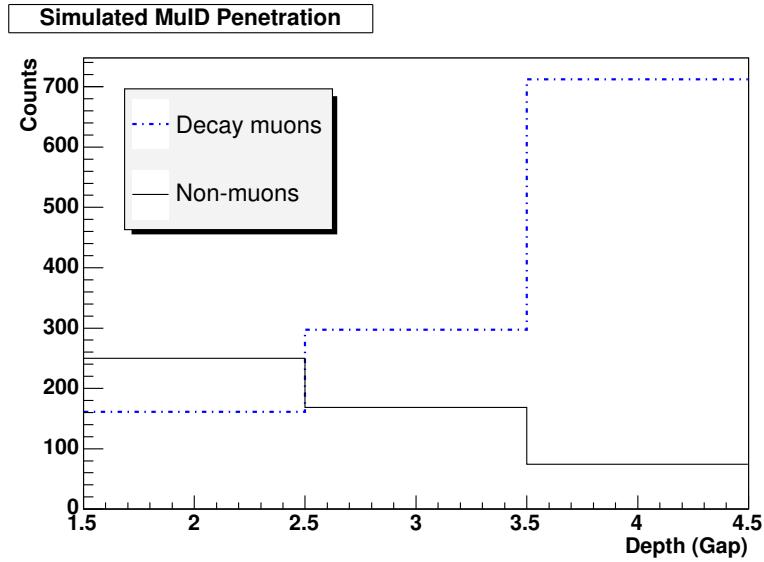
Figure 5.19: Simulated MuID penetrating depth distribution for decay muons and non-muons. The muon to hadron ratio quickly increases with depth. These were produced from simulations using the BRAHMS measured rapidity and p_T spectra as described later in this chapter.

candidates shown in Figure 5.16, as can be seen in Figure 5.20. The lack of a vertex dependence implies that there is no significant decay muon contribution. The distribution must be dominated by non-muons since the absence of decay muons requires the absence of prompt muons. Decay muons, especially for pions, are generally indistinguishable from prompt muons on an single event basis.

Particles with a last gap of 4 actually penetrate the entire detector, so no momentum cut can be used to help separate hadrons and muons. A method using hadron contamination measured at shallower gaps to extrapolate to Gap 4 is currently under investigation within PHENIX. Figure 5.21 shows simulated decay muon p_Z distributions for all gaps. Recall that the reconstruction software requires a road to penetrate to at least Gap 2.

It is important to note that the efficiency of these methods depends strongly on correctly reconstructing the penetration depth. The occupancies of Au+Au collisions and

Hadron Candidate Vertex Distribution
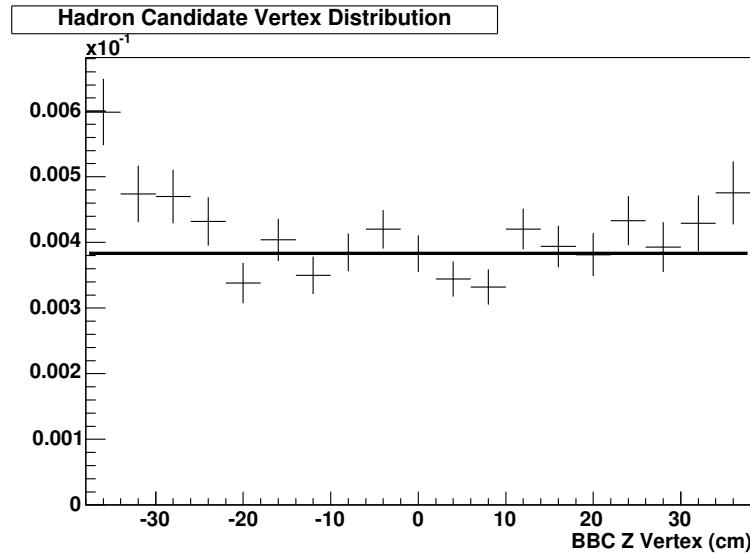
Figure 5.20: The vertex distribution of hadron background candidates. Particles with p_Z above the stopping peak show a flat vertex distribution. The distributions is made using the same method as Figure 5.16. The rise due to decreased absorber length is again seen for particles close to the nose cone. Points with BBC Z Vertex < -20 were not used in the fit.
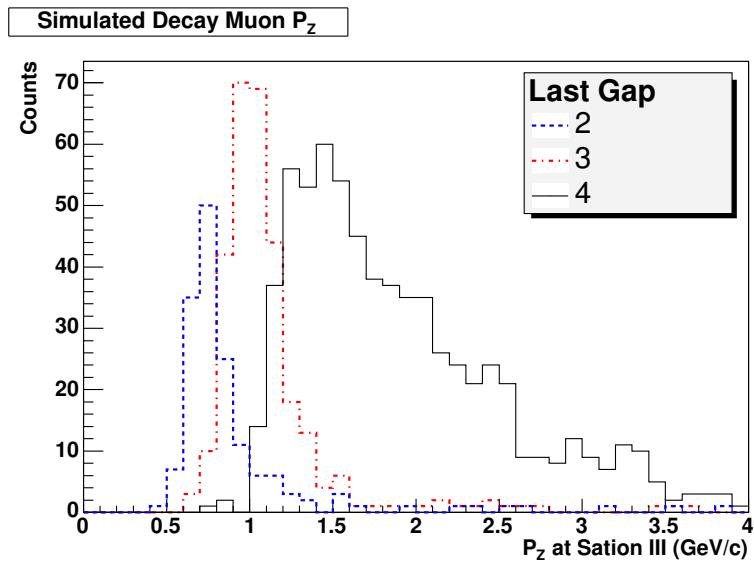
Figure 5.21: Simulated longitudinal momentum distribution for decay muons at different depths. The muon stopping peaks at Gap 2 and 3 show some overlap; this is enhanced due to detector inefficiencies which shorten some roads. The Gap 4 distribution does not have a peak since the particles did not stop before penetrating the entire detector.

the hardware efficiencies of the detectors during their commissioning run can contribute to artificially extending and shortening roads respectively.

Since hadrons can produce showers of many particles when they experience a strong interaction, shower spotting algorithms have the potential to further reduce hadron contamination. Unfortunately, the implementation of such algorithms was hampered in the high background environment of the commissioning run.

5.7   Acceptance and Efficiency

5.7.1   MuID Efficiency

Estimating hardware efficiencies for the MuID was a critical step for both commissioning and data analysis. For commissioning and trouble shooting the detector, a highly simplified version of the offline reconstruction software reconstructs cosmic-ray data using the MuID first pass road finder. The cosmic-ray data is collected using the MuID NIM-logic Level 1 trigger. The NIM-logic trigger is a quadrant based trigger which uses information from 4 of the 5 MuID gaps in one arm. To avoid a trigger bias, the data used to study a given gap, gap X, has that gap removed from the trigger. Gap X is also removed from the search order during reconstruction. Once the roads are reconstructed, quality selection is done on the roads. These roads are then projected to gap X, and hits are searched for in each orientation around the projected intersection. A number of expected hits, N_e , and a number of recorded hits, N_r, are recorded for each twopack. If no hits are found in the search window, N_e is incremented for the twopacks which the projected road passes through. If hits are found, the N_e and N_r are incremented for those twopacks. Since roads do not necessarily penetrate the entire MuID if Gap X is the first or last gap, a hit is required to be found in the orthogonal orientation before a measurement is made. For example, if the efficiency is being measured for Gap 0 horizontal, a vertical hit must be found in the window of the projection

116
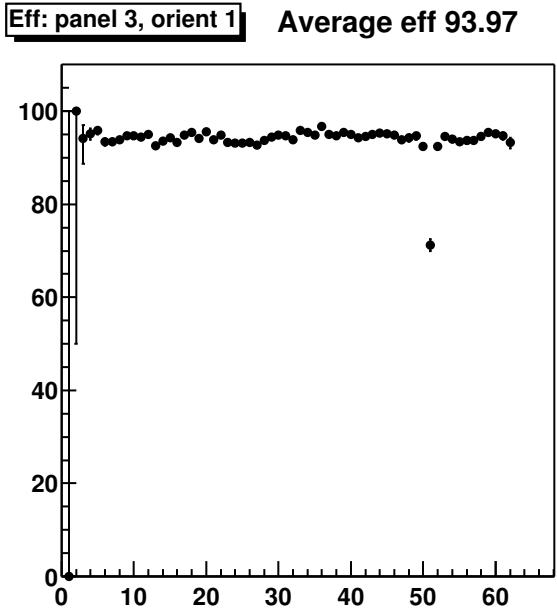
Figure 5.22: The efficiencies for a healthy MuID panel measured using cosmic rays. A single inefficient twopack, channel 50, can easily be seen.

before a measurement is attempted. The measured efficiency for each tube is given by $\epsilon = \frac{N_r}{N_e}$. Although there is some smoothing due to the small overlap of twopacks, multiple scattering, and detector edges, this method allows easy identification of single twopacks whose efficiency deviate significantly from their neighbors. A typical cosmic ray efficiency distribution for a healthy MuID panel is shown in Figure 5.22, and Figure 3.15 shows the distribution for the entire South arm.

Due to the higher occupancies in Au+Au collisions, this method of estimating efficiencies was not possible. Too few "clean" events were available. Due to increased shielding, better statistics, and improved software, it may be possible to use similar direct methods for later heavy ion data sets. One exciting possibility is to record cosmic-ray data during empty-empty beam crossings. Since the MuID hardware efficiencies are highly correlated with the high voltage values for the Iarocci tubes, an indirect method of estimating the efficiency from the high voltage state was investigated. Although

much progress was made, problems with incorrect high voltage read back and inadequate logging made this technique unreliable. Since no major system changes were made between Au+Au and $p + p$ data taking in Run II the average efficiency of MuID during the $p + p$ should be a fair estimate of the Au+Au period.

For Run II $p + p$ data, a simplified method was used to measure the MuID hardware efficiency [68]. The efficiencies were measured for each orientation of a total panel due to resource and statistical limitations. Thirty-seven randomly chosen runs were analyzed to represent the running period. The efficiency for each panel/orientation, ϵ_N, was defined as, $\epsilon_N = \frac{\text{Reconstructed roads with a hit in N}}{\text{All reconstructed roads}}$. Although much MuID Level 1 triggered data was taken, only minimum bias events were used, since the gap excluded from the MuID Level 1 was not changed during data taking.

Ideally, the gap of interest, gap X, would not be in the reconstruction search order, but since the road finder allows skipped gaps no significant effect is seen. However, gap X should not be a seed gap. The search order sets [2,1,3,4,5] and [1,2,3,4,5] were used for gaps 3,4, and 5, and the search order sets [4,5,3,2,1] and [5,4,3,2,1] were used for gaps 1,2, and 3. The gap 3 measurements for the 2 different search order combinations were found to be consistent within statistical uncertainties. Only very clean roads were used for the analysis. The cuts include: 1) the road is the only road in the event, 2) the road appears to penetrate the entire MuID, 3) there is a hit in the opposite orientation for gap X, and 4) adjacent planes have at least one hit. The distribution of the panel efficiencies is shown in Figure 5.23.

The process of reconstructing roads excluding the gap of interest and later looking for a hit in that gap, as was done with cosmic rays, was also used with $p+p$ data. In order to improve statistical fluctuations, the efficiencies were averaged over all twopacks in each high voltage chain. The average value was then assigned to each twopack in the chain. The twopack efficiency distribution from the $p + p$ measurement which is used for Run II Au+Au simulations is shown in Figure 5.24.

118
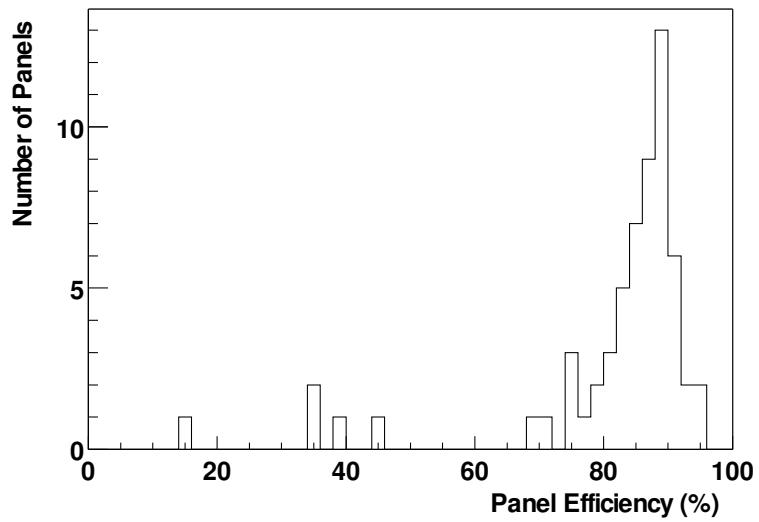
Figure 5.23: The efficiency distribution for the south MuID panels as measured using Run II $p + p$ data.
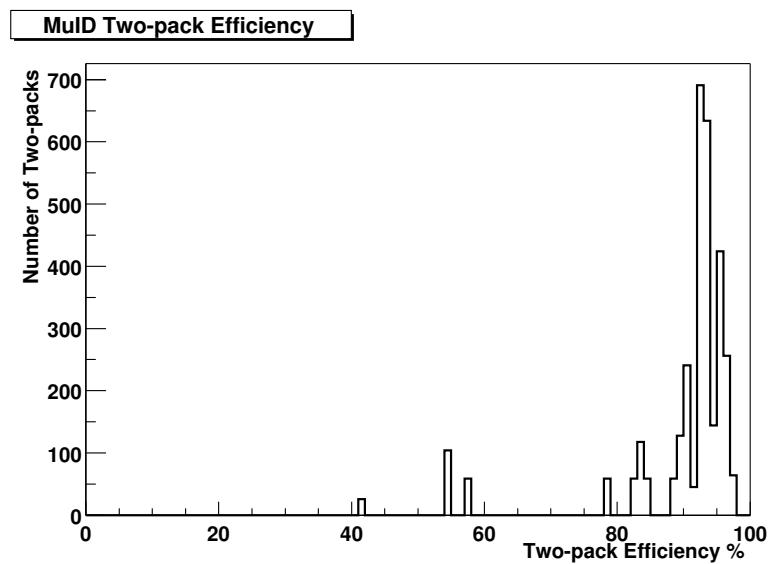
Figure 5.24: The twopack efficiency distribution for the south MuID as measured using Run II $p + p$ data. Each channel in a high voltage chain is assigned the average value, averaged over runs. This measurement is used for Run II Au+Au simulations.

5.7.2 MuTR Efficiency

The efficiencies of active regions of the MuTR are $\approx 99\%$. The main deviations in MuTR efficiency are from completely inactive sections caused by disabled high voltage chains and non-functional Front End Modules. If the detector geometry and the status of these electronics modules are well known, modeling the MuTR response by masking these dead regions should be fairly straightforward. The simulated efficiency based on hardware status was directly compared to $p+p$ data. The measured efficiency is defined as

$$\epsilon_{MuTR} = \frac{\text{The number of MuID roads with a MuTR track}}{\text{The number of MuID roads}}. \tag{5.2}$$

This quantity was measured for both real and simulated data. Cuts on road quantities, such as distance between the road intersection and the z axis in the $z = 0$ plane, were made to reduce the contribution of background roads.

The efficiency measurements show good agreement between data and simulation as seen in Figure 5.25. As discussed in Chapter 4, only runs where more than 81.5% of the MuTR high voltage chains were active are used in this analysis.

5.7.3 Total Muon Efficiencies

The total efficiency of the muon spectrometer is estimated with detailed GEANT simulations which are passed through response software which reflects the best understanding of the detector's efficiency. Figure 5.26 shows the estimated total J/ψ efficiency [6] and the estimated single muon efficiency after correcting for loss due to opening angle and assuming pair efficiency $\approx$ (single efficiency)^2. Also, the of 25% of the azimuthal acceptance which is removed for the singles analysis in order to reduce backgrounds from the unshielded section of the MuID as described later in this chapter, is accounted for. The peripheral efficiencies are compared to $p + p$ estimates later in this chapter.
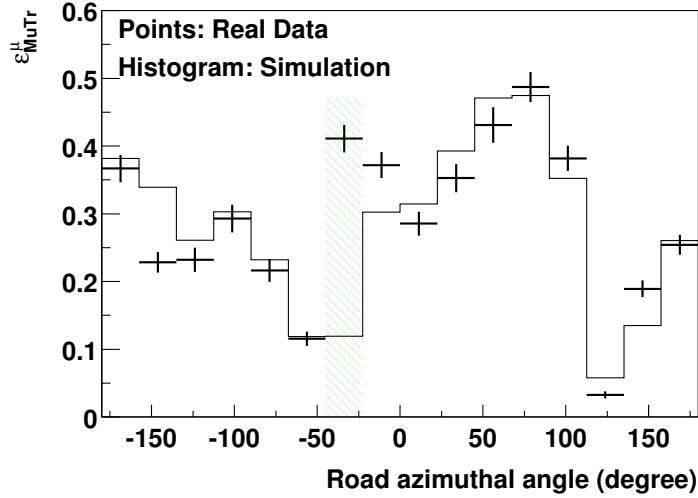
Figure 5.25: The azimuthal distribution of measured and simulated ϵ_{MuTR}. Good agreement is seen between the MuTR efficiency measured in $p + p$ data and simulated using the recorded hardware, high voltage and FEM, status. The discrepancy at $\phi \approx 30°$ is due to an understood issue in the response software.
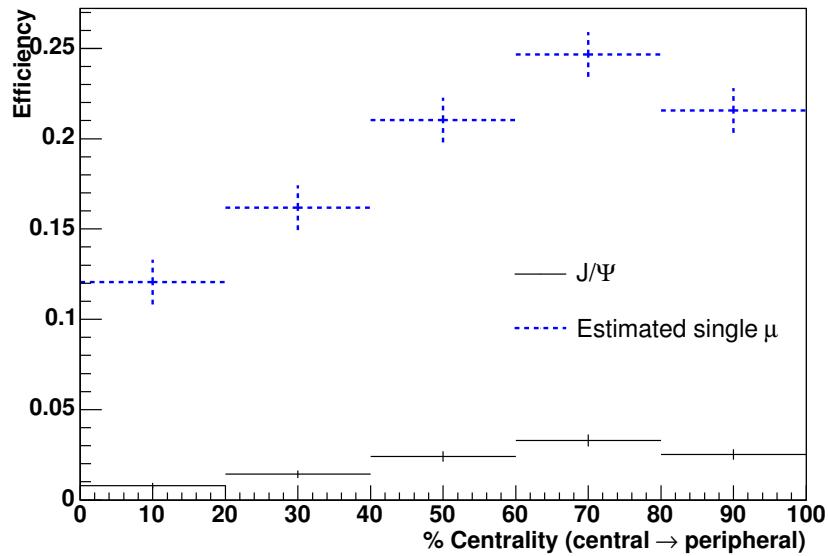
Figure 5.26: J/ψ efficiency (solid) [6] from simulations and the estimated single muon efficiency (dashed).

5.8   Cocktail Simulations

Detailed simulations are employed to help estimate decay and punch-through background contributions. One very important aspect of producing realistic simulations is beginning with realistic kinematic input for the simulation software. Therefore, experimental hadron measurements in this kinematic region are the ideal seed information. This generator incorporates data from the BRAHMS experiment [69], but the potential for using data from PHENIX central arm measurements, which is rapidity scaled by the measured rapidity distribution is discussed. Prior to the availability of such data, similar simulations depended on packages such as HIJING to produce this input, but considering the lack of tuning for RHIC energies and the computing resources required for useful statistics, only the data driven particle generator is discussed for this analysis.

Scaling central rapidity measurements to forward rapidity for input to the generator requires that to a high degree the functional form of particle production in rapidity and transverse momentum for a given species can be factorized into separate functions, i.e. $P(y, p_T) \cong P(y)P(p_T)$. The spectra shown in figure Fig. 5.27 demonstrate the good y independence for $\pi^\pm$ p_T spectra. A more direct demonstation of this is shown in Fig. 5.28 where the individual BRAHMS spectra are scaled up to the production expected at $y = 0$ using an absolute scale factor derived from the measured rapidity distribution in Fig. 5.29. The PHENIX spectra have a greater p_T reach, which allows the generator to be based on direct measurement over a larger kinematic range, and only data from the 0-5% most central collisions are currently available from BRAHMS.

These extrapolated hadron spectra for Muon Arm rapidities can then be used as input for simulations.

The simulations for this analysis used 1M single hadrons generated based on the 5% most central distributions from BRAHMS data. Single particles are produced with the proper distributions. These are then passed through PISA to produce hit files. The PISA hit files are then filtered using hit ancestry information into decay events and
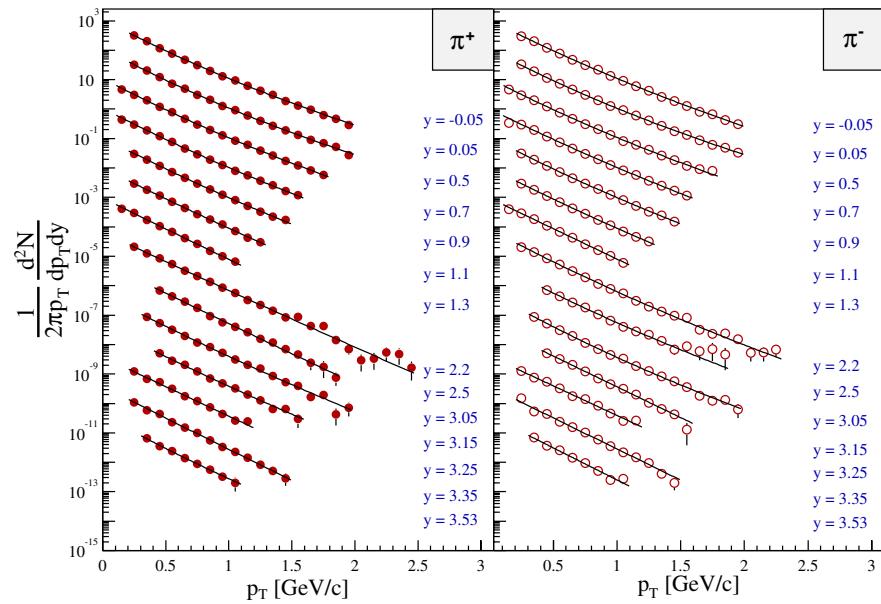
Figure 5.27: Preliminary transverse momentum spectra from the BRAHMS experiment for 5% most central collisions [69]. Each specra is scaled by factors of ten.
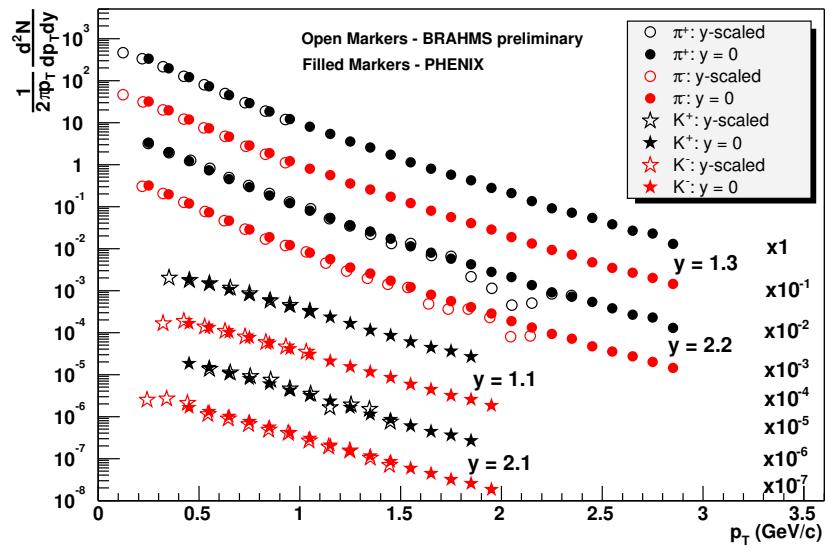
Figure 5.28: Comparison of PHENIX mid-rapidity p_T spectra with scaled forward BRAHMS measurements for 5% most central collisions [69].
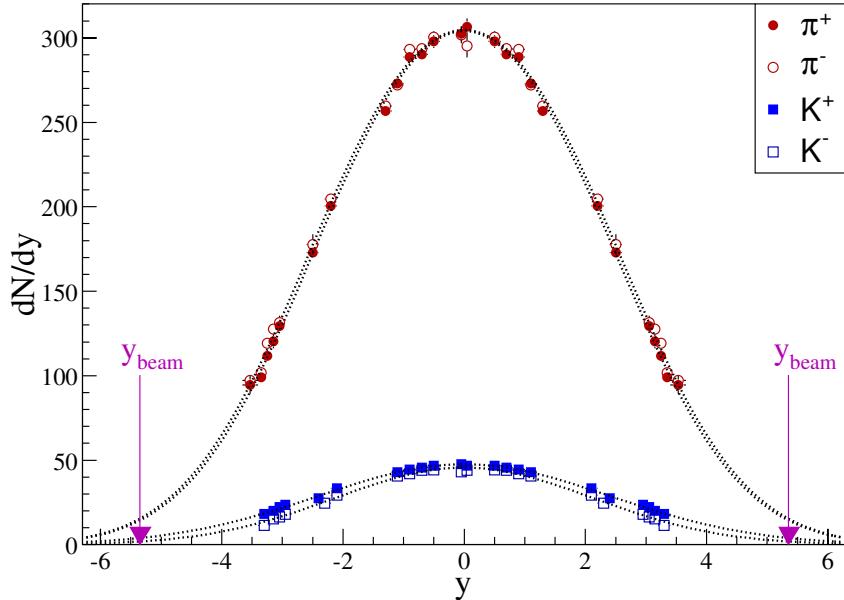
Figure 5.29: BRAHMS preliminary rapidity densities for 5% most central collisions [69].

punch-through events. These files are then passed through the full detector response and reconstruction software.

5.8.1 Simulation Results

Some of the basic results of these simulations have been presented earlier in this chapter, Figures 5.18, 5.19, and 5.21, which include estimates for the ratio of decay muons to hadron background at different depths. One of the goals of this simulation was to estimate the z-intercept of the extrapolated decay contribution, z_0 in equation 5.1. The simulated decay distribution shown in Figure 5.30 indicates a $z_0 = -65 \pm 30$ cm. The z_0 value from simulation is consistent with the analytical estimate of $z_0 = -56.3$ cm in Appendix A.

The other major goal of these simulations is to estimate the non-muon, or punch-through, background. Figure 5.19 shows an estimate of 10:1 for decay muon to hadron
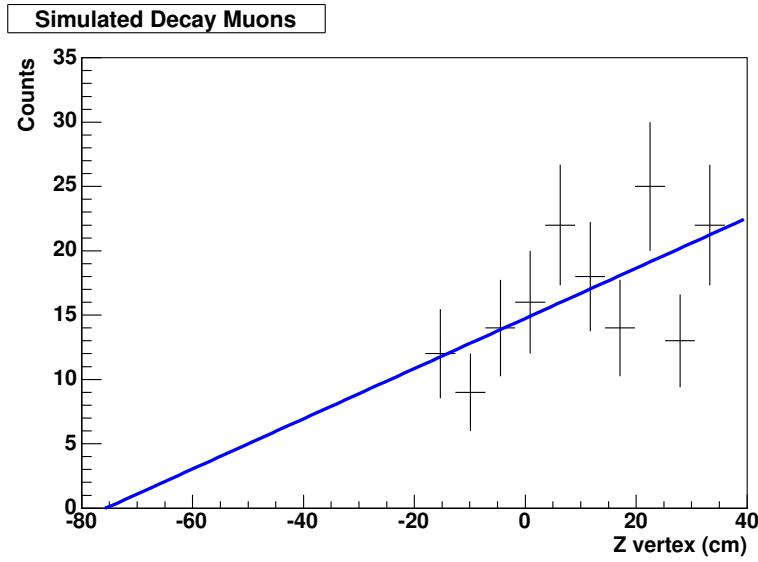
Figure 5.30: Simulated decay muon vertex distribution. The graph is for deep muons with $1 < p_T < 3$ and same η selection as for data.

punch-through at Gap 4. The non-muon vertex distribution for gaps 3 and 4, shown in Figure 5.31, is consistent with the expected flat distribution within the large statistical error bars.

Future simulations can be strengthened by more detailed study of hadronic interactions by additional FLUKA [70] tuning in conjunction alternate packages such as the GEISHA package within GEANT. Also, embedding to examine the occupancy effects will enhance the understanding of central collisions. Specialized software will significantly reduce the computing power needed for this type of simulation. A framework which allows successive cloning after absorber layers is in the late stages of testing and development. This method of cloning enriches the sample of simulated punc-through events and reduces the overhead associated with events without punch-through.

Simulated non-muon tracks
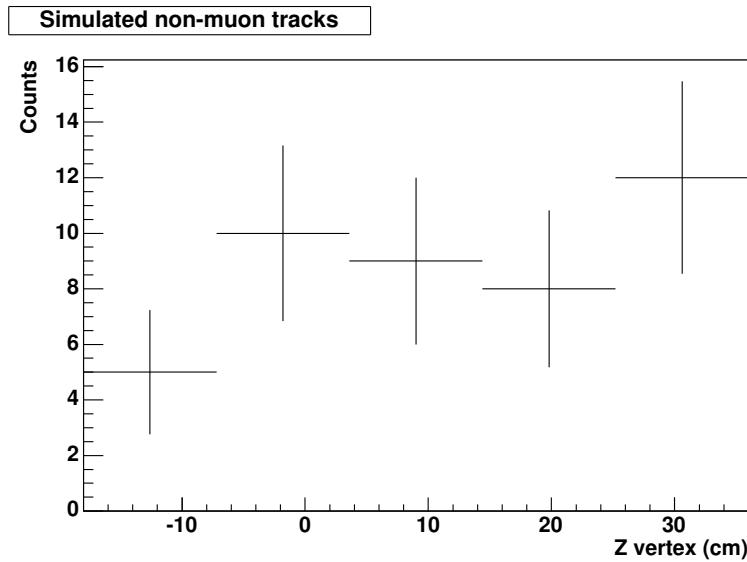
Figure 5.31: Simulated hadron background vertex distribution. The graph is for gaps 3 and 4 with $1 < p_T < 3$ and same η selection as for data.

5.9 Quality Selection Cuts

In order to enrich the signal to background ratio, quality cuts are made on various properties of the reconstructed particles. This section describes these parameters and states their accepted ranges. Some specific improvements made by these cuts are also discussed.

5.9.1 Pseudo-rapidity

In order to insure that detector acceptance does not become entangled with the vertex distribution expected from hadron decays, only a swath of pseudo-rapidity which is reconstructed as well for events at $z = -20$ as those at $z = 38$. A cut of $155^o < \theta < 161^o$, or $-1.8 < \eta < -1.5$, is currently used. Figure 5.32 shows the variation of η acceptance as a function of the event vertex.

126
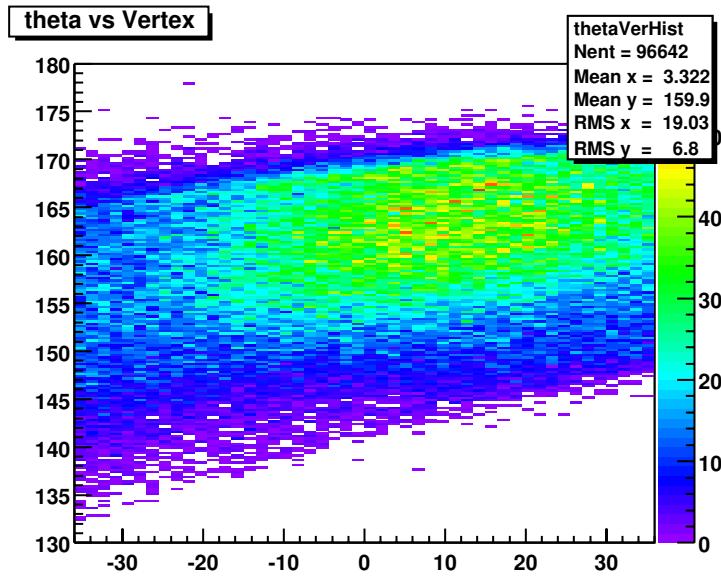
Figure 5.32: Two dimensional distribution of θ and z vertex. The distribution demonstrates the change in detector acceptance as a function of z. The region of $155 < \theta < 161$ is used in this analysis.

5.9.2 Azimuth

In order to reduce the effects of the incomplete tunnel shielding for the MuID, as discussed in Chapter 4, particles which project into the unshielded section of the MuID, the upper small panel and adjacent regions, are rejected from this analysis. Figure 5.33 shows the distribution of the cut variable before any other quality cuts are applied. The enhancement due to particles entering the detector via the MuID square hole is clearly visible in the upper wedge of the detector, Figure 5.11. Only particles with $abs(\phi) > 45^O$ for the Station III momentum vector are used.

5.9.3 MuID Depth

In order to minimize the hadron background and simplify reconstruction efficiencies, only particles which appear to fully penetrate the detector, last gap = 4, are used in the

127
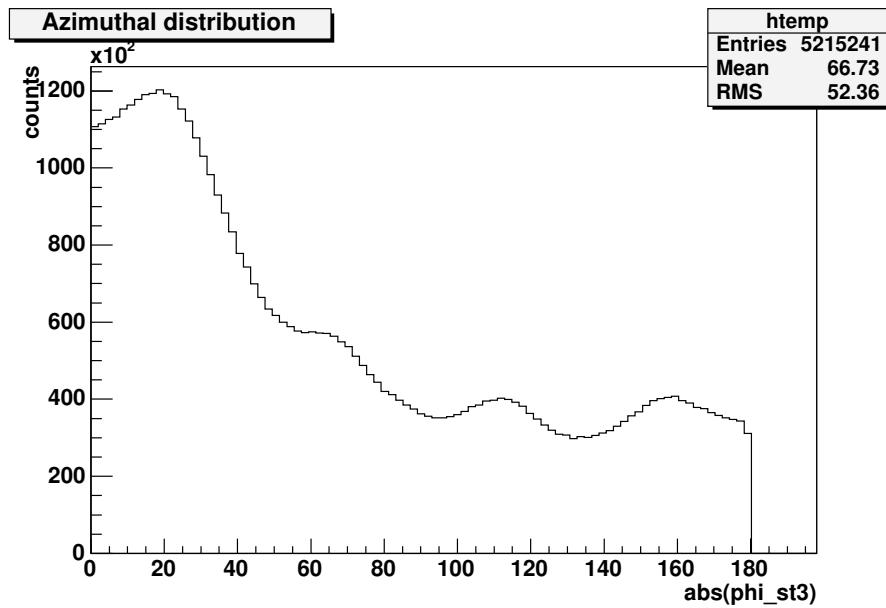
Figure 5.33: Azimuthal distribution of the Station III momentum vector before quality cuts. The enhancement below 45° is due to the lack of shielding in the ceiling of the MuID square hole, so this region is excluded from this analysis.

direct measure of prompt muons.

5.9.4 Fit Quality

The fit quality of each track is summarized in the reduced χ^2 quantity. All of a track's residuals are normalized by the resolution of the detector at the hit position. These unitless quantities are then summed and the total is normalized by the number of statistical degrees of freedom. The distribution of χ^2 variable is shown in Figure 5.34, and only particles with $\chi^2 < 7$ are used for this analysis.

5.9.5 Number of MuTr Hit Planes

A track may be constructed using hits from as few as 10 cathode planes and as many as 16. The raw MuTR hit plane distribution is actually very concentrated toward 10 in
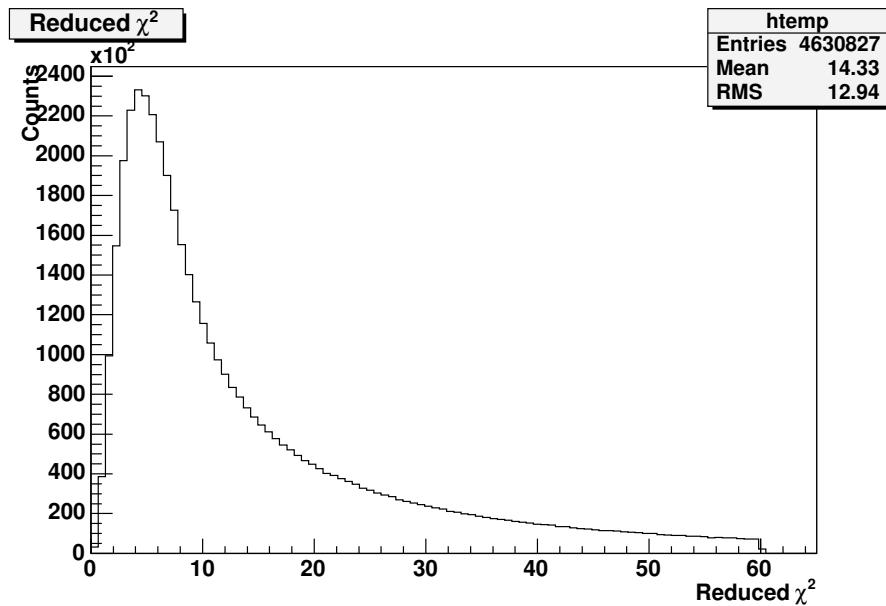
Figure 5.34: Track reduced χ^2 distribution without before quality cuts. Only particles with $\chi^2 < 7$ are used for this analysis.

Run II Au+Au data. Only particles with 12 or more MuTR hit planes are used in this analysis in order to help insure high quality tracks.

5.9.6 Longitudinal Momentum

As discussed earlier, p_Z is useful in separating muons from hardons and other non-muon background for particles which stop in gap 2 and 3. Although this cannot be done for Gap 4 particles, a minimum cut on p_z measured at Station III of 0.9 GeV/c can be used to reduce the number of falsely extended roads. As seen in Figure 5.21 nothing below this momentum should penetrate to Gap 4.

5.9.7 Gap 3 Signal-to-Background Enhancement

The improvement provided by these quality cuts is evident in the longitudinal momentum distributions. In Figures 5.35, before cuts, and 5.36, after cuts, the change made by
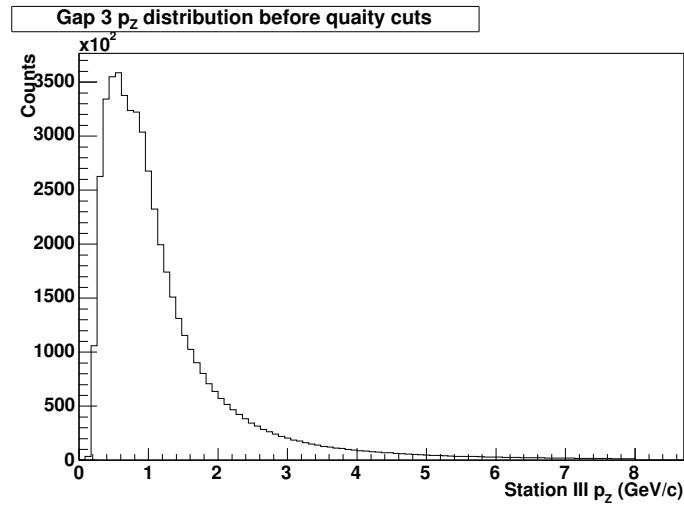
Figure 5.35: Longitudinal momentum distribution for shallow, Gap 3, muon candidates for Run II Au+Au data before quality cuts. The distribution is fairly smooth and continuous with no peak/tail division.
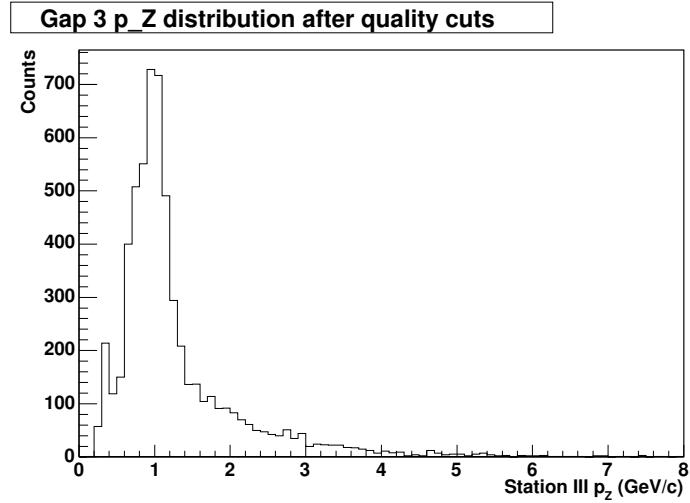
Figure 5.36: Longitudinal momentum distribution for shallow, Gap 3, muon candidates for Run II Au+Au data after quality cuts. This distribution does not include the 20% most central collisions. The muon stopping peak at around 1 GeV/c is now clearly visible. The distribution is now comparable to the simulated distribution in Figure 5.18. The small peak around 300 MeV/c shows that roads can be falsely extended by mis-associated hits.

130

the quality cuts is drastic. The distribution is much more comparable to the simulations after the quality cuts are applied.

5.10 Yields

5.10.1 Background Subtraction

The formula used for signal extraction is derived below. The yield distribution, $\rho(z)$, is the linear fit to the vertex distributions seen in Figure 5.37. The total number of reconstructed particles, or muon candidates, per event is given by $n_{\tilde{\mu}} = \frac{\text{Reconstructed Particles}}{\text{Events}}$ where reconstructed includes only particles which pass all quality cuts. This yield is found from the yield distribution by $n_{\tilde{\mu}} = \frac{1}{z_2 - z_1} \int_{z_1}^{z_2} \rho(z) dz$. For a linear distribution, $\rho(z) = mz + b$, the yield over a range is given by $\rho(z)$ evaluated at the midpoint, or $n_{\tilde{\mu}} = \rho(\frac{z_1 + z_2}{2}) \equiv \rho(z_m)$. Since only the decay component has a vertex dependence, the non-decay component is given by $\rho(z_0) = \rho_{\mu} + \rho_{non-\mu} = n_{\mu} + n_{non-\mu}$. The z_0 is the extrapolated Z value where the decay contribution ends. The average punch-through to decay fraction, $n_{non-\mu}/n_{decay} \equiv P_f$, is estimated from simulations. This analysis uses the average P_f value over all studied p_T, but it should be noted that P_f has a strong p_T dependence. The number of decay muons can be written as $n_{decay} = \rho(z_m) - \rho(z_0)$ and $n_{\mu} = \rho(z_0) - n_{non-\mu}$ or substituting from above:

$$n_{\mu} = \rho(z_0) - P_f(\rho(z_m) - \rho(z_0)) \tag{5.3}$$

The value for $z_0 = -65\text{cm}\pm10\%$ is estimated from simulations and analytical calculations. The fraction of hadron punch-through is estimated using the simulated punch-through to decay muon ratio of 0.1. Due to uncertainties in the FLUKA hadronic software package, and GEISHA giving up to a factor of 2 larger punch-through yields in similar simulations [71][72], a value of 0.15 ± 0.05 for the punch-through to decay

131
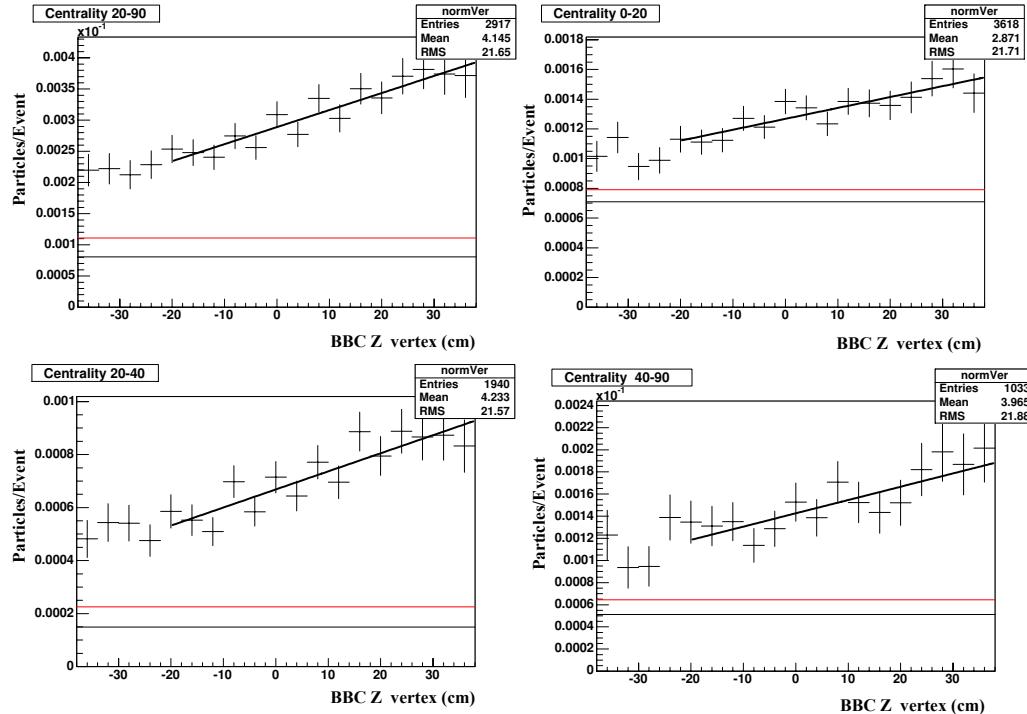
Figure 5.37: Muon candidate vertex distributions for various centrality classes. The area above the top (red) horizontal line represents the estimated contribution of muons from hadron decays. The area between the top (red) line and bottom (black) horizontal line represents the estimated contribution from non-μ punch-through. The data is over the p_T range from 1.2 to 2.5 GeV/c for $\mu = (\mu^+ + \mu^-)/2$

Table 5.3: Uncorrected yields per Au+Au collision for muons from hadron decays, punch though from non-μ, and the remaining non-hadronic prompt μ. The data is over the p_T range from 1.2 to 2.5 GeV/c for $\mu = (\mu^+ + \mu^-)/2$.

Centrality	Raw prompt μ per Au+Au collision (10^{-6})	Raw decay μ (10^{-6})	Raw punch-through (10^{-6})
0-20	$710 \pm 120(stat)^{+61}_{-550}(sys)$	540	81
20-40	$150 \pm 87(stat) \pm 57(sys)$	500	76
40-90	$51 \pm 26(stat) \pm 10(sys)$	89	13
20-90	$81 \pm 31(stat) \pm 23(sys)$	200	30

fraction, P_f, is used for this analysis. The remaining vertex independent yield is made of prompt muons and combinatoric background, which is dominated by prompt muons except for the most central events. Lines are used to show regions representing the various contributions to the vertex distributions in Figure 5.37, and the measured raw counts per collision are summarized for each contribution in Table 5.3.

5.10.2 Overall Efficiency Correction

The efficiency of the South muon spectrometer during Run II Au+Au data collection is estimated for reconstruction of $\mu^{\pm}$ using a combination of single muon estimates from Run II $p + p$ and J/$\Psi \rightarrow \mu^+ + \mu^-$ centrality dependent efficiency estimates for Run II Au+Au. Run II $p + p$ immediately followed the Au+Au run and had very similar hardware conditions. Both of the estimates were made using detailed GEANT simulations followed by response and reconstruction software.

From $p + p$ estimates [72], the efficiency is parameterized as:

$$\epsilon = \epsilon_{acc} \cdot \epsilon_{user}$$

$$\epsilon_{\mu^+} = 0.506(1 - 114.4 \exp(-5.92 p_T))(1 + 0.00147) \cdot 0.74(1 - 0.00189z)$$

and

$$\epsilon_{\mu^-} = 0.5(1 - 531.3 \exp(-7.45 p_T))(1 + 0.00126) \cdot 0.74(1 - 0.000873z)$$

Table 5.4: Estimated single muon detection efficiency for various centralities.

Centrality	Efficiency	Sys. Error
0-20	0.13	30%
20-40	0.18	30%
40-90	0.26	20%
20-90	0.19	25%

for high p_T $\epsilon = 0.37$ is a reasonable estimate for the purposes of this study.

For the most peripheral Au+Au collisions the spectrometer is 3% efficient at reconstructing J/ψs, but 30.5% of the loss is due to the pair opening angle[6]. The efficiency for reconstructing a particle pair is roughly the square of the efficiency for reconstructing a single particle, $\epsilon_{pair} \approx \epsilon_{single}^2$. This gives an estimate of a roughly 0.31 for the efficiency in peripheral Au+Au. As described earlier, this analysis removes 25% of azimuthal acceptance to reduce the problems associated with poor shielding. These two estimates are then combined to give a single muon efficiency of 0.26. The single μ efficiencies estimated from J/ψ simulations shown in Figure 5.26 are used to estimate the centrality dependence. The efficiency is estimated to be fairly constant for centrality $> 40\%$. When the $20 - 40\%$ bin is combined with the peripheral bin, the efficiencies are weighted by the number of binary collisions. The efficiencies estimated from this calculation are summarized in Table 5.4

These efficiencies are used to extract the corrected muon yield per binary collision by $N_\mu^{NN} = \frac{n_\mu}{\epsilon N_{coll}}$ where ϵ is the overall efficiency for measuring a single muon in the acceptance and N_{coll} is the average number of binary collisions for the centrality class. The rapidity density for prompt muons over our kinematic range, summarized in Table 5.5 ,is calculated by $\frac{dN_\mu^{NN}}{dy}|_{y=-1.65}(1.2 < p_T < 2.5) = \frac{1}{N_{coll}}\frac{N_\mu}{\Delta y}$.

Table 5.5: Prompt muon rapidity density at $y = -1.65$ for $1.2 < p_T < 2.5$.

Centrality	N_{coll}	$\frac{dN_\mu^{NN}}{dy}\big|_{y=-1.65}(1.2 < p_T < 2.5)\ (10^{-6})$
0-20	779 ± 75	$23 \pm 3.9(stat)^{+7.6}_{-19}(sys)$
20-40	296 ± 31	$9.3 \pm 5.5(stat) \pm 4.6(sys)$
40-90	45 ± 7	$15 \pm 7.5(stat) \pm 4.7(sys)$
20-90	117 ± 13	$12 \pm 4.6(stat) \pm 4.8(sys)$

Table 5.6: $\frac{1}{2\pi p_T}\frac{d^2\sigma_\mu^{NN}}{dp_T dy}\big|_{y=-1.65}(1.2 < p_T < 2.5)$ for various centralities.

Centrality	$< p_T >$ (GeV/c)	$\frac{1}{2\pi p_T}\frac{d^2\sigma_\mu^{NN}}{dp_T dy}\big|_{y=-1.65}(10^{-5}\text{GeV}^{-2}c^3\text{mb})$
0-20	1.85	$6.5 \pm 1.1(stat) \pm^{+2.1}_{-5.4}(sys)$
20-40	1.85	$2.6 \pm 1.5(stat) \pm 1.3(sys)$
40-90	1.85	$4.1 \pm 2.1(stat) \pm 1.3(sys)$
20-90	1.85	$3.4 \pm 1.3(stat) \pm 1.3(sys)$

5.10.3 Extrapolation Over p_T

Ideally, this analysis would be binned in p_T to produce an invariant yield shape, but only one data point will be calculated for each centrality class since the current statistics do not allow a significant number of points.

The values for $\frac{1}{2\pi p_T}\frac{d^2\sigma_\mu^{NN}}{dp_T dy}\big|_{y=-1.65} = \frac{1}{2\pi<p_T>}\frac{\sigma_{pp}N_\mu^{NN}}{\Delta p_T \Delta y}$, where $\sigma_{pp} = 42$mb, $\Delta p_T = 1.3$ GeV/c, $\Delta y = 0.3$, and $< p_T >= 1.85$ from the center of the p_T range, are reported in Table 5.6. The effect of more accurately estimating the $< p_T >$ from different shapes is discussed in the following chapter.

To find the total rapidity density, an acceptance correction must be applied to correct for the detector's finite p_T range, or $\frac{dN_\mu^{NN}}{dy}\big|_{y=-1.65} = \frac{1}{\lambda}\frac{dN_\mu^{NN}}{dy}\big|_{y=-1.65}(1.2 < p_T < 2.5)$. The correction factor is given by $\lambda = \frac{\int_{1.2}^{2.5} f(p_T)dp_T}{\int_0^\infty f(p_T)dp_T}$ where $f(p_T) = \frac{d^2N_\mu^{NN}}{dydp_T}$.

Currently, no muon p_T spectra measurements have been reported for hadronic col-
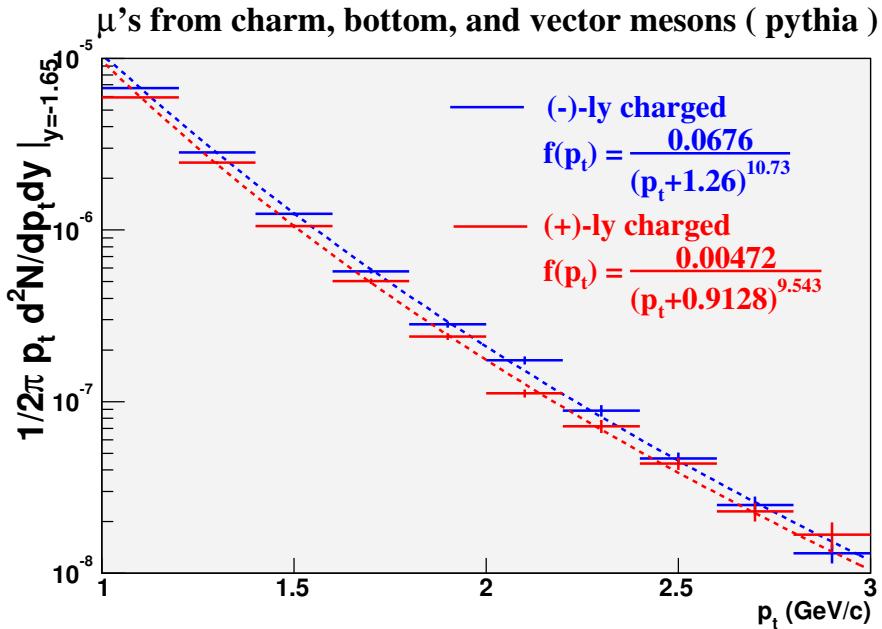
Figure 5.38: PYTHIA calculations for the p_T distribution of muons from charm, bottom, and vector mesons [72].

lisions at RHIC energies, but the analysis for $\sqrt{s_{NN}} = 200$ GeV $p + p$ collisions at PHENIX is at an advanced stage. This work in progress has been compared to PYTHIA simulations tuned from single electron data at mid-rapidity. The current PYTHIA estimate, shown in Figure 5.38, is softer and does not do a reasonable job reproducing the shape of the muon data. For electrons, the simulated spectrum allows an estimate of the fraction of the total yield which is within the p_T range of this alalysis. Using the fits from Figure 5.38, $f_{\mu^-}(p_T) = \frac{C_1 p_T}{(p_T+1.26)^{10.73}}$ and $f_{\mu^+}(p_T) = \frac{C_2 p_T}{(p_T+1.91)^{9.543}}$, gives $\lambda_{\mu^-} = 0.015$ and $\lambda_{\mu^+} = 0.009$ which are expected to be a significant understimate since the $p + p$ muon spectrum appears significantly harder and the fit is expected to overestimate the yield at low p_T. The electron analysis at mid-rapidity estimates that 12.58% of the total yield is within $0.8 < p_T < 4.0$ GeV/c [73]. Using a fit to the simulated electon spectra over this range, 3.5% of the total yield is estimated to be within $1.2 < p_T < 2.5$ GeV/c. This value will be used for discussion of the muon data in this analysis.

136

Table 5.7: The differential cross section for prompt muons at forward rapidity divided by the $c \to \mu$ branching ratio for various centrality classes.

Centrality	N_{coll}	$\frac{1}{B}\frac{d\sigma_\mu^{NN}}{dy}\|_{y=-1.65}(1.2 < p_T < 2.5)(\mu b)$
0-20	779 ± 75	$12 \pm 2.0(stat)^{+4.0}_{-9.8}(sys)$
20-40	296 ± 31	$4.7 \pm 2.7(stat) \pm 2.4(sys)$
40-90	45 ± 7	$7.3 \pm 3.8(stat) \pm 2.4(sys)$
20-90	117 ± 13	$6.1 \pm 2.3(stat) \pm 2.5(sys)$

5.10.4 Branching Fraction

The branching fractions for $D \to e + X$ for are much more accurately measured than $D \to \mu + X$. For most measurements the branching fractions are indistinguishable within errors, but branching fractions to muons appear systematically lower. One of the few statistically significant differences is $D^0 \to K^- e^+ \nu_e$ $(3.64 \pm 0.18)\%$ and $D^0 \to K^- \mu^+ \nu_\mu$ $(3.22 \pm 0.17)\%$ giving $\frac{\Gamma(K^-\mu^+\nu_\mu)}{\Gamma(K^-e^+\nu_e)} = 0.885 \pm 0.064$. Also, the fraction $\frac{\Gamma(c \to e^+ anything)}{\Gamma(c \to anything)} = 0.103 \pm 0.009^{+0.009}_{-0.008}$ and $\frac{\Gamma(c \to \mu^+ anything)}{\Gamma(c \to anything)} = 0.090 \pm 0.007^{+0.007}_{-0.006}$ giving $\frac{\Gamma(c \to \mu^+ anything)}{\Gamma(c \to e^+ anything)} = 0.874 \pm 0.102$ for an unknown mixture of charmed particles [74]. Making the assumption that $\frac{\Gamma(D \to \mu^\pm + X)}{\Gamma(D \to e^\pm + X)} \approx 0.88$, electron branching fraction measurements can be converted to muons. The ratios for the most abundant open charm mesons, and Λ_c, are estimated to be $D^+/D^0 = 0.45 \pm 0.05$, $D_s/D^0 = 0.25 \pm 0.05$, and $\Lambda_c/D^0 = 0.1 \pm 0.05$ from a combination of PYTHIA, CDF, STAR and particle data book values to give a $c \to e^+$ branching fraction of 0.095 ± 0.002 [73]. This branching fraction is scaled using the factor derived above, and this analysis assumes a branching fraction of $B = 0.084 \pm 10\%$ for $c \to \mu^+$. Using this effective branching ratio for $c \to \mu$, the $\frac{dN_c}{dy}$ over the examined 0.3 units of rapidity is:

$$\frac{d\sigma_{c\bar{c}}^{NN}}{dy}\Big|_{y=-1.65} = \sigma_{NN}\frac{dN_{c\bar{c}}^{NN}}{dy}\Big|_{y=-1.65} = \frac{\sigma_{NN}}{B}\frac{dN_\mu^{NN}}{dy}\Big|_{y=-1.65}$$

Due to the uncertainty in λ described in the previous section, only $\frac{1}{B}\frac{d\sigma_\mu^{NN}}{dy}\Big|_{y=-1.65}(1.2 < p_T < 2.5)(\mu b)$ is reported, Table 5.7.
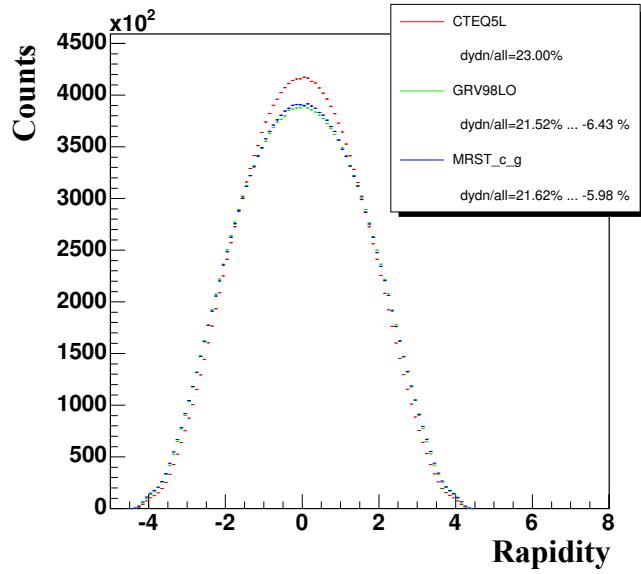
Figure 5.39: PYTHIA estimate for the rapidity distribution of charm.

5.10.5 Integration Over Rapidity

Tuned PYTHIA simulations were made for several parton distribution functions , Figure 5.39, to estimate the rapidity distribution of charm for $\sqrt{s_{NN}} = 200$ GeV $p + p$ collisions. Fitting the charm estimates using forward rapidity muon measurement, and central rapidity electron measuring, provides a measurement of the total charm cross section. Without an accurate extrapolation over all p_T, a reasonable error can not be estimated for a total cross section measurement. However the impact of data from this measurement on $\sigma_{c\bar{c}}$ under some assumptions will be discussed in the following chapter.

Chapter 6

Comparisons and Discussion

The preceding analysis has examined 5.3 million minimum bias Au+Au reactions at RHIC, at an energy of $\sqrt{s_{NN}} = 200$ GeV. Data from the forward spectrometer was used to study single muon production and its implications for charm production near rapidities of $y = -1.6$. The vertex dependent yield for muons from hadron decays was used to measure the decay component. Detailed simulations allowed estimates of non-muon punch-through as a fraction of the decay component. The punch through contamination was also reduced by studying only particles which appeared to penetrate the entire MuID. Subtracting decay and punch through components produced a net signal which should be dominated by single muons from semi-leptonic charm decays over the kinematic region studied, with the exception of high multiplicity events. PYTHIA spectra which gave good descriptions of prompt muons measured in $p + p$ collisions using a similar method were used to extrapolate the yields of this analysis over all p_T. An estimated effective branching ratio of $c \rightarrow \mu$ was used to relate the measurement to charm yield. This chapter will review several theoretical estimates for charm production at RHIC energies, as well as prior charm measurements at RHIC of relevance to this measurement. The prospects for future single muon measurements at PHENIX will also be discussed.

Table 6.1: Next to leading order (NLO) calculations for the total nucleon-nucleon charm pair production cross section at several energy regimes [75].

			40 GeV	200 GeV	5.5 TeV
PDF	m_c (GeV)	μ/m_c	$\sigma_{c\bar{c}}$ (μb)	$\sigma_{c\bar{c}}$ (μb)	$\sigma_{c\bar{c}}$ (mb)
MRST HO	1.4	1	37.8	298	3.18
MRST HO	1.2	2	44.0	382	5.83
CTEQ 5M	1.4	1	40.3	366	4.52
CTEQ 5M	1.2	2	44.5	445	7.39
GRV 98 HO	1.3	1	34.9	289	4.59

6.1 Theoretical Estimates

This section will review some of the theoretical estimates for total and open charm hadro-production at RHIC energies. The next to leading order (NLO) pQCD calculations have only claimed to be able to estimate the $Q\bar{Q}$ production cross sections to no better than 50 % for RHIC energies [75]. Various parton distribution functions (PDFs), scales (μ), and quark mass values produce NLO estimates, which do equally well at reproducing lower energy data, diverge significantly when extended to $\sqrt{s_{NN}}$ = 200 GeV as demonstrated in Figure 6.1. Predictions for the various assumptions at several energies (HERA-B, RHIC, and LHC) are summarized in Table 6.1.

The hadron-string dynamics (HSD) transport approach has been used to make detailed studies of charmomium disassociation and the inverse process of $D + \bar{D} \rightarrow$J/Ψ+ meson [76]. The study also provides estimates regarding open charm production, and this approach gives an estimate for the open charm meson rapidity distribution which is significantly different than those predicted by PYTHIA. The distribution for $\sqrt{s_{NN}}$ = 200 GeV $p + p$ collisions, seen in Figure 6.2, is nearly flat over almost ±2 units of rapidity. The authors note that the total and differential cross sections for open charm mesons might need to be reduced once experimental constraints are available.

Nuclear and medium effects have been predicted to effect total charm production

140
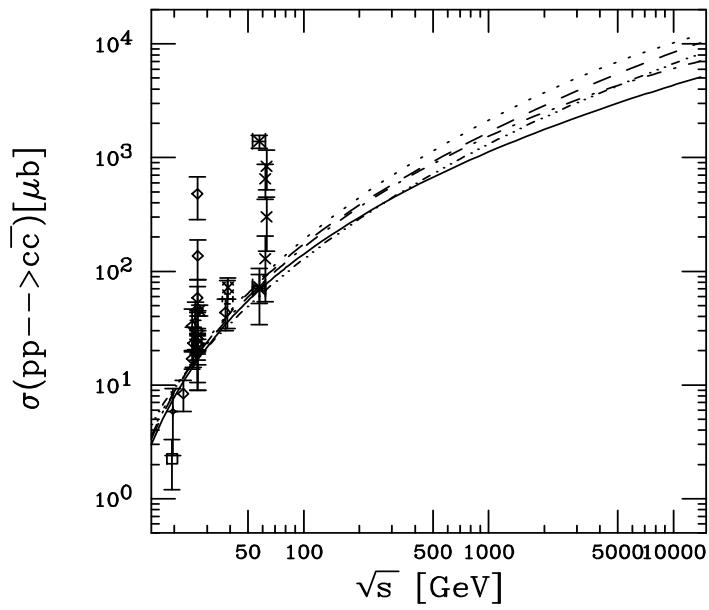
Figure 6.1: Fully NLO calculations of the total $c\bar{c}$ cross sections in $p + p$ interactions compared to data. The curves are: MRST HO (central gluon) with $\mu = m = 1.4$ GeV (solid) and $\mu = 2m = 2.4$ GeV (dashed); CTEQ 5M with $\mu = m = 1.4$ GeV (dot-dashed) and $\mu = 2m = 2.4$ GeV (dotted); and GRV 98 HO with $\mu = m = 1.3$ GeV (dot-dot-dot-dashed) [75].
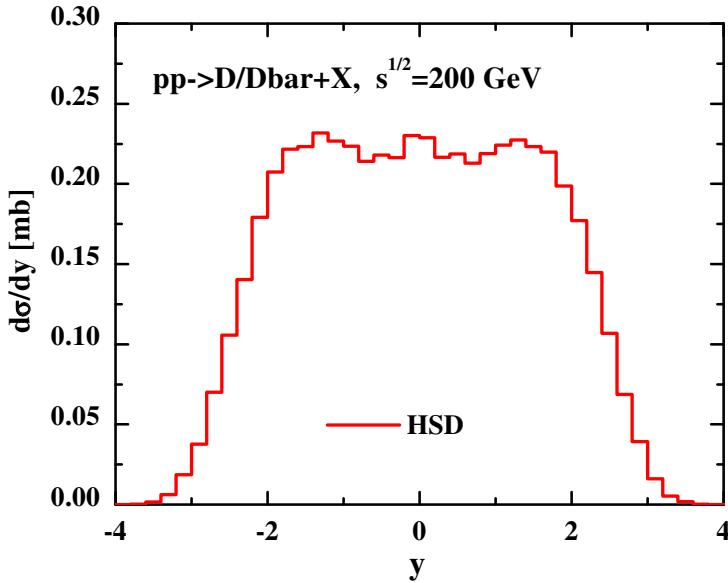
Figure 6.2: Open charm meson rapidity distribution from HSD calculations [76]. The distribution is significantly flatter than that predicted by PYTHIA.

in several ways. As discussed in Chapter 2, the creation of a QGP has been postulated to increase total charm production. Although the initial calculations of this possible effect are considered flawed, more recent estimates shown in Table 6.2 still support the possibility of significant charm production at RHIC due to the presence of a QGP, of up to 120 $c\bar{c}$ pairs, subsequent to the initial interaction in Au+Au collisions .

Also, the idea of a Color Glass Condensate (CGC) representing the initial conditions of nuclear collisions at RHIC has implications for charm production. Specifically, gluon saturation at low x would reduce charm production at forward rapidities relative to binary collision scaling. The ratio of forward rapidity charm to mid-rapidity charm would decrease with increasing centrality. An estimate of this effect is shown in Figure 6.3. Since charmed meson yields at $\eta = 2$ are expected to be suppressed by about a factor of two for even the most central collisions, the errors on current data do not allow a significant comparision, but future measurements should be able to test the prediction directly.

Table 6.2: The number of charm pairs estimated to be created "in-plasma" for central Au+Au interactions at RHIC [77]. Results assuming the scale factor $k = 1$ are shown in parenthesis. Other results are for $k = 2$. "This work" refers to reference [77].

| | QGP | $m_c = 1.2$ GeV | | $m_c = 1.5$ GeV | |
		$\alpha_s(M^2)$	$\alpha_s(T)$	$\alpha_s(M^2)$	$\alpha_s(T)$
	Levai *el al.*	$- -$	$- \ (3.7)$	$- -$	$- \ (1.1)$
$N_{QGP}^{c\bar{c}}$	Rafelski *el al.*	$- -$	$- -$	$- \ (15)$	$- -$
	Müller *el al.*	$- -$	$- -$	$17 \ -$	$- -$
	This work	$120 \ (60)$	$39 \ (19.5)$	$22 \ (11)$	$7.6 \ (3.8)$
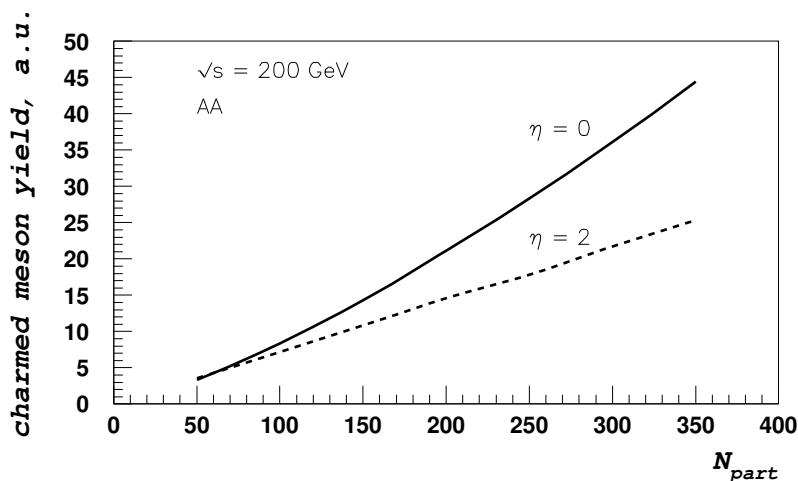
Figure 6.3: An estimate of centrality dependence for central and forward production of charmed mesons derived from a Color Glass Condensate framework [78]. The yields are given in arbitrary units (a.u.).

143

6.2 Previous Measurements at RHIC

The PHENIX spectrometers located at mid-rapididty have been used to measure charm via single electron yields for various systems. Prompt electron yields from PHENIX have only been published for $\sqrt{s_{NN}}$ = 130 GeV Au+Au [79], but preliminary data is available from $p + p$, d+Au, and Au+Au collisions at $\sqrt{s_{NN}}$ = 200 GeV. Results from the Au+Au analysis have been submitted for publication [24]. Data for backgrounds from Dalitz decays ($\pi^0, \eta, \eta', \omega, \phi$), dielectron decays ($\rho, \omega, \phi$), photon conversions, and kaon decays ($K^{0,\pm} \rightarrow \pi e v$) are subtracted to provide a non-photonic electron yield dominated by semi-leptonic decays of charm. Bottom decays also contribute to the non-photonic yield, but not at a significant level for the measured p_T range. These backgrounds are estimated using detailed GEANT simulations. Also, a thin piece of converter material is added around the beam pipe for a period of data collection to help estimate photon conversions and Dalitz decays of light neutral mesons. Other sources of background such as J/ψ and Drell-Yan are estimated to be negligible. The non-photonic electron p_T spectrum for $p + p$ collisions shown in Figure 6.4 also shows the charm and bottom contributions from a tuned PYTHIA simulation. The PYTHIA spectra demonstrate the insensitivity to bottom decays with current statistics. Data from this analysis is compared to the PHENIX electron measurement at mid-rapidity in Figure 6.5. Using the poor assumption that $< p_T >= \frac{\int p_T \frac{dN}{dp_T dy} dp_T}{\int \frac{dN}{dp_T dy} dp_T}$ = 1.85 GeV/c, the equivalent of assuming a flat $\frac{dN}{dy dp_T}$ distribution, gives a point for the muon data consistent with the electron spectra and significantly above the PYTHIA curve. More reasonable estimates for $< p_T >$ from the measured electron shape, 1.64 GeV/c, and from the PYTHIA muon spectra, 1.50 GeV/c, give points consistent with the PYTHIA shape.

144
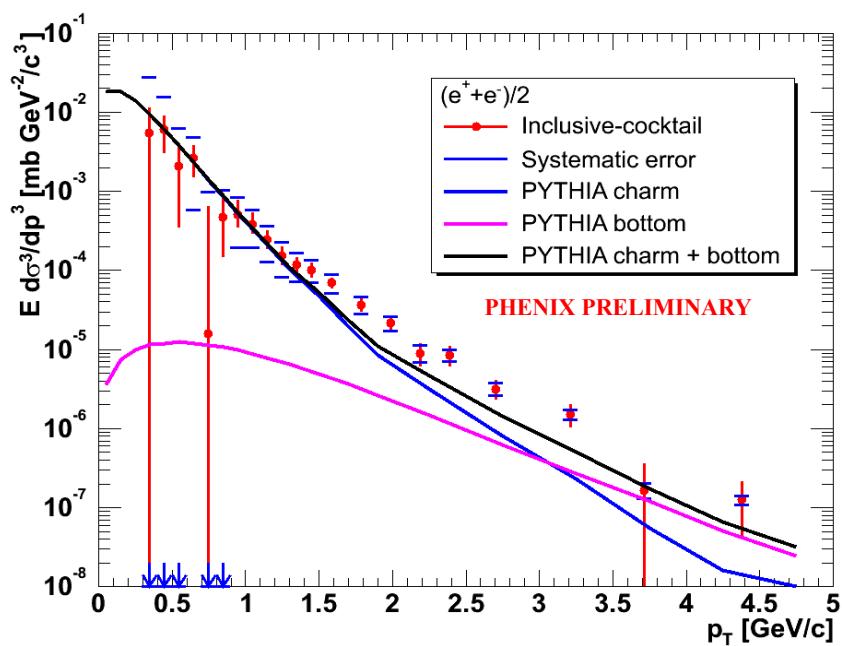
Figure 6.4: PHENIX preliminary p_T spectra from single electrons for $\sqrt{s_{NN}} = 200\,\text{GeV}$ $p + p$ collisions [80]. The lower (middle) curve show the bottom (charm) contribtion. The top curve shows the sum of charm and bottom.
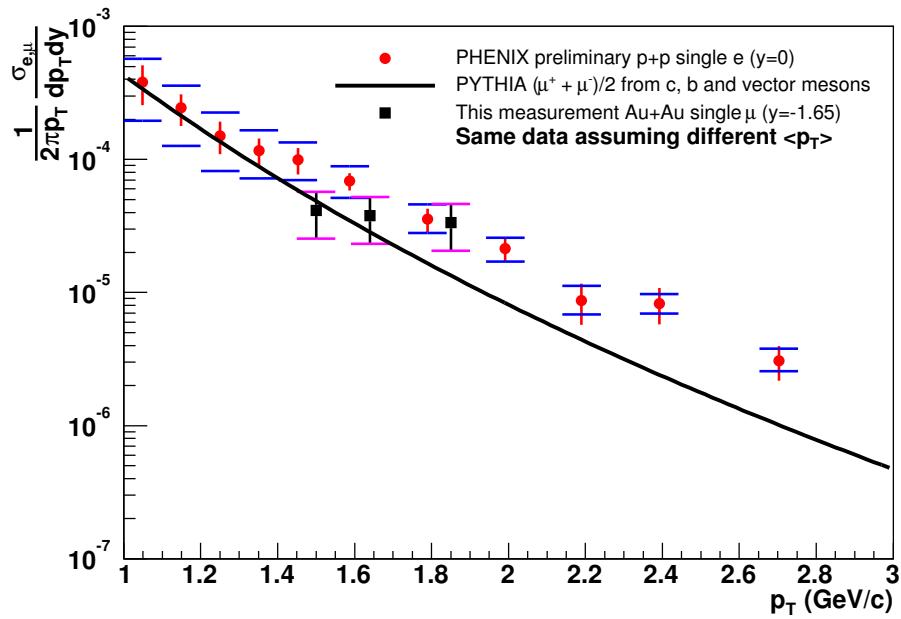
Figure 6.5: PHENIX heavy-flavor electron p_T spectra for $\sqrt{s_{NN}} = 200$ GeV $p + p$ collisions compared to single μ data for the 20-90% centrality class from this work. The μ points represent the same data assuming different values for $< p_T >$. The values are average of the extrema of the data's p_T coverage (1.85 GeV/c), the $< p_T >$ from the mid-rapidity electron spectra from PYTHIA (1.64 GeV/c), and the $< p_T >$ from the forward rapidity muon spectra from PYTHIA (1.5 GeV/c). The electron data was extracted graphically from Figure 6.4

Table 6.3: STAR collaboration measurements of dN/dy of D^0 in $\sqrt{s_{NN}}$ = 200 GeV d+Au collisions, and the corresponding estimates for $d\sigma/dy$ for $c\bar{c}$ pairs per nucleon-nucleon collision and the total charm pair production cross section [81].

	$dN(D^0)/dy\|_{y=0}(10^{-2})$	$d\sigma_{c\bar{c}}^{NN}/dy\|_{y=0}$ (mb)	$\sigma_{c\bar{c}}^{NN}$ (mb)
D^0	$2.8 \pm 0.4 \pm 0.8$	$0.29 \pm 0.04 \pm 0.08$	$1.3 \pm 0.2 \pm 0.4$
$D^0 + e^{\pm}$	$2.9 \pm 0.4 \pm 0.8$	$0.30 \pm 0.04 \pm 0.09$	$1.4 \pm 0.2 \pm 0.4$

Figure 6.6 shows the non-photonic electron p_T spectrum for various centrality classes of $\sqrt{s_{NN}}$ = 200 GeV Au+Au events. The best $p + p$ fit is consistent with the Au+Au data for all centralities. At $\sqrt{s_{NN}}$ = 130 GeV and 200 GeV, Figure 6.7, the non-photonic electron yield, and therefore the charm yield per binary collision shows no centrality dependence within experimental errors. The centrality dependence for prompt muons from this analysis, shown in Figure 6.8, also shows no centrality dependence within errors. The charm yield from non-photonic electrons is also found to be consistent with binary collision scaling of the $p + p$ data for all centralities.

The STAR experiment at RHIC has also demonstrated the ability to perform open charm measurements. STAR has directly reconstructed $D^0(\bar{D}^0) \rightarrow K^{\mp}\pi^{\pm}$ at mid-rapidity in $\sqrt{s_{NN}}$ = 200 GeV d+Au collisions (Figure 6.9). Additionally, single electron measurements were used to study charm in $p + p$ and d+Au at 200 GeV. The reconstructed D and electron p_T distributions are shown in Figure 6.10. Extending the mid-rapidity measurement over all rapidity, STAR finds a total cross section of $\sigma_{c\bar{c}}^{NN}$ = $1.4 \pm 0.3 \pm 0.3$ mb in d+Au collisions from the combined electron and D data. The value of this measurement is larger than the current PHENIX measurements [24][82] discussed in the following section, but the errors are too large to claim a statistically significant difference. The STAR measurement is significantly above NLO and PYTHIA calculations shown in Figure 6.11. The STAR measurements are summarized in Table 6.3.
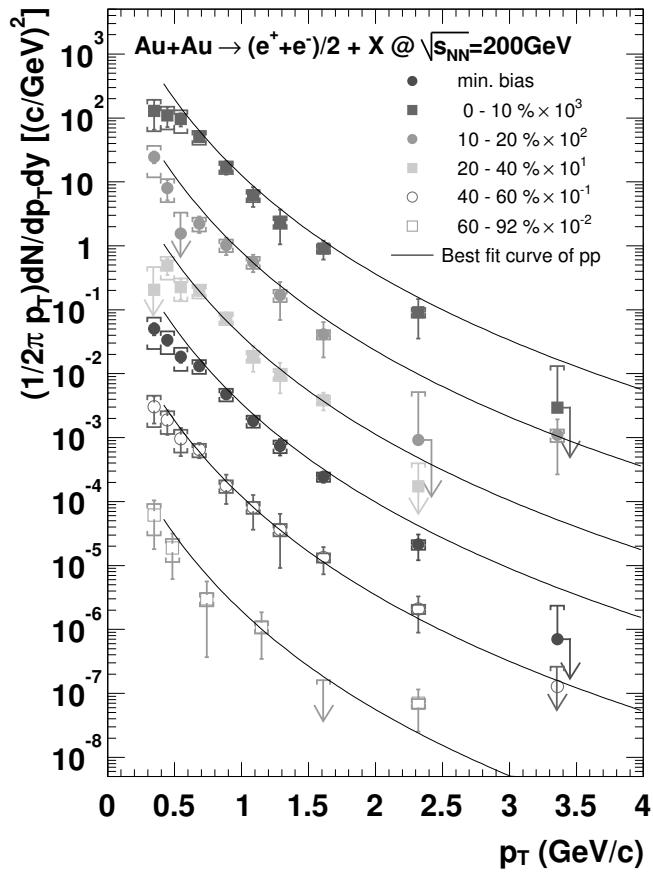
Figure 6.6: PHENIX heavy-flavor electron p_T spectra for various centrality classes of $\sqrt{s_{NN}}$ = 200 GeV Au+Au collisions. Systematic errors are indicated by brackets, and statistical errors are shown by bars. The curve shows the best fit of the $p + p$ measurement scaled by the number of binary collisions [24].
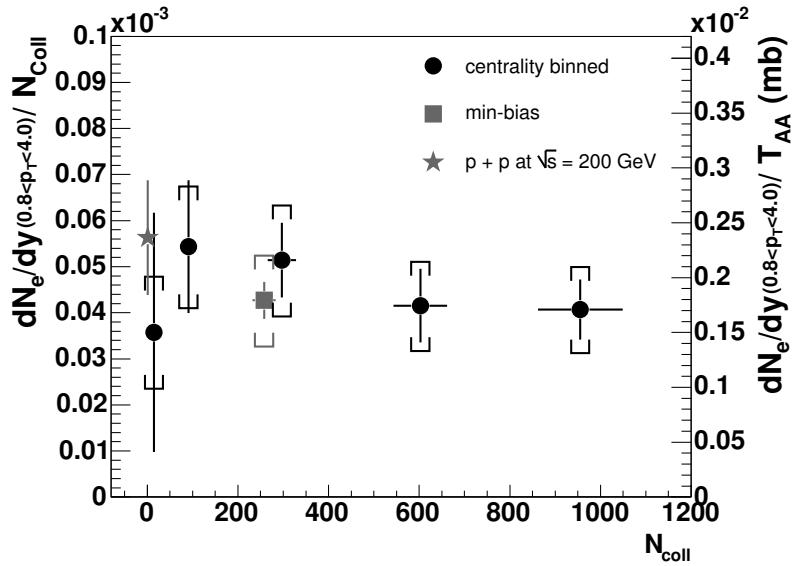
Figure 6.7: The PHENIX non-photonic electron yield per binary collision ($0.8 < p_T <$ 4.0 GeV/c) measured in Au+Au reactions at $\sqrt{s_{NN}} = 200$ GeV as a function of centrality. The yield in $p + p$ collisions at 200 GeV is also shown [24].
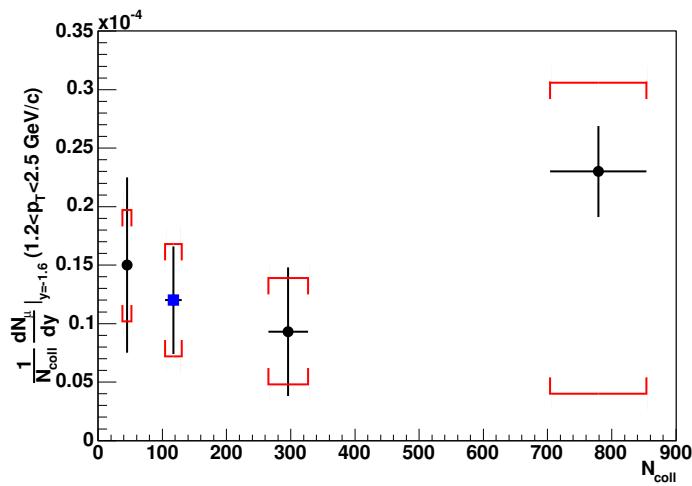
Figure 6.8: The prompt muon yield per binary collision ($1.2 < p_T < 2.5$ GeV/c) measured in Au+Au reactions at $\sqrt{s_{NN}} = 200$ GeV as a function of centrality. The closed circle markers represent exclusive centality bins, and the square marker represents 20-90% centrality.

149
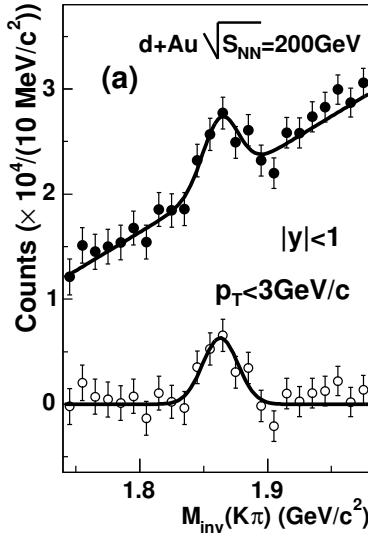
Figure 6.9: The invariant mass distributions of kaon-pion pairs from d+Au collisions measured by STAR [81]. The solid circles show the signal after mixed-event background subtraction, and the open circles show the signal after an additional subtraction using a linear parametrization.
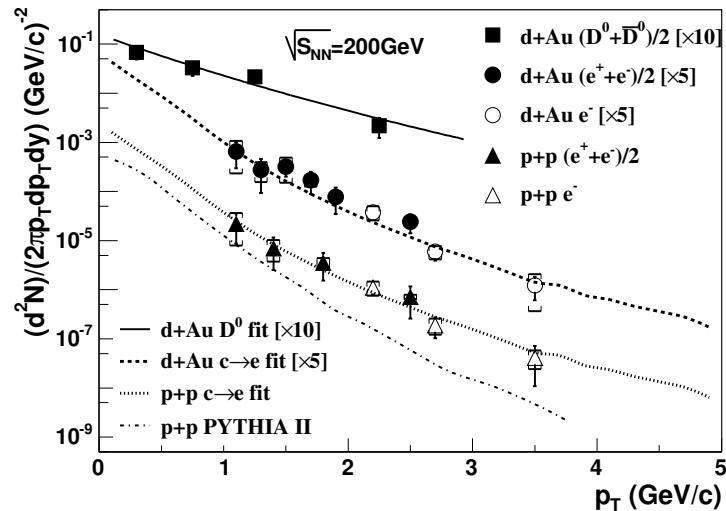
Figure 6.10: STAR measurement of reconstructed D^0 and non-photonic electron p_T distributions for $\sqrt{s_{NN}} = 200$ GeV d+Au and $p + p$ collisions [81].
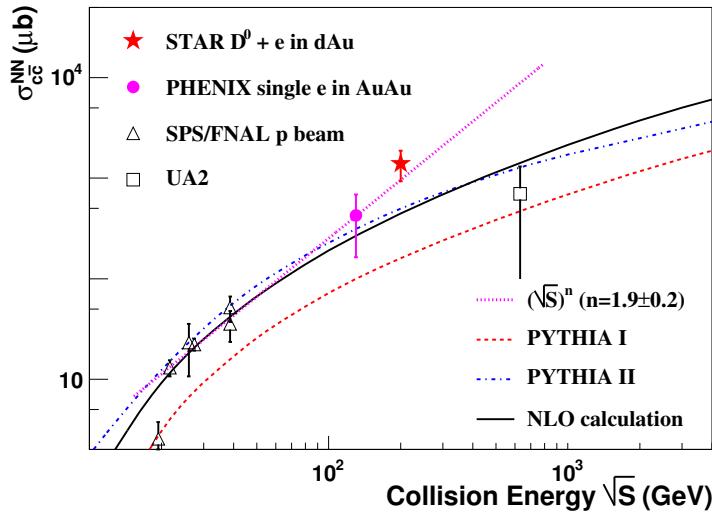
Figure 6.11: The collision energy dependence of the total $c\bar{c}$ cross section per nucleon-nucleon. The dashed line is a PYTHIA calculation from [81] and the solid line is a NLO pQCD calculation [75].

6.3 Total $c\bar{c}$ Cross Section

The total charm cross sections for $\sqrt{s_{NN}}$ = 200 GeV collisions is found to be $\sigma_{c\bar{c}}^{NN}$ = $611 \pm 56_{stat} \pm 157_{sys}$ μb for Au+Au [24] and $\sigma_{c\bar{c}}$ = $709 \pm 85_{stat} \pm {}^{332}_{281}{}_{sys}$ μ b for $p + p$ (preliminary)[82] from measurments of prompt electrons at mid-rapidity which are extended over all p_T and raidity based on simulated distributions. These measurements depend on model estimations, such as PYTHIA, for the rapidity dependence and p_T extrapolation. The measurements of this work can extend the experimental range to forward rapidity, with currently large errors. Here the total cross section is reported based on PHENIX measurements at mid-rapidity, and the importance of a forward rapidity measurement is discussed. Figures 6.12 and 6.13 show the central rapidity measurement and the forward rapidity measurement of this work for the 20-90% centrality class, assuming the p_T correction factor λ = 3.5% from the PHENIX electron shape, with several calculated shapes for charm rapidity dependence. In Figure 6.12 the

151
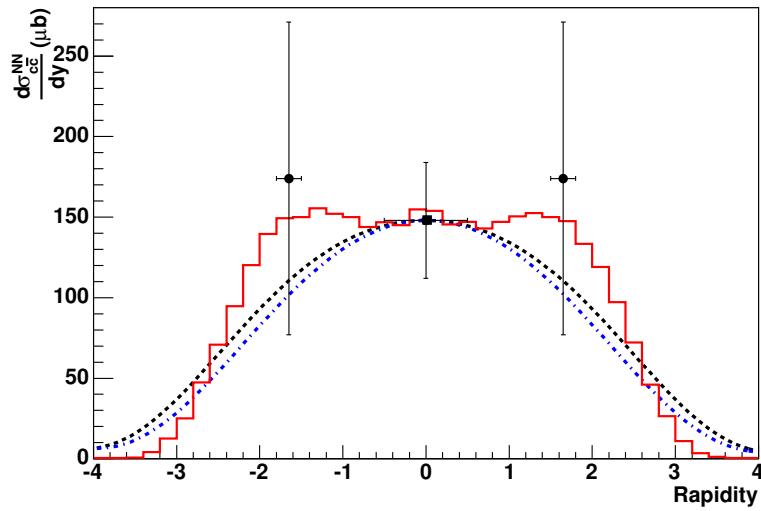
Figure 6.12: Charm rapidity dependence with shapes normalized to the PHENIX mid-rapidity measurement for $\sqrt{s_{NN}} = 200$ GeV Au+Au. The point at $y = -1.65$ and its reflection about $y = 0$ are from the 20-90% centrality bin of this work, assuming an example p_T correction factor of $\lambda = 3.5$%. The solid line is the shape from the HSD calculation for charmed mesons [76]. The dash-dotted (dashed) curve is a PYTHIA calculation for charm rapidity using the CTEQ5L (MRST_c_g) parton distribution functions [73].
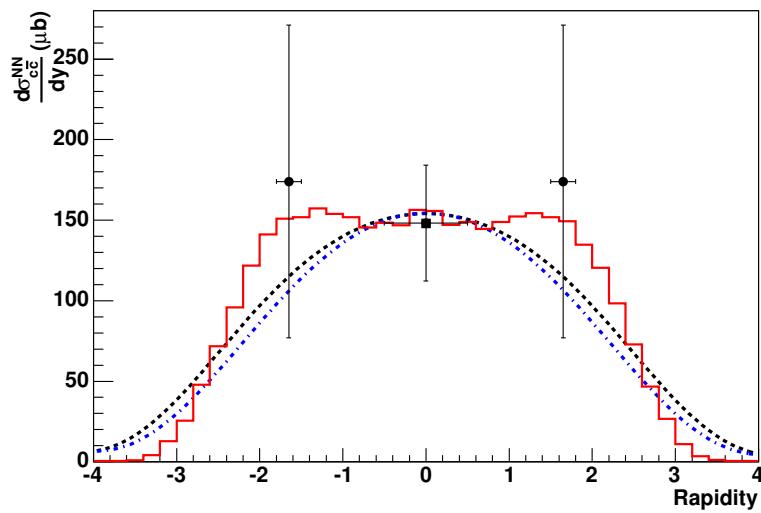
Figure 6.13: Charm rapidity dependence with shapes normalized to the PHENIX mid-rapidity measurement and the forward rapidity measurement from this work for $\sqrt{s_{NN}} = 200$ GeV Au+Au. The point at $y = -1.65$ and its reflection about $y = 0$ are from the 20-90% centrality bin of this work, assuming a example p_T correction factor of $\lambda = 3.5\%$. The solid line is the shape from the HSD calculation for charmed mesons [76]. The dash-dotted (dashed) curve is a PYTHIA calculation for charm rapidity using the CTEQ5L (MRST_c_g) parton distribution functions [73].
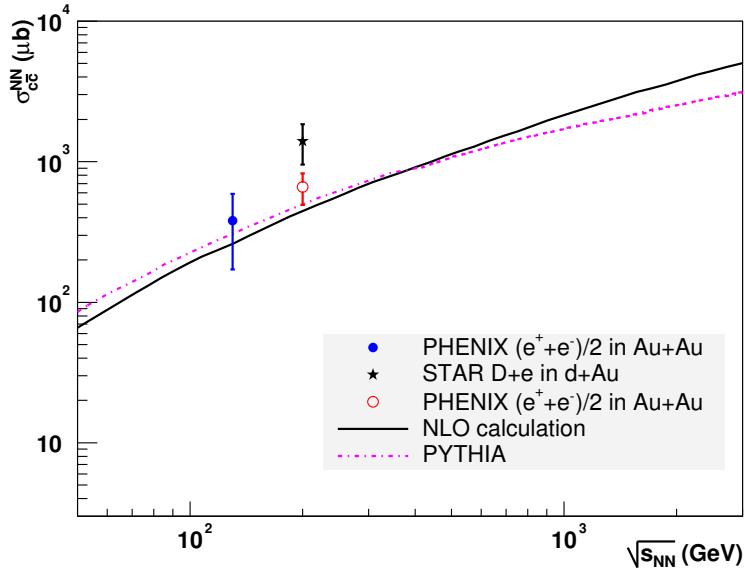
Figure 6.14: Total charm production measurements from RHIC experiments compared to PYTHIA and NLO calculations. The dash-dot line is a PYTHIA calculation from [81] and the solid line is a NLO pQCD calculation [75].

shape heights are only determined from the $y = 0$ electron data point. Figure 6.13 uses both the $y = 0$ electron and $y = -1.6$ muon points to fit the shape heights. Under the assumption of $\lambda = 3.5\%$, which is used only for instructive purposes, the forward data with significantly large error bars do not significantly influence the fit. The fits to these rapidity distributions allow for estimates of the total charm production cross section. The total charm production cross section measurements which have been reported by RHIC experiments are shown in Figure 6.14. The STAR measurement from d+Au is inconsistent with the shown calculations and is greater than the PHENIX measurement from Au+Au at the same energy. All of the measurements in Figure 6.14 are based on mid-rapidity data.
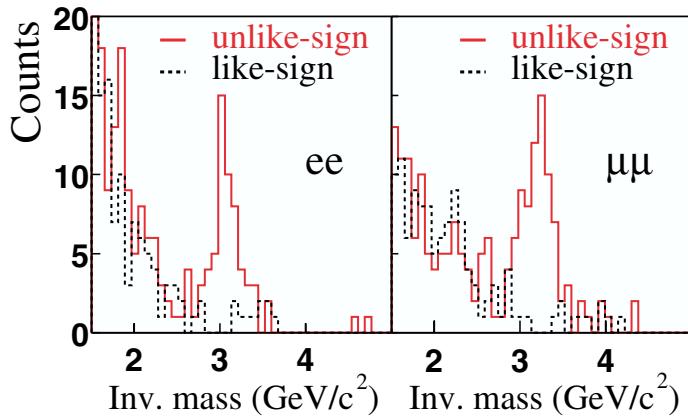
Figure 6.15: The PHENIX invariant mass spectra for dielectron and dimuon pairs [83]. The J/ψ is clearly visible in the unlike-sign distribution. Unlike-sign pairs (sum of like-sign pairs) are shown as solid (dashed) lines.

6.4 J/ψ Measuremets

As discussed in Chapter 2, one of the compelling reasons for measuring open charm production is to provide a reference for charmonium production. PHENIX has the ability to measure J/ψ at both forward and mid-rapidity. First results have been published for $p + p$ [83] and Au+Au [64]. No significant signal was observed in these low-statistics Au+Au runs, which was consistent with the expectation of binary collision scaling. Significant peaks have since been observed in the higher statistics Run IV Au+Au data set. The invariant mass distribution for dileptons in $\sqrt{s} = 200$ GeV $p + p$ collision, shown in Figure 6.15 represents the first J/ψ measurement at RHIC. The rapidity distribution of the differential cross section for $p + p$ data, including preliminary Run III data is shown in Figure 6.16, and the preliminary ratio of d+Au to $p + p$ differential cross sections is shown in Figure 6.17. The raw J/ψ yields from electrons and muon through Run IV are summarized in Table 6.4
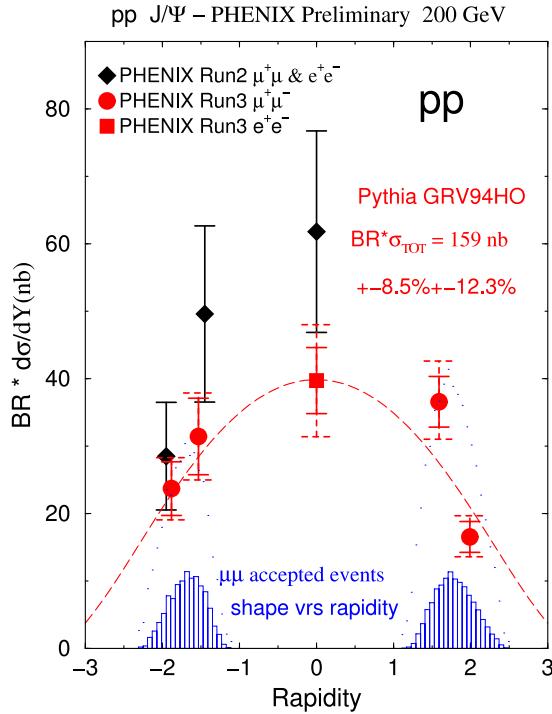
Figure 6.16: The rapidity dependence of the differential J/ψ production cross section as measured by the PHENIX experiment [84]. The preliminary Run III data demonstrate the significantly increased statistics.

Table 6.4: The history of raw J/ψ yields at PHENIX [84].

Year	Ions	$\sqrt{s}_{NN}$	Luminosity	Detectors	J/Ψ
2000	Au+Au	130GeV	1 μb^{-1}	Central (electrons)	0
2001	Au+Au	200GeV	24 μb^{-1}	Central	13[4] + 0
2002	p+p	200GeV	0.15 pb^{-1}	+ 1 muon arm	46 + 66[3]
2003	d+Au	200GeV	2.74 nb^{-1}	Central	300+800+600
2003	p+p	200GeV	0.35 pb^{-1}	+ 2 muon arms	100+300+120
2004	Au+Au	200GeV	240 mb^{-1}	Central +2muon arms	500+2×1000
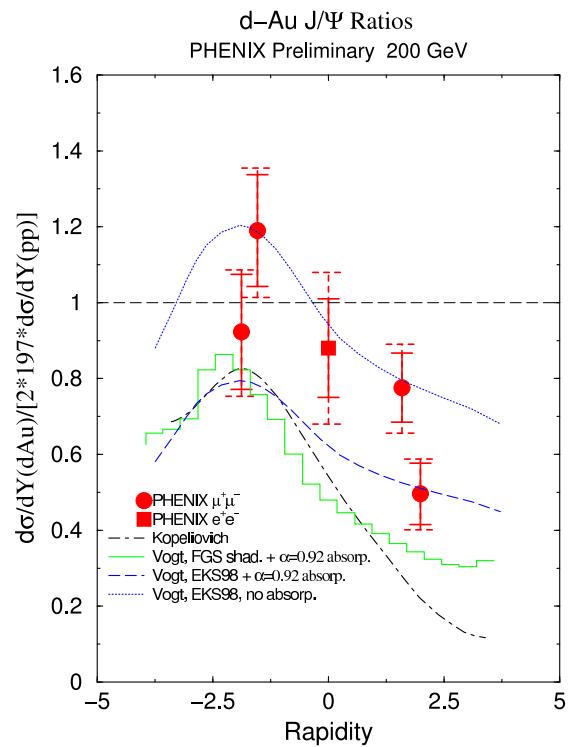
Figure 6.17: The ratio of the d+Au to $p + p$ differential cross section for the J/ψ compared to various calculations[84]. The data are compared to several shadowing estimates.

6.5 Outlook

The fit from the 20-90% centrality class, shown in Figure 5.37, is used to examine the effect of increased statistics. A histogram is randomly filled based on the vertex fit, and the same fit analysis used for measurements in this analysis is used to extract the statistical error. A factor of 100 increase in the muon candidate yield would allow for roughly a ±10% (stat) measurement for a 60-92%, N_{coll} = 14.5 ± 4, centrality class under the assumption of binary collision scaling. A factor of 500 increase in the muon candidate yield may allow roughly a 25% (stat) measurement for 60-92% centrality class for 2.25 < p_T < 2.5 GeV/c. This latter estimate is made under the assumption that the PYTHIA shape for mid-rapidity electrons is the same as forward muons over 1.2 < p_T < 2.5 GeV/c. More refined acceptance and efficiency corrections can increase statistics by reducing or removing the η cut and allowing measurements to $p_T \approx 1$ GeV/c. Statistics for future measurements will also be improved by the removal of an azimuthal cut due to better shielding, the availability of the north muon spectrometer, and improved hardware efficiencies. Over 1 billion minimum biased $\sqrt{s_{NN}}$ = 200 GeV Au+Au collisions were recorded during Run IV, and these should provide more than a factor of 500 increase in recorded muon candidates.

Chapter 7

Conclusions

The ability of the PHENIX detector to measure open charm in Au+Au collisions at RHIC provides crucial information for understanding the created medium. D meson ratios, flow, p_T spectra, total charm yield, and centrality dependence have all been proposed to be modified in a measurable way by the formation of a QGP. Open charm yields can also provide a critical baseline for charmonium measurements. Also the combination of rapidity and centrality dependence of charmed mesons has been proposed as an indicator of the Color Glass Condensate, which may describe the initial conditions of nuclear interactions at RHIC.

This thesis describes the first single muon measurements from Au+Au at RHIC energies in any kinematic region, and the results are the first with direct implications for open charm production from Au+Au collisions at RHIC energy at forward rapidity. This work finds no centrality dependence in the prompt muon yield scaled by the number of binary collisions within the large experimental errors. This observation is consistent with the higher statistics single electron measurement made by PHENIX at mid-rapidity. The yields and p_T spectra for the PHENIX single electron measurement for Au+Au are consistent with the yields from preliminary $p + p$ data scaled by the number of binary collisions. No single muon measurement for $\sqrt{s} = 200$ GeV $p + p$

159

is currently available for direct comparison comparison, but for reasonable estimates of $< p_T >$ the data point from this analysis is below the single electron p_T curve and is consistent with the presented PYTHIA shape. The ratio of prompt muon yield per binary collision over the examined kinematic range for 0-20% to 90-20% appears to be inconsistent with predictions for "in-plasma" charm production which would result in more than a factor of ~6 charm enhancement from peripheral to central collisions. On a similar note, the errors bars for this analysis would not allow for observation of an enhancement factor on the scale of that observed by NA50. No statistically significant enhancement has been observed in the $\sqrt{s_{NN}}$ = 200 GeV Au+Au PHENIX single electron data.

This analysis has demonstrated how prompt single muon measurements at forward rapidity can extend charm measurements in PHENIX to reduce error on the total charm cross section via a more experimentally motivated shape. Single muon measurements will provide additional information to help resolve the possible discrepency between the charm measurments from PHENIX Au+Au and STAR d+Au data. The statistics and the current lack of a reliable factor for extrapolating over all p_T do not yet allow this ability to be utilized. The need for higher statistics data in order to study the intriguing topics related to the Quark Gluon Plasma and the Color Glass Condensate, such as gluon saturation and energy loss has been demonstrated.

The south forward spectrometer (MuTR+MuID) collected the data for this analysis during its commissioning run. This analysis has helped demonstrate the successful design and operation of the detector. Many challenges were present during the commissioning run, and in response many improvements have been made to the system as a whole. The ability of PHENIX to measure open charm and charmonium at forward and central rapidity has been successfully demonstrated, and the stage is set for many interesting measurements for years to come.

Bibliography

Bibliography

[1] Helmut Satz. Colour deconfinement in nuclear collisions. *Rept. Prog. Phys.*, 63:1511, 2000.

[2] Simon Hands. The phase diagram of QCD. *Contemp. Phys.*, 42:209–225, 2001.

[3] Jeremy J. Drake et al. Is RXJ1856.5-3754 a quark star? *Astrophys. J.*, 572:996–1001, 2002.

[4] K. Adcox et al. Formation of dense partonic matter in relativistic nucleus-nucleus collisions at RHIC: Experimental evaluation by the PHENIX collaboration.

[5] M. C. Abreu et al. Evidence for deconfinement of quarks and gluons from the J/ψ suppression pattern measured in Pb-Pb collisions at the CERN-SPS. *Phys. Lett.*, B477:28–36, 2000.

[6] R. J. Newby. *J/ψ Production in Au-Au Collisions at $\sqrt{s_{NN}}$ = 200 GeV*. Dissertation, University of Tennessee, 2003.

[7] S. S. Adler et al. Absence of suppression in particle production at large transverse momentum in $\sqrt{s_{NN}}$ = 200 GeV d+Au collisions. *Phys. Rev. Lett.*, 91:072303, 2003.

[8] J. Adams et al. Evidence from d+Au Measurements for Final-State Suppression of High-p_T Hadrons in Au+Au Collisions at RHIC. *Phys. Rev. Lett.*, 91:072304, 2003.

[9] Anne Mosher. The Strong Interactions: Proceedings of the 9th SLAC Summer Institute on Particle Physics (SSI 81), Stanford, Calif., 27 Jul - 7 Aug, 1981. SLAC-0245.

[10] J. J. Aubert et al. EXPERIMENTAL OBSERVATION OF A HEAVY PARTICLE J. *Phys. Rev. Lett.*, 33:1404–1406, 1974.

[11] J. E. Augustin et al. DISCOVERY OF A NARROW RESONANCE IN e+ e- ANNIHILATION. *Phys. Rev. Lett.*, 33:1406–1408, 1974.

[12] G. Goldhaber et al. Observation in e^+e^- Annihilation of a Narrow State at 1865 MeV/c^2 Decaying to $K\pi$ and $K\pi\pi\pi$. *Phys. Rev. Lett.*, 37:255259, 1979.

[13] I. Peruzzi et al. Observation of a Narrow Charged State at 1876 MeV/c^2 Decaying to an Exotic Combination of $K\pi\pi$. *Phys. Rev. Lett.*, 37:569571, 1979.

[14] G. Goldhaber et al. OBSERVATION IN e+ e- ANNIHILATION OF A NARROW STATE AT 1865-MeV/c**2 DECAYING TO Kπ AND K$\pi\pi$. *Phys. Rev. Lett.*, 37:255–259, 1976.

[15] I. Peruzzi et al. OBSERVATION OF A NARROW CHARGED STATE AT 1876-MeV/c**2 DECAYING TO AN EXOTIC COMBINATION OF K$\pi\pi$. *Phys. Rev. Lett.*, 37:569–571, 1976.

[16] J. L. Ritchie et al. FORWARD PRODUCTION OF CHARM STATES AND PROMPT SINGLE MUONS IN 350-GeV p Fe INTERACTIONS. *Phys. Lett.*, B126:499, 1983.

[17] H. Cobbaert et al. A-DEPENDENCE OF THE CHARM PRODUCTION CROSS-SECTION IN 320- GeV/c π^- INTERACTIONS. *Phys. Lett.*, B191:456, 1987.

[18] H. Cobbaert et al. A-DEPENDENCE OF THE CHARM PRODUCTION CROSS-SECTION IN 300- GeV/c PROTON INTERACTIONS. *Phys. Lett.*, B206:546, 1988.

[19] P. Sonderegger. Accurate measurements of dimuon production in the NA60 experiment. *J. Phys.*, G30:S1027–S1030, 2004.

[20] A. Baldit et al. Study of prompt dimuon and charm production with proton and heavy ion beams at the CERN SPS. CERN-SPSC-2000-010.

[21] B. L. Combridge et al. ASSOCIATED PRODUCTION OF HEAVY FLAVOUR STATES IN pp AND $\bar{p}p$ INTERACTIONS: SOME QCD ESTIMATES. *Nuc. Phys.*, B151:429–456, 1979.

[22] J. C. Collins et al. HEAVY PARTICLE PRODUCTION IN HIGH-ENERGY HADRON COLLISIONS. *Nuc. Phys.*, B263:37–60, 1986.

[23] R. L. Thews. Nonlinear behavior of quarkonium formation and deconfinement signals. In H. Thomas Elze, Erasmo Ferreira, Takeshi Kodama, Jean Letessier, Johann Rafelski, and Robert L. Thews, editors, *an American Advanced Studies Institute on New States of Matter in Hadronic Interactions*, volume 631, Campos do Jordao, Brazil, 2002. American Institute of Physics.

[24] S. S. Adler. Centrality dependence of charm production from single electrons measurement in Au + Au collisions at $\sqrt{s_{NN}} = 200$ GeV. 2004.

[25] R. Rapp and E. V. Shuryak. *D*-meson production from recombination in hadronic collisions. *Phys. Rev.*, D67:074036, 2003.

[26] CheukYin Wong. *Introduction to High-Energy Heavy-Ion Collisions*. World Scientific Publishing Co. Pte. Ltd, 1994.

[27] M. Adamovich et al. Nuclear dependence of charm production by a 340-GeV pi-beam. *Phys. Lett.*, B284:453–456, 1992.

[28] G. A. Alves et al. Atomic mass dependence of D+- and D0, anti-D0 production in 250-GeV pi+- nucleon interactions. *Phys. Rev. Lett.*, 70:722–725, 1993.

[29] M. J. Leitch et al. Nuclear dependence of neutral D meson production by 800-GeV/c protons. *Phys. Rev. Lett.*, 72:2542–2545, 1994.

[30] Y. Akiba. Charm measurements at SPS and RHIC. *J. Phys.*, G30:S283–S293, 2004.

[31] J. W. Cronin et al. Production of hadrons with large transverse momentum at 200-gev, 300-gev, and 400-gev. *Phys. Rev.*, D11:3105, 1975.

[32] L. Kluberg et al. Atomic number dependence of large transverse momentum hadron production by protons. *Phys. Rev. Lett.*, 38:670–673, 1977.

[33] B. Z. Kopeliovich, J. Nemchik, A. Schafer, and A. V. Tarasov. Cronin effect in hadron production off nuclei. *Phys. Rev. Lett.*, 88:232303, 2002.

[34] Alberto Accardi. Cronin effect in proton nucleus collisions: A survey of theoretical models. 2002.

[35] R. Vogt. The A dependence of open charm and bottom production. *Int. J. Mod. Phys.*, E12:211–270, 2003.

[36] Jens Ole Schmitt et al. Charm and Bottom Production at LHC and RHIC. *Phys.Lett.*, B498:163–168, 2001.

[37] Miklos Gyulassy. What Have we learned at RHIC? *J. Phys.*, G30:S911–S918, 2004.

[38] Edmond Iancu, Andrei Leonidov, and Larry McLerran. The colour glass condensate: An introduction. 2002.

[39] Y. Shutz. High energy heavy-ion collisions pot pourri.

[40] Berndt Muller and Xin-Nian Wang. Probing parton thermalization time with charm production. *Phys. Rev. Lett.*, 68:2437–2439, 1992.

[41] Klaus Geiger and Berndt Muller. Parton cascades in highly relativistic nuclear collisions. *Nucl. Phys.*, A544:467c–470c, 1992.

[42] Zi-wei Lin and M. Gyulassy. Open charm as a probe of preequilibrium dynamics in nuclear collisions? *Nucl. Phys.*, A590:495c–498c, 1995.

[43] Zi-wei Lin and Miklos Gyulassy. Open charm as a probe of preequilibrium dynamics in nuclear collisions. *Phys. Rev.*, C51:2177–2187, 1995.

[44] Peter Lévai, Berndt Muller, and Xin-Nian Wang. Open charm production in an equilibrating parton plasma. *Phys. Rev.*, C51:3326–3335, 1995.

[45] H. Satz and K. Sridhar. Charmonium production versus open charm in nuclear collisions. *Phys. Rev.*, D50:3557–3559, 1994.

[46] G. Agakishiev et al. Enhanced production of low mass electron pairs in 200-GeV/u S - Au collisions at the CERN SPS. *Phys. Rev. Lett.*, 75:1272–1275, 1995.

[47] P. Braun-Munzinger, D. Miskowiec, A. Drees, and C. Lourenco. Open charm contribution to the dilepton spectra produced in nuclear collisions at SPS energies. *Eur. Phys. J.*, C1:123–130, 1998.

[48] Torbjorn Sjostrand, Leif Lonnblad, Stephen Mrenna, and Peter Skands. Pythia 6.3 physics and manual. 2003. Please see cited works for specific version and parameters.

[49] Guo-Qiang Li, C. M. Ko, G. E. Brown, and H. Sorge. Dilepton production in proton nucleus and nucleus nucleus collisions at SPS energies. *Nucl. Phys.*, A611:539–567, 1996.

[50] Ralf Rapp and Jochen Wambach. Low mass dileptons at the CERN-SPS: Evidence for chiral restoration? *Eur. Phys. J.*, A6:415–420, 1999.

[51] M. C. Abreu et al. Dimuon and charm production in nucleus nucleus collisions at the CERN-SPS. *Eur. Phys. J.*, C14:443–455, 2000.

[52] A. P. Kostyuk, M. I. Gorenstein, and W. Greiner. Heavy flavor enhancement as a signal of color deconfinement. *Phys. Lett.*, B519:207–211, 2001.

[53] Ralf Rapp and Edward V. Shuryak. Thermal dilepton radiation at intermediate masses at the CERN-SPS. *Phys. Lett.*, B473:13–19, 2000.

[54] Cheuk-Yin Wong. Signatures of absorption mechanisms for J/ψ and *psi′* production in high-energy heavy-ion collisions. *Nucl. Phys.*, A630:487–498, 1998.

[55] Cheuk-Yin Wong. Private communication. 2004.

[56] V. Greco, C. M. Ko, and R. Rapp. Quark coalescence for charmed mesons in ultrarelativistic heavy-ion collisions. *Phys. Lett.*, B595:202–208, 2004.

[57] The long road from ISABELLE to RHIC. http://www.bnl.gov/bnlweb/history/RHIC_history.asp.

[58] M. Liu et al. Performance of the PHENIX Muon Tracking System in Run-2. Presentation to the APS Division of Nuclear Physics, April 20-23 2002, Albuquerque NM.

[59] S. H. Aronson et al. PHENIX Magnet System. *NIM A*, 499:480–488, 2003.

[60] H. Akikawa et al. PHENIX muon arms. *Nucl. Instrum. Meth.*, A499:537–548, 2003.

[61] C. Adler et al. The RHIC zero degree calorimeters. *NIM A*, 470:488–499, 2001.

[62] M. P. Bai et al. RHIC beam instrumentation. *NIM A*, 499:372–387, 2003.

[63] M. Allen et al. PHENIX inner detectors. *NIM A*, 499:549–559, 2003.

[64] S. S. Adler et al. J/ψ production in au-au collisions at $\sqrt{s_{NN}}$ = 200 gev at the relativistic heavy ion collider. *Phys. Rev.*, C69:014901, 2004.

[65] J. Drachenberg et al. Improvements to the PHENIX Muon Tracking Efficiency. Presentation to the Division of Nuclear Physics 2003 Fall Meeting October 29 - November 1, 2003, Tucson, AZ.

[66] R. Brun et al. GEANT 3.21 Detector Description and Simulation Tool, 1994. CERN Program Library Long Write-up W5013.

[67] M. Liu et al. Inclusive particle (muon) production in forward and backward rapidity in d-Au collisions at RHIC. Presentation to the Division of Nuclear Physics 2003 Fall Meeting October 29 - November 1, 2003, Tucson, AZ.

[68] H. D. Sato. *J/ψ Production in p+p Collisions at $\sqrt{s}$ = 200 GeV*. Dissertation, Kyoto University, 2002.

[69] Djamel Ouerdane. *Charged Pion and Kaon Production in Central Au+Au Collisions at $\sqrt{s_{NN}}$ = 200 GeV*. Dissertation, University of Copenhagen, 2003.

[70] A. Fasso, A. Ferrari, P. R. Sala, and J. Ranft. Fluka: Status and prospects for hadronic applications. Prepared for International Conference on Advanced Monte Carlo for Radiation Physics, Particle Transport Simulation and Applications (MC 2000), Lisbon, Portugal, 23-26 Oct 2000.

[71] E. W. Cornell et al. Calorimeter / absorber optimization for a RHIC dimuon experiment. *Nucl. Instrum. Meth.*, A350:150–173, 1994.

[72] M. L. Brooks et al. Heavy Flavor Production in pp Collisions at $\sqrt{s}$ = 200 GeV Measured by the PHENIX Muon Arms. 2004.

[73] T. Hachiya and Y. Akiba. Single eletron analysis in Run2 Au+Au. 2004.

[74] S. Eidelman et al. Review of particle physics. *Phys. Lett.*, B592:1, 2004.

[75] R. Vogt. Systematics of heavy quark production at RHIC. 2002.

[76] E. L. Bratkovskaya, W. Cassing, and H. Stocker. Open charm and charmonium production at RHIC. *Phys. Rev.*, C67:054905, 2003.

[77] F. O. Duraes, F. S. Navarra, and M. Nielsen. On open charm production in heavy ion collisions. *Braz. J. Phys.*, 34:290–292, 2004.

[78] Dmitri Kharzeev and Kirill Tuchin. Open Charm Production in Heavy Ion Collisions and the Color Glass Condensate. hep-ph/0310358, 2003.

[79] K. Adcox et al. Measurement of single electrons and implications for charm production in Au+Au collisions at $\sqrt{s_{NN}}$ = 130 GeV. *Phys. Rev. Lett.*, 88:192303, 2002.

[80] T. Hachiya et al. Single electron measurement at RHIC-PHENIX. Presentation to the Spring Meeting of the Japanese Physical Society, Kyusyu University, Fukuoka, Japan, March 27 - 30, 2004.

[81] J. Adams. Open charm yields in d+Au collisions at $\sqrt{s_{NN}}$ = 200 GeV. 2004.

[82] Sean Kelly et al. The PHENIX measurement of heavy flavour via single electrons in pp, dAu and AuAu collisions at $\sqrt{s_{NN}}$ = 200 GeV. *J. Phys.*, G30:S1189–S1192, 2004.

[83] S. S. Adler et al. J/ψ production from proton-proton collisions at $\sqrt{s} = 200$ GeV. *Phys. Rev. Lett.*, 92:051802, 2004.

[84] DongJo Kim et al. J/ψ production at RHIC/PHENIX. Presentation to the Hot Quark 2004 Workshop, The Inn at Snakedance in the Taos Ski Valley Resort, Taos, New Mexico, July 18-24, 2004.

Appendix

Decay Vertex Dependence

Appendix A

Vertex dependence of decay muons

A.1 1. Case: Free decay with no absorper

Let us start with the following assumptions:

- Only charged pions are considered, generically labeled π

- The pions are created with a uniform probability distribution $P_V\,(z_v)$ in the vertex position z_v between $-Z_V$ and $+Z_V$

- The pions are moving in the positive z-direction with the speed of light ($\beta = 1$) and Lorentz factor γ

- The pions will decay to muons with a half life of τ. The decay length λ_d of the pions is $\lambda_d = \gamma c \tau$.

- Assume $\lambda_d \gg Z_V$.

- The decay muons will have the same β and γ as the mother pion.

- A perfect muon detector is positioned at Z_D.

Typical numerical values for these quantities are:

$$Z_V = 0.40 \text{ m}$$

$$Z_D = 6.2 \text{ m}$$

$$\gamma = 1.3/0.140 = 9.3 \approx 10$$

$$c\tau = 7.8 \text{ m}$$

$$\lambda_d = \gamma c\tau = 10 \times 7.8 \text{ m} = 80 \text{ m}$$

$$\lambda_I = 0.16 \text{ m}$$

$$L_{spec} = 6.00 \text{ m}$$

The probability $P_V(z_v)$ that a pion is created at the vertex position z_v is assumed to be uniform

$$P_V(z_v) = \tfrac{1}{2Z_V} \text{ for } -Z_V < z_v < Z_V$$

The probablility $p_\mu(z)$ that a muon is created at the position z if the decaying pions was created at z_v is

$$p_\mu(z) = \tfrac{1}{\lambda_d} \exp\left(-\tfrac{z-z_v}{\lambda_d}\right)$$

The probability $P_\mu(Z_D, z_v)$ that a muon will have been generated from the decay of a pion, created at z_v, before entering the muon detector at $z = Z_D$ is

$$
\begin{aligned}
P_\mu(Z_D, z_v) &= \tfrac{1}{2Z_V} \int_{z_v}^{Z_D} \tfrac{1}{\lambda_d} \exp\left(-\tfrac{z-z_v}{\lambda_d}\right) dz \\
&= \tfrac{1}{2Z_V}\left(1 - e^{\frac{z_v - Z_D}{\lambda_d}}\right) \\
&= \tfrac{1}{2Z_V}\left(-e^{-\frac{Z_D}{\lambda_d}} + 1\right) - \tfrac{1}{2}\tfrac{z_v}{Z_V \lambda_d} e^{-\frac{Z_D}{\lambda_d}} - \tfrac{1}{4}\tfrac{z_v^2}{Z_D \lambda_d^2} e^{-\frac{Z_D}{\lambda_d}} + O\left(z_v^3\right) \\
&= \tfrac{1}{2Z_V}\left(1 - \exp\left(-\tfrac{Z_D}{\lambda_d}\right)\right) - \tfrac{1}{2Z_V}\tfrac{1}{\lambda_d}\exp\left(-\tfrac{Z_D}{\lambda_d}\right)z_v + O\left(z_v^2\right)
\end{aligned}
$$

This apparent linear relation in z_v will intersect the z-axis at Z_0

$$(1 - \exp\left(-\tfrac{Z_D}{\lambda_d}\right)) - \tfrac{1}{\lambda_d}\exp\left(-\tfrac{Z_D}{\lambda_d}\right)Z_0 = 0$$

$$Z_0 = -\frac{\lambda_d}{e^{-\frac{Z_D}{\lambda_d}}}\left(e^{-\frac{Z_D}{\lambda_d}} - 1\right) = \lambda_d\left(e^{\frac{Z_D}{\lambda_d}} - 1\right) = Z_D + \tfrac{1}{2}\frac{Z_D^2}{\lambda_d} + O\left(Z_D^3\right)$$

In the limit $Z_D \ll \lambda_d$ we obtain

$$Z_0 = Z_D$$

A.2 Calculation of Z_0

If muon yield at $z_v = -Z_V$ is N_- and the yield at $z_v = Z_V$ is N_+ then the linear z_v dependence will be

$$N(z_v) = \frac{N_- + N_+}{2} + \frac{N_+ - N_-}{2Z_V}z_v$$

and the intercept at the z-axis Z_0 is

$$Z_0 = Z_V\frac{N_- + N_+}{N_- - N_+}$$

The muon yield from $z_v = -Z_V$ and $z_v = -Z_V$ are

$$N_{\mu,vertex}(-Z_V) = 1 - e^{\frac{-Z_V - Z_V}{\lambda_d}} = 1 - e^{-2\frac{Z_V}{\lambda_d}} \approx 2\frac{Z_V}{\lambda_d}$$

$$N_{\mu,vertex}(Z_V) = 1 - e^{\frac{Z_V - Z_V}{\lambda_d}} = 1 - e^0 = 0$$

so

$$Z_0 = Z_V\frac{2\frac{Z_V}{\lambda_d} + 0}{2\frac{Z_V}{\lambda_d} - 0} = Z_V$$

which is the expected result.

A.3 Case 2: add decays within the absorber

Let us now add an absorber starting at Z_V with thickness L_{abs}. Assume the perfect muon detector is placed at $Z_D = Z_V + L_{abs}$. The muon production inside the absorber wil be

$$dN_\mu = N_\pi \frac{dz}{\lambda_d} = \frac{1}{\lambda_d} e^{-\frac{z}{\lambda_I}} dz$$

$$N_{\mu,absorber}(L_{abs}) = \frac{1}{\lambda_d} \int_0^{L_{abs}} e^{-\frac{z}{\lambda_I}} dz = \frac{1}{\lambda_d} e^{-\frac{L_{abs}}{\lambda_I}} \left(\lambda_I e^{\frac{L_{abs}}{\lambda_I}} - \lambda_I \right)$$

$$= \frac{\lambda_I}{\lambda_d} (1 - e^{-\frac{L_{abs}}{\lambda_I}}) \approx \frac{\lambda_I}{\lambda_d} \text{ for } L_{abs} \gg \lambda_I$$

so

$$N_+ = \frac{\lambda_I}{\lambda_d}$$

$$N_- = \frac{\lambda_I}{\lambda_d} + 2 \frac{Z_V}{\lambda_d}$$

and therefore

$$Z_0 = Z_V \frac{\frac{\lambda_I}{\lambda_d} + 2 \frac{Z_V}{\lambda_d} + \frac{\lambda_I}{\lambda_d}}{\frac{\lambda_I}{\lambda_d} + 2 \frac{Z_V}{\lambda_d} - \frac{\lambda_I}{\lambda_d}} = Z_V + \lambda_I$$

A.4 Case 3: Add free decay space behind absorber

Assume that a free space of length L_{spec} is located after the absorber and before the detector. The probability of a muon produced in this space will be the product of the probability that a pion makes it through the absorber and the probability that it decays in the free space. Assume the perfect muon detector is placed at $Z_D = Z_V + L_{abs} + L_{spec}$. If we neglect the small reduction in pion flux due to decay inside the absorber, the probabilty that a pion goes through the absorber is

$$N_{\pi,abs} = e^{-\frac{L_{abs}}{\lambda_I}}$$

The decay probability in the free space is

$$P_{\mu,spec} = 1 - e^{\frac{-L_{spec}}{\lambda_d}}$$

The muon production in the free spectrometer space is therefore

$$N_{\mu,spec} = e^{-\frac{L_{abs}}{\lambda_I}} \left(1 - e^{\frac{-L_{spec}}{\lambda_d}}\right) \approx \frac{L_{spec}}{\lambda_d} e^{-\frac{L_{abs}}{\lambda_I}}$$

so

$$N_+ = \frac{\lambda_I}{\lambda_d} + \frac{L_{spec}}{\lambda_d} e^{-\frac{L_{abs}}{\lambda_I}}$$

$$N_- = \frac{\lambda_I}{\lambda_d} + 2\frac{Z_V}{\lambda_d} + \frac{L_{spec}}{\lambda_d} e^{-\frac{L_{abs}}{\lambda_I}}$$

and therefore

$$Z_0 = Z_V \frac{\frac{\lambda_I}{\lambda_d} + 2\frac{Z_V}{\lambda_d} + \frac{L_{spec}}{\lambda_d} e^{-\frac{L_{abs}}{\lambda_I}} + \frac{\lambda_I}{\lambda_d} + \frac{L_{spec}}{\lambda_d} e^{-\frac{L_{abs}}{\lambda_I}}}{\frac{\lambda_I}{\lambda_d} + 2\frac{Z_V}{\lambda_d} + \frac{L_{spec}}{\lambda_d} e^{-\frac{L_{abs}}{\lambda_I}} - \frac{\lambda_I}{\lambda_d} - \frac{L_{spec}}{\lambda_d} e^{-\frac{L_{abs}}{\lambda_I}}}$$

$$\boxed{Z_0 = Z_V + \lambda_I + L_{spec} e^{-\frac{L_{abs}}{\lambda_I}}}$$

Numerical example:

$$Z_0 = 0.40 + 0.16 + 6.0 e^{-\frac{1.20}{0.16}} = 0.563 \text{ m}$$

Vita

Andrew Miles Glenn was born on September 26, 1975 in the small Appalachian town of Boone, North Carolina. He graduated from Watauga High School in Boone in May 1993. Two months later, he moved to Berea, Kentucky to pursue his bacheloriate studies at Berea College. During his time there he worked as a teaching assistant in the math and later the physics departments. He began to take a serious interest in scientific research while working with Berea College professor Michael Chrescimano during a summer project at the Boston University Center for Space Physics. The research focused on development of an image reconstruction algorithm for the Single Element Imaging Spectrograph for the TERRIERS satellite. In 1997 he graduated from Berea with a Bachelor of Arts in Physics.

After two summers of research participation in the University of Tennessee's Science Alliance program, he began graduate studies there in August of 1997. For the first two years he served as a teaching assistant, during which he was awarded the Robert W. Lide citation for development of undergraduate laboratories. He then began his doctoral research in experimental high-energy nuclear physics. Under the tutelage of his advisor Dr. Soren Sorensen he started research with the PHENIX experiment located at Brookhaven National Laboratory's Relativistic Heavy Ion Collider (RHIC). During his time at BNL he provided extensive aid in the instrumenting, commissioning, and support of the PHENIX muon identifiers. He assisted in muon aspects of the analysis of Au+Au and $p + p$ collision data.